A SURVEY OF EGRET SOURCES USING THE MILAGRO OBSERVATORY

By

Chuan Chen

A DISSERTATION

Submitted to
University of California, Irvine
in partial fulfillment of the requirements
for the degree of

DOCTOR OF PHILOSOPHY

Department of Physics and Astronomy

2008

ABSTRACT

A SURVEY OF EGRET SOURCES USING THE MILAGRO OBSERVATORY

By

Chuan Chen

Very high energy gamma-rays can be used to understand some of the most powerful astrophysical objects in the universe, such as active galactic nuclei, supernova remnants and pulsar wind nebula. EGRET is one of the four instruments of the Compton Gamma Ray Observatory (CGRO) project which detected gamma-ray emission from 30 keV to 30 GeV. EGRET covered an energy range between 20 MeV and 30 GeV. The third EGRET catalog contained 271 new gamma-ray sources with energies above 100 MeV. The 271 sources in this catalog include the single 1991 solar flare, the Large Magellanic Cloud, five pulsars, one radio galaxy, and 66 high-confidence identification of blazars. In addition, 27 lower confidence potential blazar identifications are noted. The rest of sources, 170 out of 271, have not yet been identified with known objects.

Located in northern New Mexico, the Milagro gamma-ray observatory employs a water-Cherenkov technique to continuously monitor the northern sky for TeV gamma-ray emission from astrophysical sources. The instrument has a large field of view, which covers the entire overhead sky (~ 2 sr) and has a high duty cycle ($> 90\%$). More than seven years of Milagro data are used to search for TeV gamma-ray emission from the EGRET sources in the northern sky. Milagro's new gamma-hadron separation variable, A_4, coupled with the weighting analysis technique significantly improves the sensitivity of the Milagro detector. In my thesis I present the flux and flux upper limits of 129 EGRET sources which are in the Milagro field of view using two different gamma-hadron separation parameters, $X2$ and A4. The median energies

for $X2$ and A_4 are 7 TeV and 25 TeV respectively. Constrains on the flux of these sources at 7 TeV and 25 TeV are computed assuming a differential photon spectrum of a power law with spectral index $\alpha = -2.3$. For 18 EGRET unidentified sources I compare the Milagro flux (if $\sigma > 2.0$) and flux upper limits (if $\sigma < 2.0$) with the flux measured by EGRET at 100 MeV and the flux upper limits measured by the Whipple observatory at 350 GeV. The comparison of Milagro measurements, EGRET and Whipple extrapolation to Milagro energies using the spectral indices taken from 3EG catalog are presented. Because the typical point spread function of EGRET is large ($\sim 5^\circ$), Monte Carlo simulations are used to find out an optimum analysis technique to search EGRET sources in Milagro data.

ACKNOWLEDGMENTS

Contents

List of Tables

List of Figures

Chapter 1

Introduction to Very High Energy Gamma-Ray Astronomy

Very high energy (VHE) gamma-ray astronomy is defined as observations of celestial γ-rays at energies above 100 GeV up to 100 TeV. This field resulted from the extension of observation in γ-ray astronomy, performed by satellites, upwards in energy, and the study of cosmic-rays, where the detection of cosmic photons above $\sim$1 TeV with ground based instruments was pursued. As VHE observations are at the high end of the observable electromagnetic spectrum there has been much difficult in identifying sources of VHE γ-rays. However, the development of the imaging air cherenkov telescopes allowed for the detection of the first TeV γ-ray source, the Crab Nebula, about 19 years ago [1].

High energy γ-ray astronomy was outgrowth from two distinct fields of study. In the early 1970s, space-based detectors extended the field of x-ray astronomy upwards in energy to high energy γ-rays and observed a number of discrete source of 100 MeV photons. The study of cosmic photons above $\sim$ 1 TeV was pursued by physicists with ground-based instruments, which were an outgrowth of cosmic-ray studies. Although the techniques of space-based and ground-based γ-ray astronomy are distinct, the science addressed by them overlaps considerably. And detectors are being developed to bring the energies studied on earth and in space closer together. This chapter explains the motivations of study VHE γ-ray astronomy and describes various methods that are useful for detecting VHE γ-ray sources.

1.1 Motivation for VHE Gamma-Ray Astronomy

The study of VHE γ-ray astronomy can provide insights into a number of scientific areas. The first major science area addressed by high-energy γ-ray astronomy is the nature of cosmic-particle acceleration mechanisms. The photon spectra observed at VHE energies are non-thermal and most likely originate from interaction of particles accelerated to high energy with ambient matter or photons in energetic astrophysical sources, such as Supernova Remnant (SNR), Pulsar Wind Nebula (PWN), etc. The second area is the cosmic ray origins. Because of the galactic magnetic field, even the protons with energies up to 10^{18} eV coming from galactic source $\sim$ 10 kpc away have lost all directional information before reaching the Earth. Since γ-rays do not bend in the galactic magnetic fields, they can point back to the sources of the cosmic rays. The study of exotic objects is another motivation for VHE γ-ray astronomy. All of the sources detected at TeV energies contain compact objects such as black holes and neutron stars. In addition, there are many speculative objects, such as cosmic strings and primordial black holes, that may produce TeV photons. VHE γ-ray astronomy can provide further insight into the known and speculative phenomena. The study of photon propagation through the intergalactic medium is also addressed by VHE γ-ray astronomy. Observations of TeV sources can provide a measurement of the spectrum of the infrared component of the extragalactic diffuse photon background (EBL) which is currently poorly known. It may also provide new information related to the epoch of star and galaxy formation as well as various dark matter hypotheses. Finally, the

VHE γ-ray astronomy can study the nature of nuclear and particle interactions at energies above those available at terrestrial accelerators.

1.2 Gamma-Ray Detection

There are two techniques of detections in the VHE γ-ray astronomy[2].

First note that Earth's atmosphere is opaque to high-energy photons. At sea level, the atmosphere is ~ 28 radiation length thick. This implies the probability that a photon will survive to ground level is negligible small. Thus only a detector above the Earth's atmosphere, in a balloon or a satellite, can detect primary cosmic γ-rays. Second, the fluxes of high-energy γ-rays from astrophysical sources are low and decrease rapidly with increasing energy. The collecting power of a satellite becomes inadequate at high photon energies. Thus VHE and UHE astronomers use Earth-based detectors. Third, the flux of high-energy charged cosmic rays is much larger than the γ-ray flux. The all-particle cosmic-ray flux is many orders of magnitude greater than photon flux in the region from 100 GeV to ~ 100 TeV. Rejection of the large cosmic-ray background is extremely important in high-energy γ-ray astronomy.

1.2.1 Space-based Detectors

Space-based high energy γ-ray detectors are flown on satellites or high altitude balloons. They can detect γ-rays directly when they pass through the detector and interact with the detector material. One technique uses the resulting electron-positron pairs to determine energy and direction of the incoming photon. The satellite detectors typically include three basic components: a tracking chamber, a calorimeter, and an anti-coincidence shield. The tracking chamber is used to record the path of charged particles within the detector. The tracks are used to reconstruct the direction of the initial γ-ray photon through the identification of the electron positron pair

Photon energy	Energy resolution (FWHM)	Angular resolution (FWHM)	Effective area
100 MeV	26%	5.5°	930 cm^2
500 MeV	20%	2.0°	1570 cm^2
1 GeV	19%	1.2°	1300 cm^2
10 GeV	26%	0.4°	690 cm^2

Table 1.1: EGRET characteristics [2]

that resulted from the annihilation of this γ-ray photon. Calorimeter determines the energy of the incident photon by measuring the integrated path length of particles in the electromagnetic cascade produced by the incident photon. The anti-coincidence shielding typically consists of scintillators that are used to veto events caused by charged particles incident on the detector.

Space-based detectors can unambiguously identify γ-rays with an angular resolution of about 1°, an energy resolution better than 15%, and have a field of view of 20°-40° half-angle. Unfortunately, the detectors can only detect γ-rays below the VHE energy regime. This is because a typical source's flux decreases dramatically as energy increases, requiring a very large detection area for VHE observations. Nonetheless, the sources identified by these satellites are useful indicators of what objects may be bright in the VHE sky.

The most sensitive high-energy γ-ray space-based detector to date was the EGRET instrument aboard the Compton Gamma Ray Observatory (CGRO) [5]. It operated from 1991 to 2000. CGRO had four instruments that covered an unprecedented six decades of the electromagnetic spectrum, from 30 keV to 30 GeV. In order of increasing spectral energy coverage, instruments were the Burst And Transient Source Experiment (BATSE), the Oriented Scintillation Spectrometer Experiment (OSSE), the Imaging Compton Telescope (COMPTEL), and the Energetic Gamma Ray Experiment Telescope (EGRET). The performance of EGRET is listed in table 1.1.

EGRET was able to detect a total 271 sources above energy of 100 MeV. Of these

66 have been identified with high confidence and 27 with low confidence as blazars, 5 pulsars, 1 probable radio galaxy detection, the Large Magellanic Cloud, and one very bright solar flare which occurred in 1991 (see figure 1.1). In addition to this galactic diffuse emission, as well as extragalactic diffuse emission were identified [40]. The unidentified sources are those which do not have an identified counterpart at other wavelengths, and in some circumstances may be a collection of high energy sources. Currently the nature of these unidentified sources is an active area of research, as is a full understanding of the nature and cause of the extragalactic γ-ray background [6]. Recently some of these sources have been tentatively associated with VHE sources detected in the HESS Galactic plane survey [7], as well as some of the new Milagro sources.

Scheduled for launch in mid-2008, the Gamma Ray Large Area Space Telescope (GLAST) is a next generation high-energy γ-ray observatory designed for making observations of celestial γ-ray sources in the energy band extending from 100 MeV to more than 100 GeV. It follows in the footsteps of the EGRET experiment. The key scientific objectives of the GLAST mission are:

- To understand the mechanisms of particle acceleration in AGNs, pulsars, and SNRs.
- Search the γ-ray sky for unidentified sources and diffuse emission.
- Determine the high-energy behavior of γ-ray bursts and transients.
- Probe dark matter and early Universe.

The GLAST has a field of view of more than 2.5 steradians, and sensitivity about 50 times that of EGRET at 100 MeV and even more at higher energies. Its two year flux limit for source detection in an all-sky survey is 1.6×10^{-9} photons $cm^{-2}s^{-1}$ (at energies $>$ 100 MeV). It will be able to locate sources to positional accuracies of 30 arc seconds to 5 arc minutes.

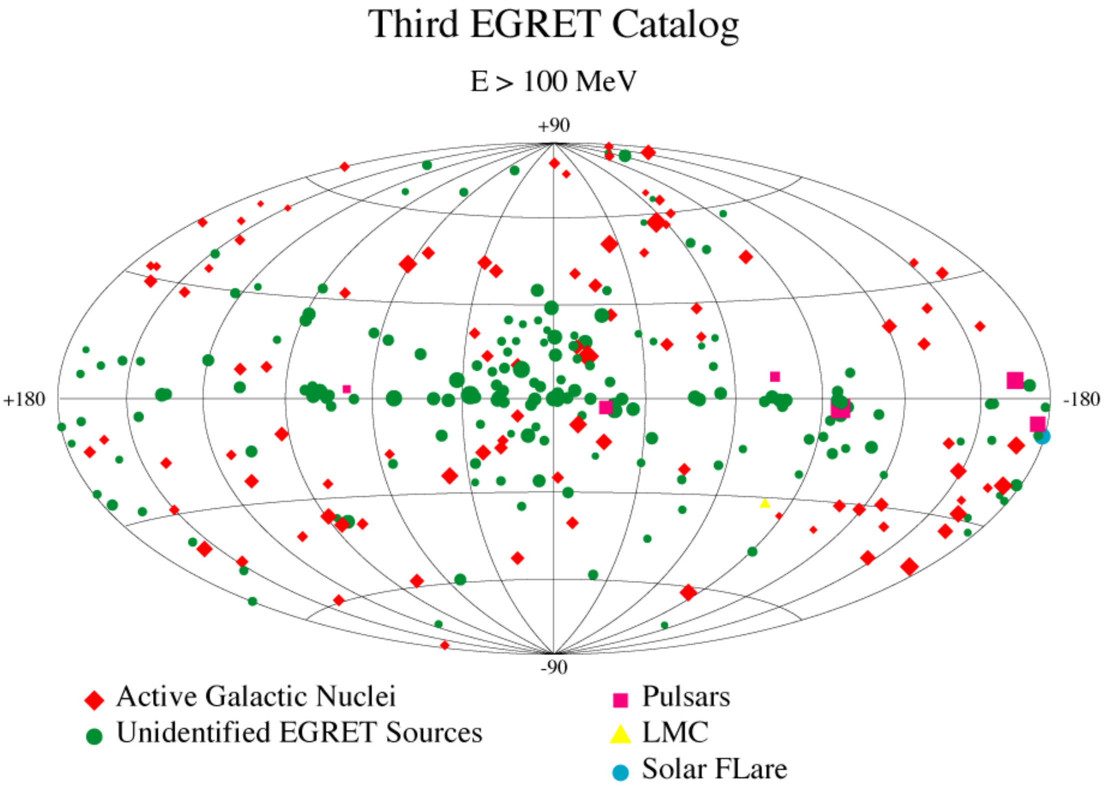

Figure 1.1: Third EGRET source catalog, shown in Galactic coordinates. The size of each symbol is proportional to the highest intensity seen for the corresponding source. Taken from [8].

1.2.2 Grand-based Detectors

Although the space-based γ-ray detectors have a great advantage in γ-hadron separation though direct particle identification, the effective areas of such detectors are limited by their physical size and ultimately by the payload limits of available launch vehicles necessary for the insertion of a detector into orbit. For the study of γ-ray sources at energies above 1 TeV, ground based methods which are free from this limitation are required.

However, the atmosphere is opaque to VHE photons. Therefore the secondary effects of the interaction of the VHE photon with the atmosphere are used to determine the direction and energy of the initial photon. This is done by either detecting the secondary particles in the Extensive Air Shower (EAS) which results from the interaction of the VHE photons in the upper atmosphere or by detecting the Cherenkov light produced by these secondary particles as they propagate through the atmosphere. Astronomical observations are made possible because the EAS retains the original direction of the incident photon to a high degree. Further, the spread of secondary particles, as well as Cherenkov photons, is very large (several hundred meters in radius) allowing for a ground based detector to have a collection area that is large enough to make it sensitive to the flux of γ-rays from VHE sources. In other words, the atmosphere is an amplifier for collection area.

One main disadvantage for ground based γ-ray detectors is the large background from cosmic-rays. Cosmic-rays, consisting of protons and heavier nuclei, are constantly striking the atmosphere. These cosmic rays produce EAS that are superficially similar to those produced by photons, and are $\sim$ 10,000 more numerous for a given incident photon energy. This large hadronic background limits the sensitivity of ground based detectors and makes it very hard to observe a statistically significant signal from a celestial γ-ray source. To minimize the effect of this large hadronic background, differences in the EAS initiated by hadronic particles and photons have to be used for rejecting cosmic ray triggers.

1.2.3 Cosmic Rays and Extensive Air Showers

The Earth is immersed in a ”sea” of high-energy nuclei known as cosmic rays. In the late 1800’s people realized that there was an ionizing radiation present in the our surroundings. But it was not until Victor Hess performed a series of high-altitude balloon flights beginning in 1905, that we learned that the origin of this radiation was beyond the Earth’s atmosphere. Hess won the Nobel prize for this discovery in 1936. At present we know that cosmic rays are composed of all nuclei, from the simple hydrogen nucleus (a proton) to the iron nucleus and beyond (transuranic elements have been observed in cosmic rays). The energy spectrum of cosmic rays has been measured beyond 10^{20} eV (electron-volts) and is shown in figure 1.2. A well hit tennis ball has roughly the same energy as the highest energy cosmic rays, but here it is packed into a single atomic nucleus.

When a high-energy cosmic ray enters the atmosphere it loses its energy via interactions with the nuclei that make up the air. At high energies these interactions create particles. These new particles go on to create more particles, etc. This multiplication process is known as a nuclear-electromagnetic cascade. This process continues until the average energy per particle drops below about 80 MeV for the electro-magnetic component. At this point the interactions lead to the absorption of particles and the cascade begins to die. This altitude is known as shower maximum. The particle cascade looks like a pancake of relativistic particles traveling through the atmosphere at the speed of light. Though the number of particles in the pancake may be decreasing, the size of the pancake always grows as the interactions cause the particles to diffuse away from each other. When the pancake reaches the ground it is roughly 100 meters across and 1-2 meters thick. If the primary cosmic ray was a photon the pancake will contain mainly electrons, positrons, and gamma rays. If the primary cosmic ray

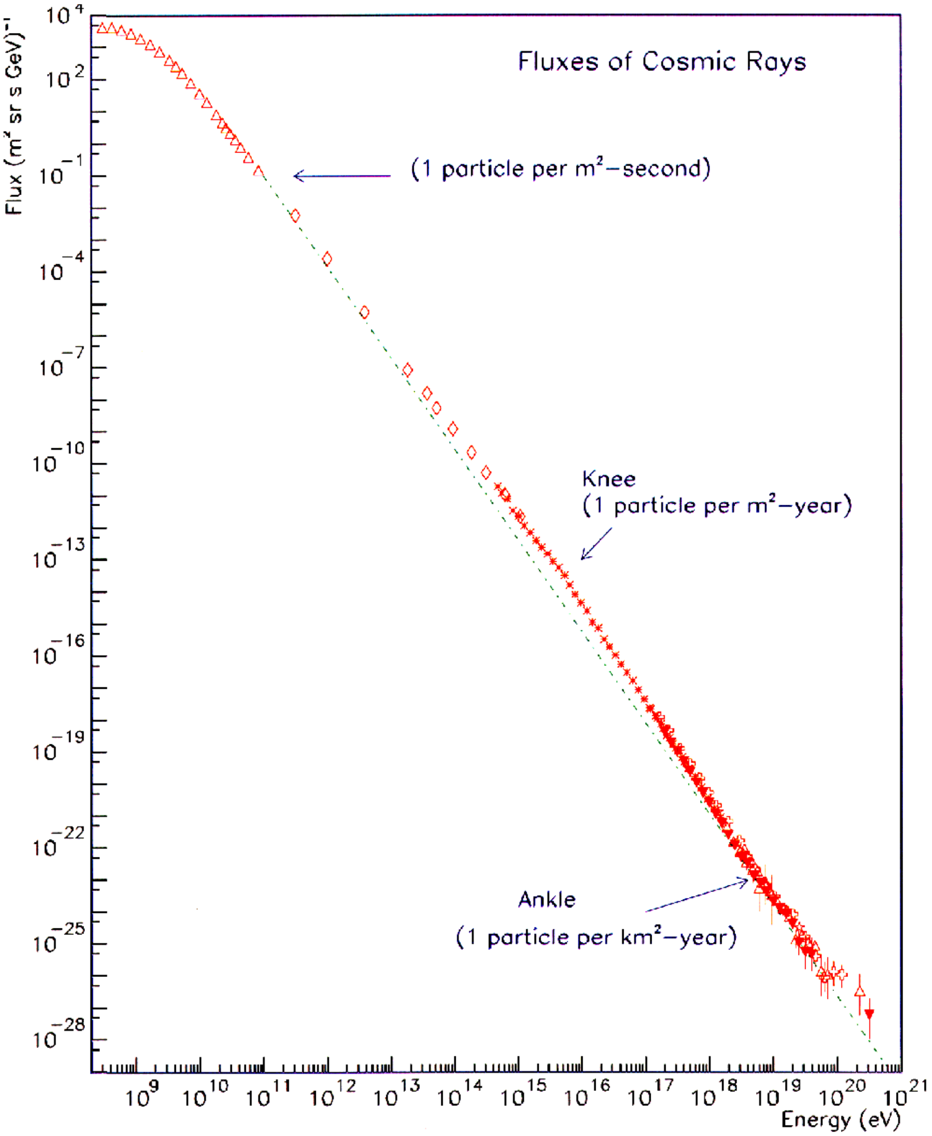

Figure 1.2: The energy spectrum of cosmic rays measured up to 10^{21} eV.

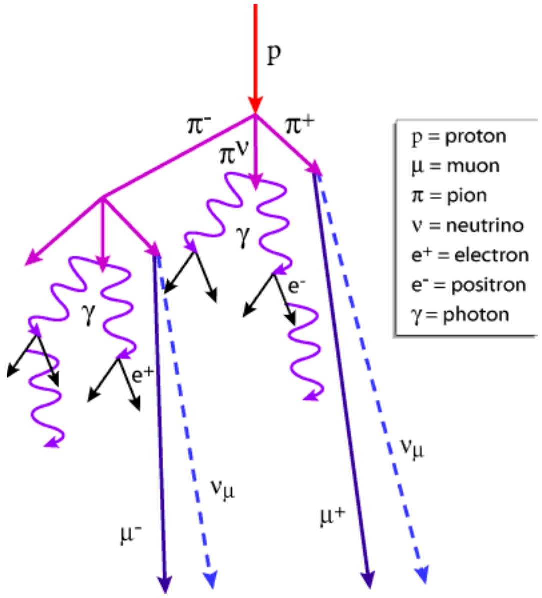

Figure 1.3: Schematic of an extensive air shower. The initial particle is a proton. Taken from [10]

was a nucleus the pancake will also contain muons, neutrinos, and hadrons (protons, neutrons, and pions). The number of particles left in the pancake depends upon the energy of the primary cosmic ray, the observation altitude, and fluctuations in the development of the shower. This particle pancake is known as an extensive air shower (or simply an air shower). A schematic of an EAS is shown in figure 1.3.

1.2.4 Imaging Atmospheric Cherenkov Detectors

The Imaging Atmospheric Cherenkov Technique (IACT) is the method whereby very high energy γ-ray photons in the 50 GeV to 50 TeV range can be detected by ground based telescopes, by imaging the Cherenkov photons produced by the shower.

Due to the rapidly falling flux of γ-ray photons from cosmic sources in this energy regime, space-based detectors become ineffective due to their small collection areas which are often limited to some tens or hundreds of square centimeters. In the case of the IACT, the Earth's atmosphere is used as the detection medium, implying a collection area of many hundreds of square meters. This enables IACT instruments to detect γ-ray photons in an energy regime inaccessible to space-based instruments.

The IACT works by imaging the very brief flash of Cherenkov radiation generated by the cascade of relativistic charged particles produced when a very high-energy γ-ray strikes the atmosphere. These extensive air showers are initiated at an altitude of 10-20 km. The incoming γ-ray photon undergoes pair production in the vicinity of the nucleus of an atmospheric molecule. The electron-positron pair produced are of extremely high energy and immediately undergo Bremsstrahlung or 'Braking Radiation'. This radiation produced is itself extremely energetic, with many of the photons undergoing further pair production. A cascade of charged particles ensues which, due to its extreme energy, produces a flash of Cherenkov radiation lasting between 5 and 20 ns. The total area on the ground illuminated by this flash corresponds to many hundreds of square meters, which is why the effective area of IACT telescopes is so large.

The instrument used to detect the brief flash of Cherenkov radiation comprises a large segmented mirror which reflects the Cherenkov light onto a camera consisting of an array of photomultiplier tubes. The tubes are coupled to fast electronics which amplify, digitise and record the pattern or image of the shower. The image shape provides discrimination of Cherenkov showers produced by primary γ-rays and primary cosmic rays, and combined with angular resolution provides rejection of $>$ 99% of cosmic ray triggers. The most effective mode of operation is to use an array of such telescopes, which can be typically located 70 to 120 meters apart. The primary advantage of this mode of operation is that the energy threshold (the peak sensitivity) of the telescope can be lowered as local muons produced by cosmic ray induced showers can be eliminated. This is because the narrow Cherenkov light cone produced by local muons will only be recorded by a single telescope. The shower reconstruction and background rejection offered by an array of telescopes provides an

Figure 1.4: The HESS telescope array in Namibia.

order of magnitude increase in sensitivity and improved angular and energy resolution as compared to a single telescope. This advantage has been used to great effect by the HESS telescope array (see figure 1.4)which has detected several new sources of very high energy γ-ray photons in recent years.

The IACT was pioneered by the Whipple collaboration and led to the discovery of TeV emission from the Crab Nebula in 1989. The Whipple 10m telescope (see figure 1.5) also discovered the first extra-galactic source of TeV emission with the detection of very high energy γ-ray emission from the active galaxy Markarian 421. The HEGRA telescope array was the first system to use multiple telescopes, a technique known as stereoscopy. The largest IACT telescope is the 17 m MAGIC telescope at the Roque de los Muchachos Observatory in La Palma. As of 2007, the HESS collaboration are currently planning construction of a 30 m dish in Namibia.

1.2.5 Extensive Air Shower Arrays (EASA)

IACTs have large collection areas ($> 50{,}000$ m^2) and a good angular resolution ($\sim 0.1^\circ$) and reasonably good energy resolution ($\sim 20\%$ - 40%). However, they are limited by their small field of view ($< 5^\circ$) and low duty cycle ($< 10\%$). This latter effect is the result of the requirement that observations be made on moonless, cloudless nights because the Cherenkov signals are faint and produced at altitudes of several kilometers.

Figure 1.5: The Whipple Observatory 10 m γ-ray telescope on Mount Hopkins in southern Arizona.

Another way for the ground based observation of TeV γ-rays is the use of a large array of particle detectors for the direct detection of the shower particles of an extensive air shower. Arrays have two advantages over IACTs: the large duty cycle ($> 90\%$), and the large field of view (~ 2 sr). These two factors provide the ability for continuously monitoring the over-head sky, study of transient sources, and performing sky surveys.

EAS arrays have typically consisted of numerous scintillator detectors spread out over a large area ($>$1 km^2). Several EAS arrays are described in [11] and [12]. The individual detectors that make up the array measure the arrival times of charged particles across the shower front. The times are then used to reconstruct the air shower direction. The individual scintillators measure the energy deposited by charged particles in the shower. This information determines the size of the air shower and can be related to the energy of the initiating particle. Some separation of γ-ray induced and proton induced air showers is achieved with this technique by finding the presence of muons, a hadronic by-product.

This approach (EASA) was first proposed as far back as 1958 [13] and was quickly followed by extremely optimistic flux predictions. The first experiment was CYGNUS array (April, 1986) [14] which was the first ground based array constructed explicitly for the purpose of searching for 100 TeV γ-ray sources. In its first phase CYGNUS consisted of 108, and was later expanded to 200, scintillation counters dispersed over a 20,000 m^2 area near Los Alamos, NM. In addition a number of buried muon detectors were utilized in order to distinguish hadronic EAS's from γ-ray EAS's. The major obstacle for an EAS arrays is the large background due to the presence of the cosmic rays. Though CYGNUS was unable to detect γ-ray point sources the quest to improve this technique proceeded. Another ground-based array is the Tibet AS-gamma Experiment which is located at an altitude of 4,300 m at Yangbajing in Tibet, China. Tibet AS-gamma array consists of 697 scintillation counters which are placed at a lattice with 7.5 m spacing and 36 scintillation counters which are placed at a lattice with 15 m spacing. Each counter has a plastic scintillator, 0.5 m^2 in area and 3 cm in thickness, equipped with a 2-inch-in-diameter PMT. The time and charge information of each PMT hit by an air shower event is recorded to determine its direction and energy. The detection threshold energy is approximately 3 TeV. The event trigger rate is currently 1.5 kHz and the data size is 26 GB/day. Figure 1.6 shows the Tibet air shower array.

1.2.6 Water Cherenkov Array

The difficulty in the searching for TeV γ-ray sources using the EAS array lies in its low sensitivity, high energy threshold and the lack of an effective γ-hadron separation technique. For the purpose of discriminating γ-rays and hadron induced EAS's, the water Cherenkov array, Milagro, was developed.

Figure 1.6: The Tibet air shower array. Taken from [15].

The Milagro γ-ray detector is located at Los Alamos, NM. It is a new type of detectors that uses the water Cherenkov technique to detect extensive air showers. The use of water as a detection medium has the advantage of lowering the energy threshold of the detector to energies comparable to those of IACT's. The lower energy threshold is achieved through the detection of nearly every relativistic particle in an extensive air shower. At ground level, γ-rays in an EAS outnumber electrons and positrons by a factor of ~ 5. In an air shower array these photons are usually undetected. Upon their entrance into the water, these γ-ray photons convert to electron-positron pair or Compton scatter electrons which will in turn produce Cherenkov radiation that can be detected. With an appropriate γ-hadron separation variable, Milagro detected the Crab Nebula at the 6.4 σ in 2003 [31]. Since then improvements in Milagro reconstruction algorithms and γ-hadron separation techniques have made possible the observation of numerous sources including Mrk 421 [38], the Cygnus region hot spot (MGRO J2019+37), diffuse emission from the Cygnus region [16] and the Galactic plane [17] demonstrating the potential of array based γ-ray astronomy for the survey and monitoring of the overhead sky.

Chapter 2

The Milagro Detector

The Milagro γ-ray Observatory is a ground-based TeV detector that uses the water Cherenkov detector to observe the extensive air showers produced by high energy particles impacting the Earth's atmosphere. The wide field of view ($\sim 2sr$) and high duty cycle ($> 90\%$) make Milagro an excellent survey instrument and provide observations of a broad range of γ-ray and cosmic-ray phenomena.

The details of the detector configuration, water system, electronics and DAQ system, calibration, event reconstruction and simulations are described in this chapter.

2.1 Milagro Detector Description

The Milagro observatory is located near Los Alamos, NM, in the Jemez mountains at latitude 35° 52' 45" and longitude 106° 40' 37" West. The altitude of the detector is 2630 m which is equal to an atmospheric overburden of 750 g cm^{-2}. The Milagro detector consists of a six million gallon artificial pond sealed with a light tight cover and instrumented with 723 photomultiplier tubes (PMTs) arranged in two layers. The pond has dimensions of 80 m × 60 m × 8 m (depth). The sides of the pond are sloping and the area of the bottom is 50 m × 30 m. In addition to the pond, Milagro is surrounded by a sparse outrigger array of 175 tanks with each containing

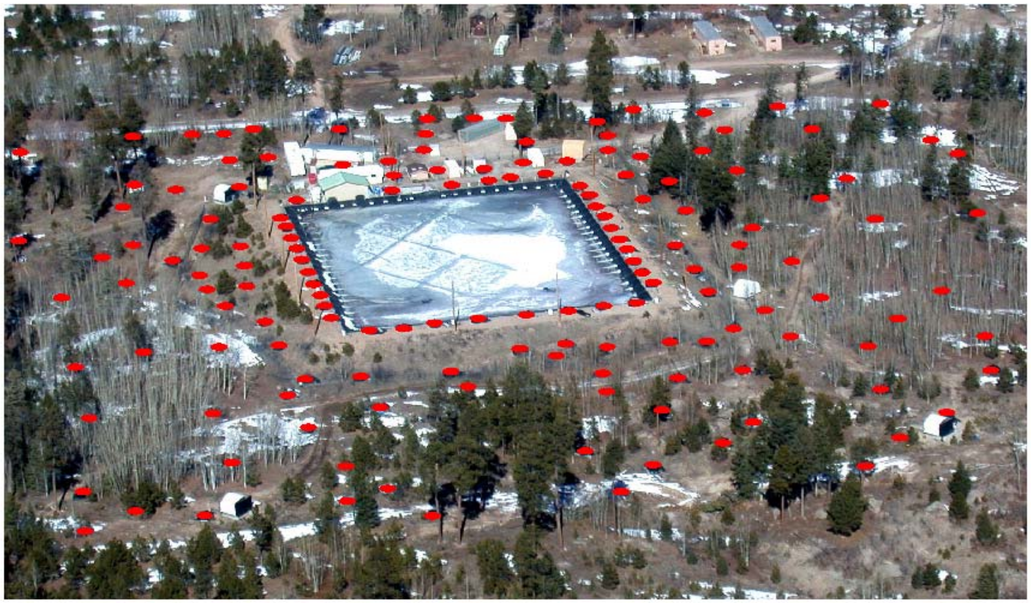

Figure 2.1: An aerial view of the Milagro detector. The red circles mark locations of the outrigger tanks.

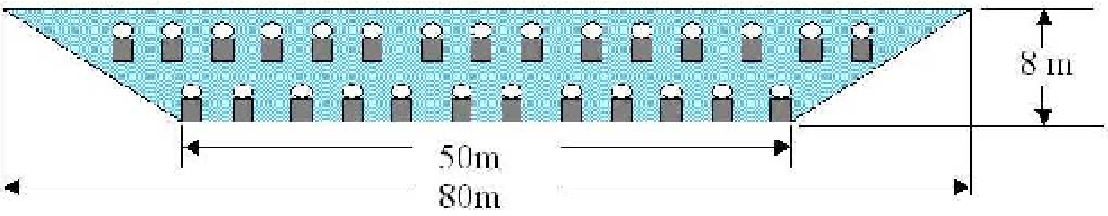

Figure 2.2: A schematic diagram of the Milagro pond.

an individual PMT. The pond and the outrigger array cover an area of 40,000 m^2. Figure 2.1 shows an aerial view of Milagro and figure 2.2 shows a schematic diagram of the pond.

2.1.1 The Pond

The pond PMTs are arranged in two layers. The top layer, referred to as the air shower (AS) layer, consists of 450 PMTs at 1.5 m below the pond water surface. This layer is used primarily for triggering and event reconstruction. The bottom layer,

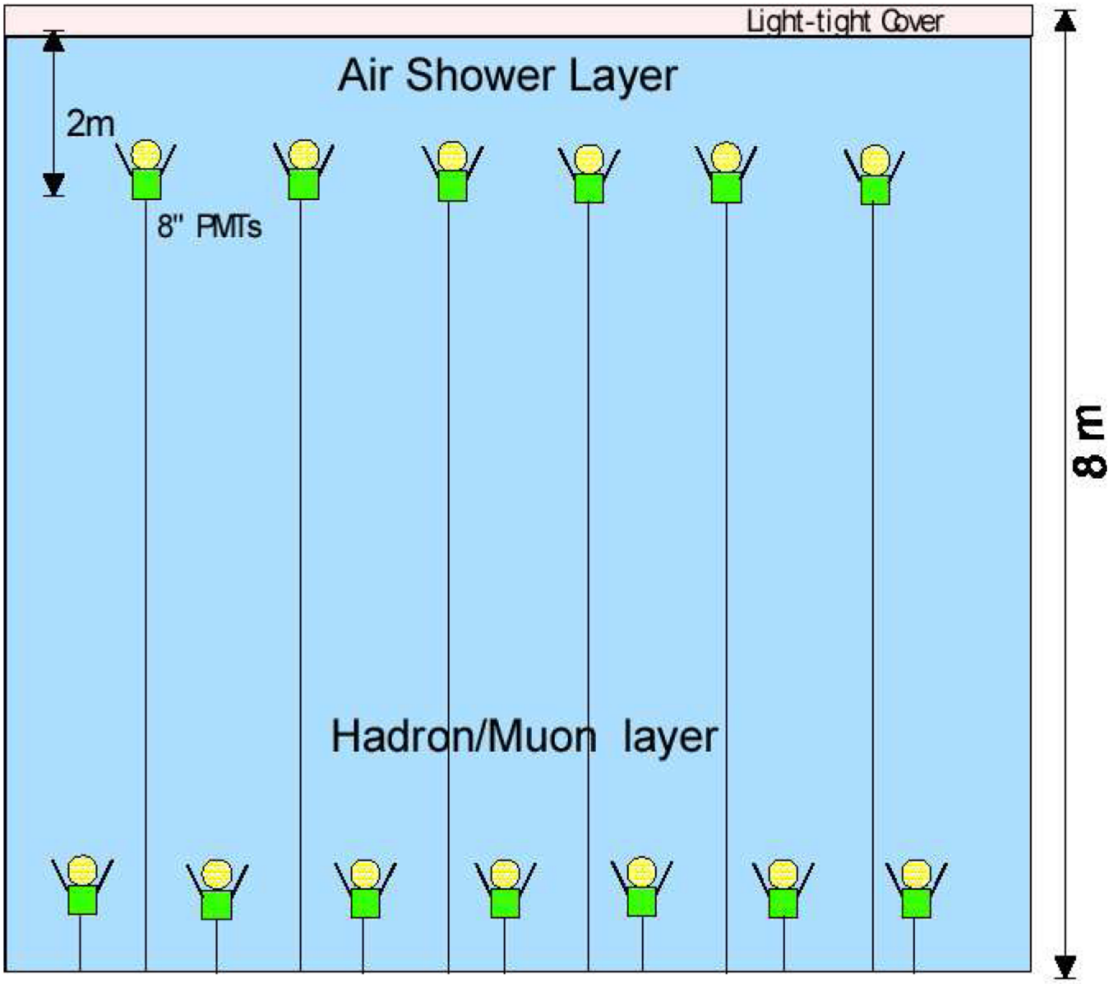

Figure 2.3: Schematic of PMT placement in the pond (not to scale). Figure taken from [3].

referred to as the muon layer (MU), consists of 273 PMTs at 6 m below the pond surface. It is used primarily for background rejection. In each of these layers the PMTs are arranged on a 2.8 $m \times 2.8$ m grid. The MU layer PMTs are horizontally offset from the AS layer PMTs by half the grid spacing. Figure 2.3 shows a schematic diagram of the PMT placement in the pond [3]. Figure 2.4 shows the inside of the pond. The AS layer PMTs can be seen attached to the grid crossing, while the MU layer PMTs are tied between grid crossing. This photo was taken with the cover inflated during one of the tube repair operations.

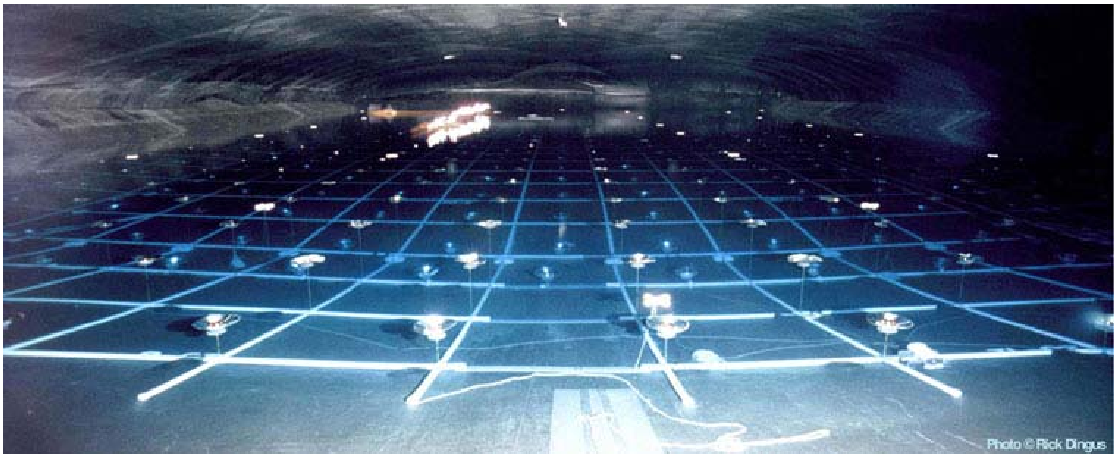

Figure 2.4: An inside view of the Milagro pond.

Due to the higher index of refraction of water the Cherenkov angle is $\sim 41°$. This leads to a substantial increase in the detectable Cherenkov light pool within the detector. The two layer design of the Milagro pond also provides a method of background rejection when searching for sources of γ-ray emission. Cosmic ray induced EAS's contain a large muon component and high energy hadrons and γ-rays which provides a means of discrimination and background rejection (see section 3.5). The distance from the water surface to the AS layer is approximately 4 radiation lengths for γ-rays. So the γ-rays convert to electrons and positrons before reaching AS layer. The distance from the AS layer to the MU layer is equal to approximately 10 radiation lengths, so most of the electromagnetic particles in an air shower will be absorbed before reaching MU layer and that only muons, hadrons and high energy photons can penetrate to the MU layer. These penetrating component leaves a unique signature in the MU layer of the Milagro detector upon which γ-hadron separation parameters were developed.

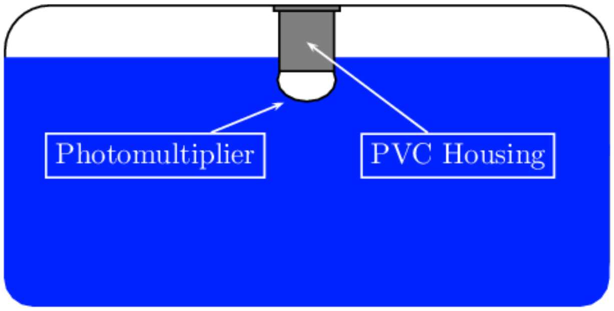

Figure 2.5: Schematic diagram of a single outrigger. Figure taken from [4].

2.1.2 Outrigger Array

The Milagro pond provides a mechanism for the detection of Muons which provides an effective γ-hadron separation method, however the limited size of the pond makes the complete characterization of an EAS difficult. For this reason the outrigger array was included in Milagro design for the purpose of probing the EAS outside the Milagro pond.

The outrigger array covers a 40,000 m^2 area around the central Milagro pond. An outrigger is an individual Cherenkov counter that consists of a 5,680 liter tank of water, measuring 2.4 m in diameter and 1 m in height. Each outrigger is instrumented with a single PMT facing the bottom of the tank. The inside of each tank is lined with Tyvek to reflect light inside the tank. A schematic diagram of an outrigger is shown in figure 2.5.

By extending the physical area of the detector from 5,000 m^2 to 40,000 m^2, the outrigger array allows the determination of the location of the shower core for showers whose cores do not hit the pond. It also improves the angular reconstruction of the air shower by providing a longer lever arm across the shower front to reconstruct the shower direction, and a better curvature correction for showers with cores not on the pond.

2.2 Water System

The Milagro pond holds 6 million gallon of water. The water is filtered and softened before addition to the pond. The constant recirculation rate is 200 GPM. During recirculation the water is filtered through a charcoal filter, a 10 μm filter, a 1 μm filter, a carbon filter, and a 0.2 μm filter to maintain transparency. In addition, the water passes through a UV filter before returning to the pond to prevent any biological growth. To ensure good quality of the water, measurements of the attenuation length of the water are made periodically using a laser unit[18]. Recent tests have shown an attenuation length of 17 m at 325 nm. The bottom of the pond is lined to keep contaminants out of the filtered water.

2.3 Electronics and DAQ System

2.3.1 Signal Extraction

The electronic system collects and processes the PMT pulses and provides the time and pulse amplitude information to computers for online reconstruction of the events. The PMTs are divided into patches of sixteen tubes that operate at the same high voltage level. Each patch is first processed by a custom 16 channel front end board (FEB). The FEB reads in the AC signal from each PMT, and distributes the high voltage (HV) to each tube. The FEB then processes the signal from each PMT and sends it to the digital boards where timing and pulse height information is prepared for digitization.

For each PMT signal, the arrival time and charge must be determined. A straightforward way of doing this would be to employ analog-to-digital converters (ADCs), but due to high cost and high event rate in Milagro the time-over-threshold (TOT) method was used instead.

In the FEB, the signal from each PMT is split and sent to high gain (∼ × 7) and low gain (∼ × 1) amplifiers [21]. These amplified signals are then sent to a pair of discriminators with different photo-electron (PE) thresholds. The signal from the high gain amplifier is sent to a low threshold discriminator with a ∼ 1/4 PE threshold. The signal from the low gain amplifier is split in two, one part goes to a high threshold discriminator with a ∼ 5 PE threshold, while the other goes to an output which can be connected to an external ADC for calibration purposes. When the PMT pulse crosses either of the low or high thresholds, an edge is generated. This is illustrated in figure 2.6. For a relatively small pulse which crosses only the low threshold, two edges are generated. For a pulse that crosses both the low and high thresholds, four edges are generated. The time spent over the threshold can then be calibrated to the charge.

The output of the low and high threshold discriminators are sent to the digital boards. The digital boards multiplexes the signals from the low and high threshold discriminators, and also provide triggering and monitoring information. The edges are then digitized in LeCroy FASTBUS time-to-digital converters (TDCs). The FASTBUS TDCs can record up to 16 edges per event with a 0.5 ns resolution. A FASTBUS latch connected to a GPS clock encodes the common stop time for each event.

2.3.2 Trigger

Before March 19, 2002 Milagro trigger was a simple multiplicity trigger requireing more than ∼ 60 PMTs to generate signals within a 200 ns window. The threshold was set by the maximum data rate the data acquisition system (DAQ) could handle (∼ 2000 Hz). The 200 ns window minimizes random his uncorrelated with the shower. From March 19, 2002 until its failure in April 1, 2006 triggering for Milagro was controlled through a custom built VME (Versa Module Europa) trigger card. This card is programmable allowing the implementation of multiple trigger conditions and

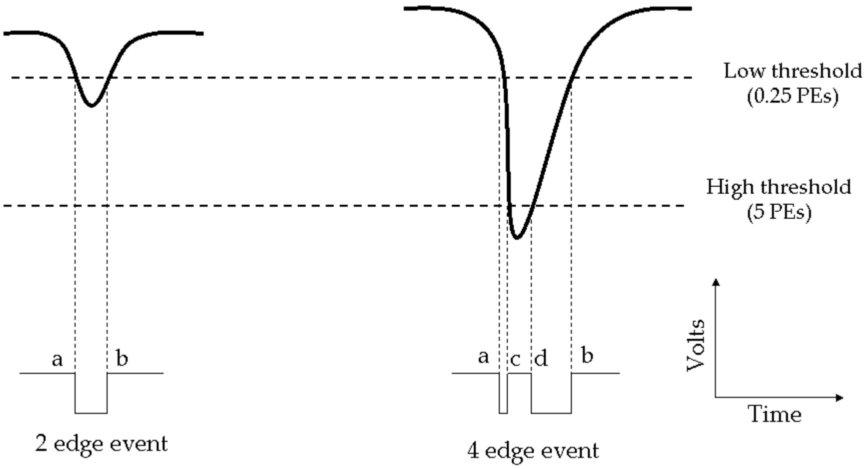

Figure 2.6: A conceptual drawing of the dual TOT method and the logic pulses that result from the technique. Taken from [22]

external triggering[23]. These trigger conditions could be changed to keep the trigger rate below the maximum the DAQ system could handle. The set of trigger conditions that were used when the VME trigger was first installed are as follows:

1. $N_{top} > 20$ & risetime < 50 ns.
2. $N_{top} > 53$ & risetime < 87.5 ns.
3. $N_{top} > 74$.

These values were selected to maximize the number of low energy showers, while keeping the trigger rate at a manageable level of $\sim$ 1800 Hz with $\sim$ 8% dead time. The trigger conditions have been modified over time to keep the trigger rate below the DAQ limit. The simple multiplicity trigger was used again on April 1st, 2006 since the VME trigger card failed on that day.

2.3.3 Data Acquisition System and Online Reconstruction

Following the activation of the trigger card the raw event data is recorded temporarily to a dual ported memory module in the VME crate. The memory module is then read out by the data acquisition computer via a PCI-VME bridge that serves as a link between the detector hardware and the on-site computer network. These events are then send to a computer known as a worker, where the events are decoded, calibrated, and reconstructed. After these tasks are completed the events are then passed back to the main data acquisition computer where they are sorted by time and stored in the appropriate file. Figure 2.7 shows a schematic Milagro computer system.

The raw data are broken into runs and subruns. A new subrun is started every 5 minutes. A new run started at 0:00 UT every day and will last for a whole day unless the DAQ system is shut down by a user, for maintenance, or by external factors like power outage. The raw data consists of the TOT information from each tube and the time of the event. Storing all the raw data would need extremely huge disk space

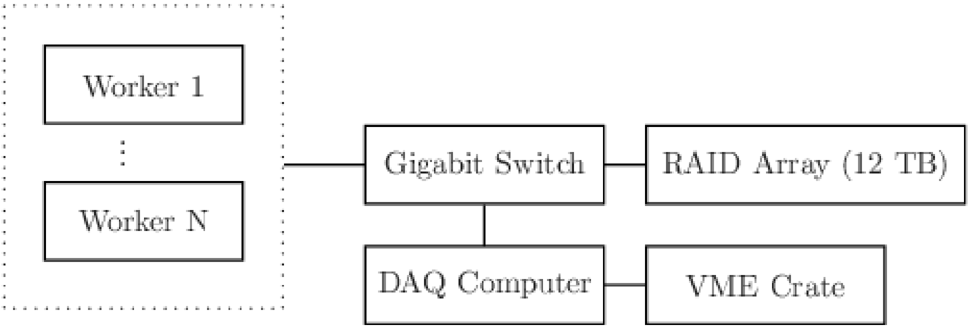

Figure 2.7: Schematic of the on-site Milagro computer system. Taken from [24].

since in one day it will require more than 230 GB of disk space which is equal to $\sim$ 82 TB/year. So raw data are saved only for selected sources, such as the Crab Nebula, the active galaxies Mrk 421 and Mrk 501 when they are flaring, the sun, and the moon. The raw data are also saved when there is a notification, by other experiments, of a GRB that occurred in the field of view of Milagro. All the raw data are calibrated and reconstructed in real time. All of these reconstructed data are saved. The reconstructed data contain information about each reconstructed event which include, the reconstructed direction of the event, core position, event time, the modified Julian date, and timing error information from the GPS clock. The size of disk space required to store all the reconstructed data for one day is $\sim$ 5 GB. The reconstructed data are stored on a DLT (Digital Linear Tape) tapes at the site , and more recently on portable disk arrays, which are then physically transferred for storage in Los Alamos National Laboratory. The reconstructed data are also piped through the network to large redundant disks arrays (RAID) in Los Alamos National Laboratory and University of Maryland.

2.4 Calibration

The timing and charge information is determined using the TOT method. In order to convert the edge times into relative times of hit tubes and the number of PEs, the PMT response must be calibrated. Timing corrections consists two parts. The first part applied accounts for differences in travel times of the PMT pulses through the signal cables and electronics. It is done primarily with a laser calibration system. This system includes a pulsed laser, a filter wheel, and optical fibers that carry the light to a system of diffusing balls placed throughout the pond. The laser fires a set number of pulses of fixed amplitude through a filter wheel which go through optical fiber that connects to an optical switch, allowing the light to be sent to any of the thirty laser balls in the pond. A laser ball is an optical fiber with a sphere of epoxy at the end which diffuses the light out isotropically from the fiber. The filter wheel allows the intensity of the light sent to the pond to be varied. Laser calibration data are taken periodically to produce new calibration constants [3]. In particular, new calibrations are always performed after repairs, since the repaired tubes may have slightly different responses and some tubes may have been replaced together.

The second part of the calibration involves timing corrections. This correction is required because the analog PMT pulses have finite risetime. A large pulse will cross a threshold more quickly than a smaller pulse. This correction is referred to as electronic slewing and is corrected for by measuring the change in start time as a function of TOT using the laser calibration data. The variation of TOT is achieved by varying the position of the filter wheel, and hence the intensity of the light sent to the pond. In addition to this, corrections must be made for the differences in travel times of PMT pulses through the signal cables and electronics.

In addition to the timing calibrations, the calibration of the PMT charge is carried out. As discussed above, in the TOT method an edge is generated whenever the PMT signal crosses one of the high or low discriminator thresholds. The time spent above threshold is proportional to the logarithm of the number of photo-electrons. This relation is determined using the occupancy method, which is based on the fact that, at low light levels, the number of photon-electrons created by the PMT obeys a Poisson distribution. This produces a logarithmic relation between TOT and the number of PEs. The exact relation is determined by the laser calibration.

2.5 Event Reconstruction

After the PMT pulse have been calibrated for a given event, the data are ready to be reconstructed. The times and pulse heights of the tubes which were hit in an event allow the determination of the orientation of the shower plane, and the direction of the primary particle. As the EAS traverses the atmosphere it spreads out laterally, forming the shower front. The orientation of the shower front point back to the direction of the particle which initiated the EAS. The time at which the particles reach the ground will vary within the shower front. This relative timing is used to determine the orientation of the shower plane. Figure 2.8 shows a conceptual drawing of the primary particle direction reconstruction in Milagro.

2.5.1 Core Reconstruction

The first step in analyzing the calibrated information from a triggered event in Milagro is to determine where the core of the incident EAS is located. Over the course of running Milagro, a number of different methods have been used to determine the location of the shower core. The shower core should be associated with the location of the largest number of PMTs hit and with the largest number of PEs. However, the problem is complicated due to the fact that the shower core may be located off the pond. This is in fact the case for most (over 80%) of the events detected by Milagro, which is why the outriggers are so important in determining the location of the core.

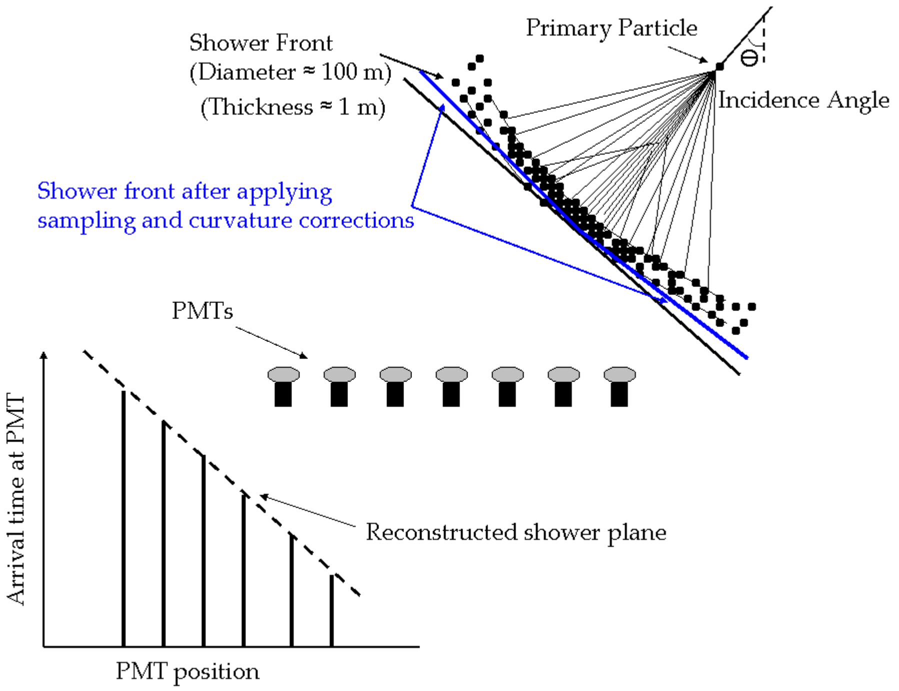

Figure 2.8: Conceptual diagram of the primary particle direction reconstruction in Milagro. Taken from [32].

The first core fitter was a simple center of mass fitter (weighted by the square root of the number of PEs) which put all the cores on the Milagro pond. This was improved by using various methods to determine if the shower core was likely to be located off the pond. If the core was likely to be on the pond, the center of mass core fitter was used; otherwise the reconstructed core location is placed 50 meters from the center of the pond in the direction determined by the center of mass fitter. The value of 50 meters was used because Monte Carlo simulations indicate that this value results in the best agreement, on average, with the true core location.

After the installation of the outriggers, they were used in the core fitter to determine if the core was located on or off the pond. The ratio of the number of outriggers hit to the number of the AS layer PMTs hit provides a good measure of whether the core was on or off the pond. If the core was determined to be off the pond, the center of mass of the outriggers was used to determine the location of the shower core. If the core was determined to be on the pond, the center of mass of the AS layer tubes was used to determine the location of the shower core.

The current core fitter algorithm performs a least square fit to a 2-D Gaussian using the AS layer PMTs and the outriggers. Figure 2.9 shows the distribution of core locations for simulated gamma-ray events that triggered the detector using this core fitter. The error in the core position, determined by comparison to simulated air showers, with known core positions, is shown in figure 2.10.

Once the core position is known, a correction is applied to adjust for the curvature of the shower plane. In addition to correcting for the curvature of the shower front, a correction must be made for the way in which the shower front is sampled. Since the time of each hit is recoreded as the arrival time of the first Cherenkov photon, the arrival times of tubes hit near the core will be slightly earlier than those hit further from the core. Once both of these corrections have been made, it is possible to reconstruct the angle of incidence of the primary particle.

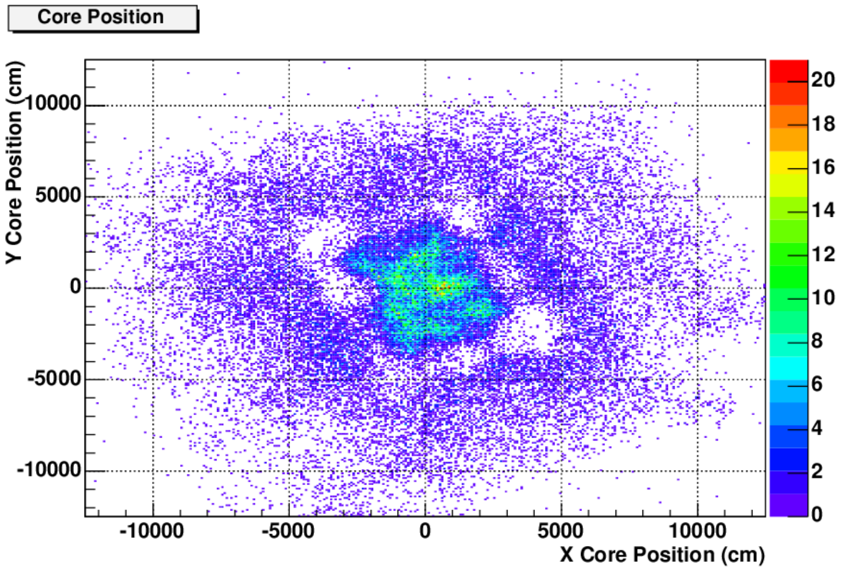

Figure 2.9: Reconstructed core positions for simulated gamma-ray events that triggered the detector using the current 2-D Gaussian fitter.

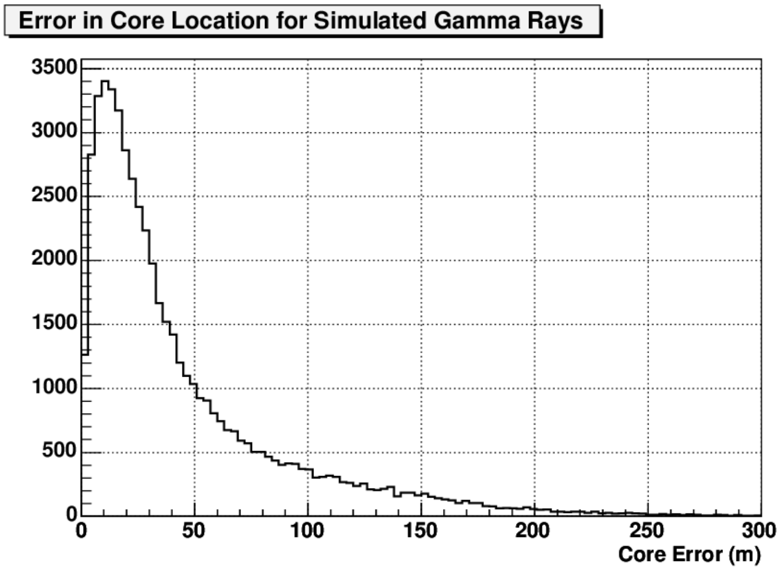

Figure 2.10: Error in the reconstructed core position. The true core position from the simulation is compared to the fitted core position.

2.5.2 Angular Reconstruction

In order to determine the origin of a γ-ray primary for a single event detected with Milagro an angular reconstruction algorithm has been formulated. The shower front of an extensive air shower has a finite thickness. It is thinner near the shower core and thicker near the edge of the shower. This thickness in the shower front is due to the lower energy secondary particles, which are present near the shower edge, suffering more scattering than the higher energy ones that are present near the shower core. The shower front is fit to a plane using an iterative least squares fit. The tubes are weighted by the number of PEs, and several iterations are made based on the number of PEs. The residuals of small PE hits are very non-Gaussian, so only larger PE hits are used in the first iteration of the fit. The residuals from the fit are calculated, and if they are within a pre-set range they are retained for the second iteration, otherwise they are excluded. On the second iteration the large PE requirement is relaxed, allowing more tubes to come into the fit. This process is repeated five times. Using this method $\sim 90\%$ of triggered data is successfully fit.

The outriggers were used in the angular reconstruction after they were installed. The addition of the outriggers improved the angular resolution of the detector by giving a longer lever arm to reconstruct the shower. Using this technique the angular resolution of Milagro is approximately 0.7° (see figure 2.11) with the application of quality cut ($N_{fit} > 40$ and $X2 > 2.5$, which will be discussed in next chapter).

2.6 Simulations

There are two steps in the process to simulate the response of Milagro detector to EAS. In the first step, the EAS are simulated by a software package known as CORSIKA [19]. The simulation of an EAS with CORSIKA begins with the first interaction of the primary particle in the atmosphere, then proceeds to track the subsequent

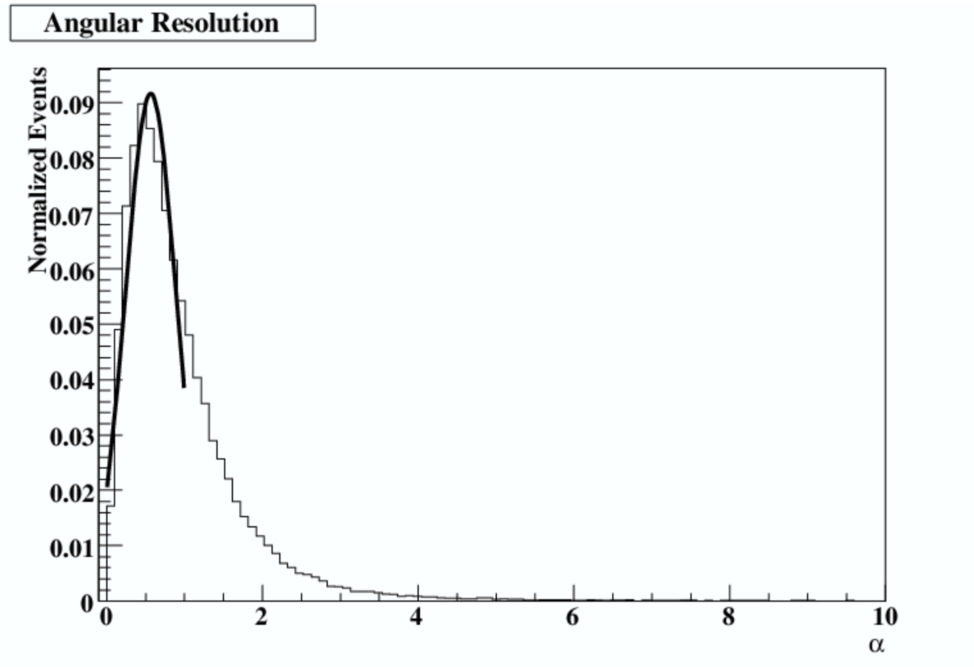

Figure 2.11: The distribution of the space angle difference (α between the reconstructed angle and the true angle of γ-ray primaries for energies between 0.1 and 100 TeV. Taken from [4].

Parameters	Simulation Range
Zenith Angle	$< 45^\circ$
γ-Ray Energy	30 GeV - 100 TeV
Core radius	< 1 km

Table 2.1: Parameter ranges used for Monte Carlo simulated γ-ray air showers.

interactions of the secondary particles to the ground level. The second step is to simulate the detector's response to EAS, and is performered using a software package known as GEANT4 (GEometry ANd Tracking)[20]. The input for the second step is the information about the shower particles reaching the ground. The GEANT4 software takes these particle and propagates them through a model of the Milagro detector. All the interactions, hadronic and electromagnetic, for both the charged particles, as well as the input photons, are simulated by GEANT4. These interactions include the production of Cherenkov light and γ-rays within the detector.

In order to obtain enough statistics, especially for high energy particles, hundreds of millions of CORSIKA showers were generated. The primaries that were thrown are γ-rays, protons and heliums. The range of zenith angle, initial particle energy, and shower core location used to generate simulated events are chosen to represent the full set of γ-ray air showers that can trigger the detector, be reconstructed , and pass analysis cuts. The shower core location is defined in terms of the radius from the center of the pond. The ranges of parameters used for the simulated γ-ray air showers are shown in table 2.1[1]. These were selected such that showers with parameters outside this range are detected with negligible efficiency and can be ignored. The showers were thrown with a power law spectrum of $dN/dE \propto E^{-2.0}$. At the analysis stage, the events were properly re-weighted for γ-ray spectral index other than -2.0 and for proton ($\alpha = -2.75$) and helium ($\alpha = -2.68$) showers.

---

[1] for proton and helium showers the zenith angle range is from 0° to 70°.

Chapter 3

Milagro Data and Analysis

3.1 Background Determination

The method to search for a point source of ultra high energy γ-rays is to count the number of events in an angular bin in celestial coordinates containing a possible source and compare this with the number of background events expected in this bin. After these are obtained, the statistical significance of the result can be calculated using the method of Li and Ma [25], which will be discussed in section 3.2. Since the number of background events is much larger compared with the signal events, the emission from a source would appear as a relatively small excess of events above the background coming from the direction of the source. It is crucial to correctly estimate the background events. If the background is underestimated, a fluctuation of the background could appear as a signal and if the background is overestimated, it will wash out any real signal.

3.1.1 Direct Integration Method

In Milagro analysis the direct integration method[27] was used to estimate the background. This method utilizes background rate information from the same regions in the local sky, and a data method to account for changes in the overall event rate. It assumes that the efficiency for detecting events depends on the local angles (zenith and azimuth) and remains approximately constant for short periods of time. The angular distribution of accepted events is assumed to be independent of the event rate. For this analysis, an integration period of two hours was selected. The number of background events expected to fall within a bin $\Delta(\mathrm{RA})$ in right ascension and $\Delta(\delta)$ in declination is given by

$$N_B(RA,\delta) = \int\int E(HA(t),\delta)\ Rate(t)\ \epsilon(HA(t),RA,t)\ dHA\ d\delta\ dt \tag{3.1}$$

where $N_B(RA,\delta)$ is the background estimate within a bin at equatorial coordinates (RA,δ), E(HA(t),δ) is the detector efficiency at local coordinate (dHA(t), dδ), and $\epsilon = 1$ if an event falls in the (RA,δ) bin at sidereal time t and $\epsilon = 0$ otherwise. The hour angle, HA(t), is a function of sidereal time given by:

$$HA(t) = t - RA \tag{3.2}$$

and this equation provides the conversion from the local, rotating acceptance coordinates to the static equatorial coordinates.

The events in the sky are binned in $0.1^\circ \times 0.1^\circ$ bins. The number of events in each of these bins is divided by the total number of events observed in the integration period to get an efficiency map. At the end of the two hours background integration period, the efficiency map is converted into a background map in equatorial coordinates (RA,δ) by using the rate of events collected for each 24 seconds of time. The size of the time bin is 24 seconds to eliminate appreciable motion of the sky within the angular bin of 0.1°. This ensures that the background events have the same time distribution as the collected data. Figure 3.1 is a schematic view to show this direct integration method.

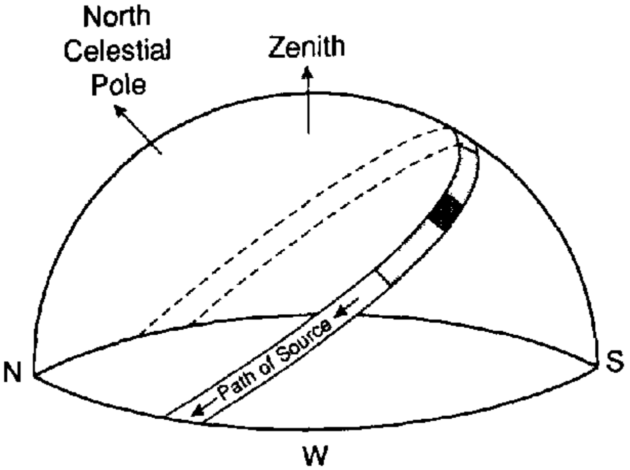

Figure 3.1: A schematic view of the sky showing the path of a source within a given declination band over a day. The source bin is darkly shaded while the bins used to estimate the background with the direct integration method are lightly shaded. Taken from [27]

3.1.2 Region of Interest (ROI)

In some places the background are overestimated because the events from the γ-ray sources are included. In Milinda, Milagro's standard analysis, some of known sources were removed before the background map was generated. These regions include $3^\circ \times 3^\circ$ around the Crab Nebula and Mrk 421. The region in the Galactic plane $l \in [10^\circ, 90^\circ]$ and $|b| < 2.5^\circ$ is also excluded. In Milagro these regions are called Region of Interest (ROI) After the estimation of the background the map can be smoothed either by bin smoothed method or by the point spread function (PSF) of Milagro. Details are in section 3.3 and 3.4.

3.2 Determing the Significance of a Measurement

After estimating the background we can calculate the statistical significance of an excess (or deficit) for each point in the sky. This is done using the method of Li and

Ma[25]. In this method the measure of significance, S:

$$S = \sqrt{2}\sqrt{N_{on}\ln\left(\frac{(1+\alpha)}{\alpha}\frac{N_{on}}{(N_{on}+N_{off})}\right) + N_{off}\ln\left((1+\alpha)\frac{N_{off}}{(N_{on}+N_{off})}\right)} \tag{3.3}$$

where N_{on} is the number of events in the signal bin, N_{off} is the number of events in the background bin, and α is the ratio of signal to background exposures and is given by:

$$\alpha(\delta) = \frac{\frac{B}{\cos\delta}}{I - f\frac{B}{\cos\delta}} = \begin{cases} \frac{\frac{B}{\cos\delta}}{I-\frac{B}{\cos\delta}} & \text{(if outside ROI, f=1)} \\ \\ \frac{\frac{B}{\cos\delta}}{I} & \text{(if inside ROI, f=0)} \end{cases} \tag{3.4}$$

Where B is the bin size, δ is the declination of the bin at which the significance is to be calculated, and I is the total bin size of the integration time in the RA direction, 30° in this case. $\frac{B}{\cos\delta}$ is the signal exposure in degrees, and $I - f\frac{B}{\cos\delta}$ is the background exposure in degrees. If the bin is in the ROI, then it is already not included in the background map generation, so it does not need to be subtracted again in the denominator of equation 3.4. The factor f is discussed and defined in section 3.3.

Although the Li-Ma prescription requires that N_{on} and N_{off} be ≥ 10 [25], in fact the Li-Ma significance follows a standard normal distribution quite well even in the case of a small expected background count in a signal bin[26].

3.3 Bin Smoothed Method and Optimal Bin Size

Milagro signal and background event maps are initially binned in $0.1^\circ \times 0.1^\circ$ bins. But 0.1° is substantially smaller than Milagro's angular resolution[1]. This indicates that events originating from a point source in the sky will occupy many of the surrounding

---

[1] It is $\sim 0.9^\circ$ for pre outrigger data and $\sim 0.35^\circ$ for post outrigger data.

bins. In order to account for this effect a smoothing process is carried out, where 0.1° bins are combined into a larger square bin, also called search bin, for the computation of source excess and significances. This is the bin smoothed method.

A small search bin contains less background events but not enough signal events. On the other hand, a large search bin contains most of the signal events, but the background is also large and may overwelm any signal. The optimal source bin (the bin that, on average, maximizes the ratio of signal strength to the square root of the background level) is a round angular bin centered on the source with an angular radius of 1.58 σ, where σ is the rms projected angular resolution of the detector[27]. On average, this bin will contain 72% of the signal from a point source. A square bin with approximately the same angular area as the optimal round bin is only slightly inferior and is easier to computationally use. A signal with a significance corresponding to an n-standard-deviation fluctuation of the background in an optimal round bin would be expected to yield ~ 0.985 n-standard-deviation significance in an optimal square bin. The optimal square bin width for the Milagro data is $\sim 2.1^\circ$. When using the bin smoothed method the bin size is also scaled to have equal area on the sky. This requires the width in RA to be scaled by $1/cos(\delta)$. The resulting bin is rectangular with a width of $2.1^\circ/cos(\delta)$ in RA and 2.1° in δ.

For the bin smoothed method the search bin can be total inside ROI, outside ROI, or partially inside ROI. The factor f in equation 3.4 is given by:

$$f = 1 - \frac{N_{ROI}}{N} \tag{3.5}$$

where N_{ROI} is the number of events of the search bin inside the ROI, and N is the total number of events in the search bin.

3.4 PSF Smoothed Method

Using the binned method to search a point source is conceptually simple but there are ways to achieve better sensitivity to a signal. Some of the real source events are contained in background bins. In addition, if there is a real signal, the relative probability of coming from the source (compared with being background) is higher for events near the true source location. However, the binned method treats all events inside the source bin equally. The PSF smoothed method estimates the signal size from the distribution of event locations and can be more sensitive to signals than binned method.

The PSF smoothed method computes a weighted sum of events from a given source position. The weight for each event is given by the probability for that event to have come from the source, typically parameterized as the probability density function (PDF) for signal events. The normalized PDF for signal events, P_s, is typically a properly normalized two-dimensional Gaussian of width equal to the detector's angular resolution. The angular resolution is,

$$P_s(\theta_s) = \frac{\theta_s}{\sigma^2} \, exp(\frac{-\theta_s^2}{2\sigma^2}) \tag{3.6}$$

where θ_s is the space angle between the measured event direction and the true point source direction, and σ is the detector's angular resolution. The background events can be obtained in the manner discussed in section 3.1. After getting the number of events in each signal bin and background bin, the significance for each $0.1^\circ \times 0.1^\circ$ bin can be calculated using the technique described in section 3.2. θ_s and σ in equation 3.6 are fitted for the whole Milagro data. The detailed fitting results can be found in Aous Ahmad Abdo's Ph.D. thesis [32].

The PSF smoothed maps α in equation 3.3 needs to be corrected[28]. When doing the PSF smoothing Milagro's standard code, milinda, reads the bin size as

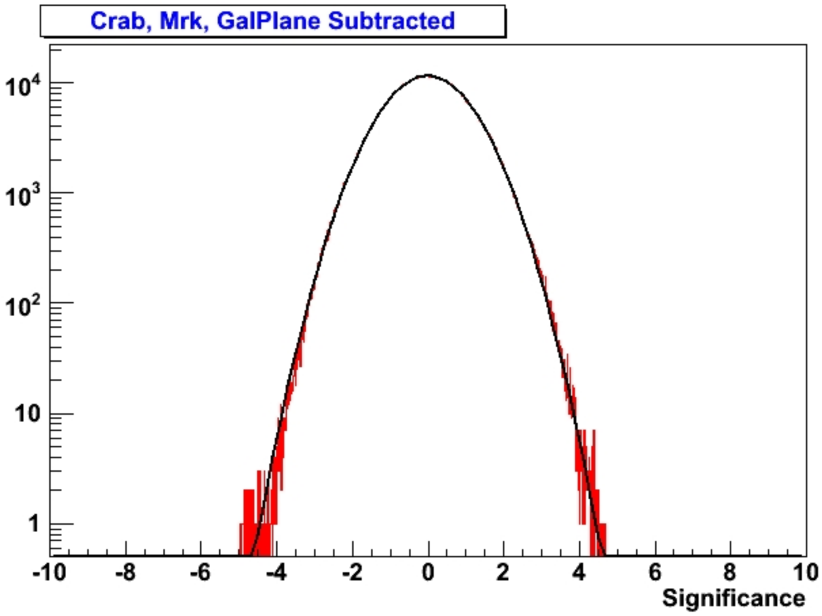

Figure 3.2: Distribution of significances of the Milagro all sky map with the region of interest subtracted

0.1°, so α is too small. This has the effect of making the significances inside ROI too high by a factor of $\sqrt{1+\alpha_{true}}$ (α_{true} is the true α). The significances outside the ROI are too low the same factor. To correct for this effect, simulation was used to estimate the effective bin size for the PSF smoothing. Results show that the effective bin size is $3.6\times\sigma_{PSF}$, which σ_{PSF} is the sigma used to PSF smoothed the maps. This result was used to find α for the whole Milagro dataset. Figure 3.2 shows the significance distribution for the sky with the region of interest subtracted. The fit to the distribution has the width of 1.026, which is consistent with the expected width of 1.

3.5 γ-Hadron Separation Techniques and Variables

The cosmic-ray background is very large in comparison to γ-ray signals. So the implementation of an effective γ-hadron rejection algorithm is very important to the analysis. The background events in Milagro can be removed using the different properties of γ-ray induced and cosmic-ray induced air showers. Milagro's two layer design is used for the purpose of γ-hadron separation. The air shower layer and outrigger array are primarily used in order to reconstruct the event directions and core positions of EAS's while the muon layer is used to search the presence of penetrating particles in the EAS, such as muons, which are more prevalent in the background showers.

For each air shower event that is detected by Milagro, it is not known if the primary particle is a γ-ray or a cosmic ray. However, we can attempt to identify the primary particle by statistical means. The γ-ray initiated EAS at ground is composed primarily of electrons, positrons, and low-energy γ-rays. The top layer in Milagro is placed under ~ 4 radiation lengths and ~ 2 interaction lengths of water. Before the top layer most of the γ-rays that enter the pond will be converted to electron-position pairs. These relativistic charged particles will generate Cherenkov radiation in the water and will illuminate the PMTs in the Top layer. The muon layer in Milagro is located ~ 17 radiation and ~ 7.2 interaction lengths under the water. Most γ-ray initiated charged particles that enter the pond will be absorbed before reaching the muon layer. On the other hand, an EAS induced by a cosmic ray contains muons and hadrons, both of which are more penetrating in water than photons or electrons. The muon layer can be used to identify these kind of events. The muons and hadrons which reach the muon layer illuminate a relatively small number of tubes in a small region. Figure 3.3 shows the distribution of light in the muon layer PMTs for simulated γ-rays (bottom) and proton (top) induced air showers. As can be seen in the figure, the γ-ray events have relatively smooth PE distributions in the muon layer while the proton events have more clumpy distributions in the muon layer. This property can be used to find the γ-hadron separation parameters.

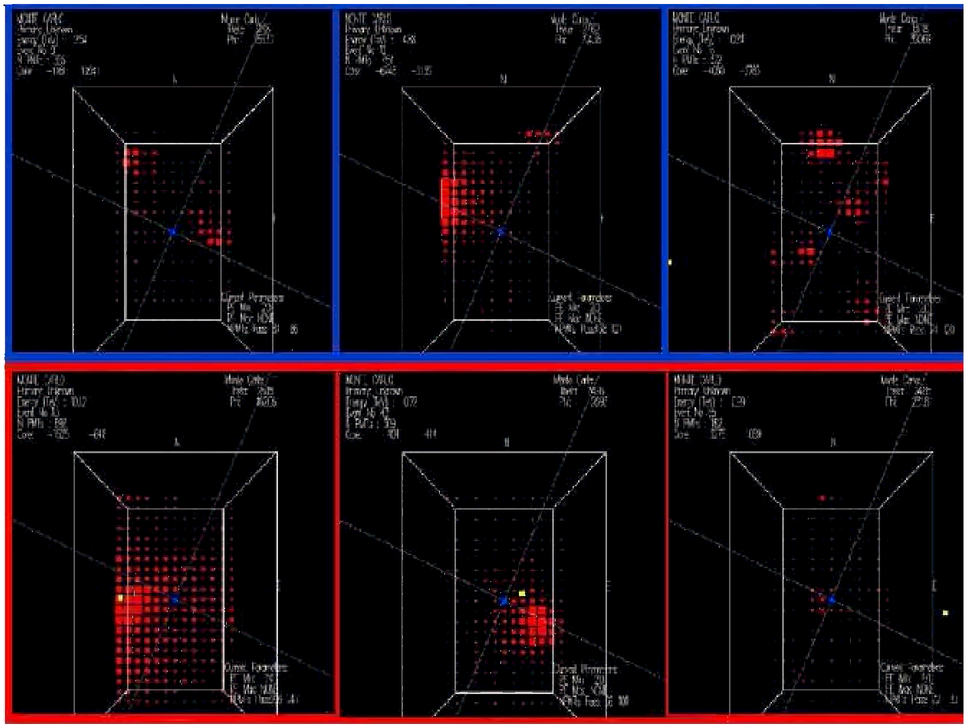

Figure 3.3: Differences between simulated γ-ray (bottom) and proton (top) induced air showers.

3.5.1 $X2$ Parameter

The first method [29, 30, 31] for distinguishing γ-rays and hadronic cosmic-rays uses the $X2$ parameter:

$$X2 = \frac{N_{MU \geq 2PEs}}{PE_{max}} \tag{3.7}$$

Where $N_{MU \geq 2PEs}$ is the number of PMTs hit in the muon layer with more than 2 PEs, and PE_{max} is the maximum PE value in the muno layer. For cosmic ray events where there is an uneven distribution of PEs (clumpy) the value of $X2$ will be small. For events due to γ-ray primaries the number of PEs in each PMT in the muno layer is approximately equal, the value of $X2$ will increase substantially. Therefore, hadronically initiated shower typically have small values of $X2$, while γ-ray initialed showers typically have large values of $X2$. Distributions of the parameter $X2$ for simulated γ-ray showers, simulated cosmic-ray showers, and data events are shown in Figure 3.4. As we can see in the figure, the data and simulated cosmic-ray showers agree well and both of them have smaller values of $X2$ than the simulated γ-ray showers.

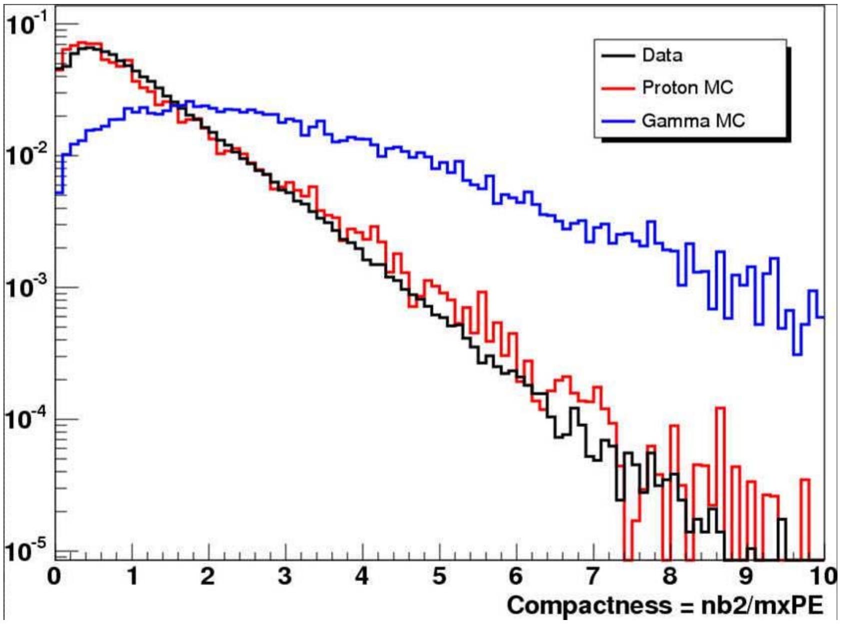

Figure 3.4: $X2$ distribution for simulated γ-ray showers (blue), simulated cosmic-ray showers (black), and data (red). The horizontal axis is the $X2$ value. Taken from Jordan Goodman's talk.

The relative increase in sensitivity for a given selection criterion can be given by a quality factor, which is defined as

$$Q(X2) = \frac{\epsilon_\gamma}{\sqrt{\epsilon_p}} \tag{3.8}$$

Where ϵ_γ and ϵ_p are the efficiencies for retaining the γ-rays and cosmic-rays (most of them are protons) given certain cut.

In Milagro analysis the optimum $X2$ cut is 2.5 which is determined by the maximum Q-factor with the greatest ϵ_γ. The number of PMTs used in the angular fit is 20. These cuts reject 89.0% of the simulated cosmic-ray induced air showers and 90.0% of the data, while retaining 39.0% of the γ-ray induced air showers. This results in a relative increase in Q-factor of 1.18 and 1.23 when comparing the simulated γ-rays to simulated cosmic-rays and data respectively.

The effectiveness of the $X2$ γ-hadron separation parameter was first demonstrated by the observations of the Crab Nebula and examination of the significance before and after the application of an $X2$ cut using a data set spanning from June 1999 until September 2002. Without the $X2$ cut the significance of detection for the Crab Nebula was 1.9 σ, where after the application of the $X2$, the significance of the Crab increased to 6.4 σ [31].

3.5.2 A_4 Parameter

From 2000 to 2003 Milagro installed 175 outriggers which surround the Milagro pond. The outrigger array allows a more accurate determination of the location of the shower core, which is important in the angular reconstruction. The $X2$ parameter does not carry information about the size of the air shower and how well the shower is fit. A new γ-hadron separation variable, named A_4, was found by Aous Ahmad Abdo [32]. A_4 is defined as:

$$\mathrm{A}_4 = \frac{(f_{top} + f_{out}) \times N_{fit}}{PE_{max}} \tag{3.9}$$

Where f_{top} and f_{out} are the fraction of the PMT's triggered in the air shower layer and outriggers, N_{fit} is the number of PMTs used in the angle fit and PE_{max} is the maximum number of PE's detected by a single tube in the muon layer for a single event.

The first part in the numerator of A_4, $f_{top}+f_{out}$, carries information about the size of the shower. The second part in the numerator, N_{fit}, carries information about how well the shower is reconstructed. The denominator of A_4, PE_{max}, carries information about the clumpiness in the muon layer that is due to the penetrating muons and hadrons which are mostly in hadronic air showers.

Figure 3.5 shows the A_4 distribution for the simulated γ-rays, simulated cosmic-rays and data. The cut $A_4 \geq 3.0$ rejects 94.4% of the simulated cosmic-ray induced air showers and 97.2% of the data, while retaining 27% of the γ-ray induced air showers. This result in a relative increase in Q-factor of 1.62 and 1.59 when comparing the simulated γ-rays to simulated cosmic-rays and data respectively, which is better than the improvement of ~ 1.4 relative to the $X2$ cut. The details of the properties of A_4 such as the energy dependence, the core location dependence, and zenith angle dependence can be found in Aous' PhD thesis [32].

Figure 3.6 shows a map of the statistical significance in the Crab region with the $A_4 \geq 3.0$ and $\mathrm{N}_{fit} \geq 40$ using Milagro data set from September 2003 until May 2005. In this map the statistical significance in the location of Crab Nebula is 8.02 σ. Figure 3.7 shows the significance of Crab Nebula using $X2 \geq 2.5$ and $N_{fit} \geq 20$ cuts for the same data set is 5.34 σ. The significance of Crab Nebula increases $\sim$ 50%.

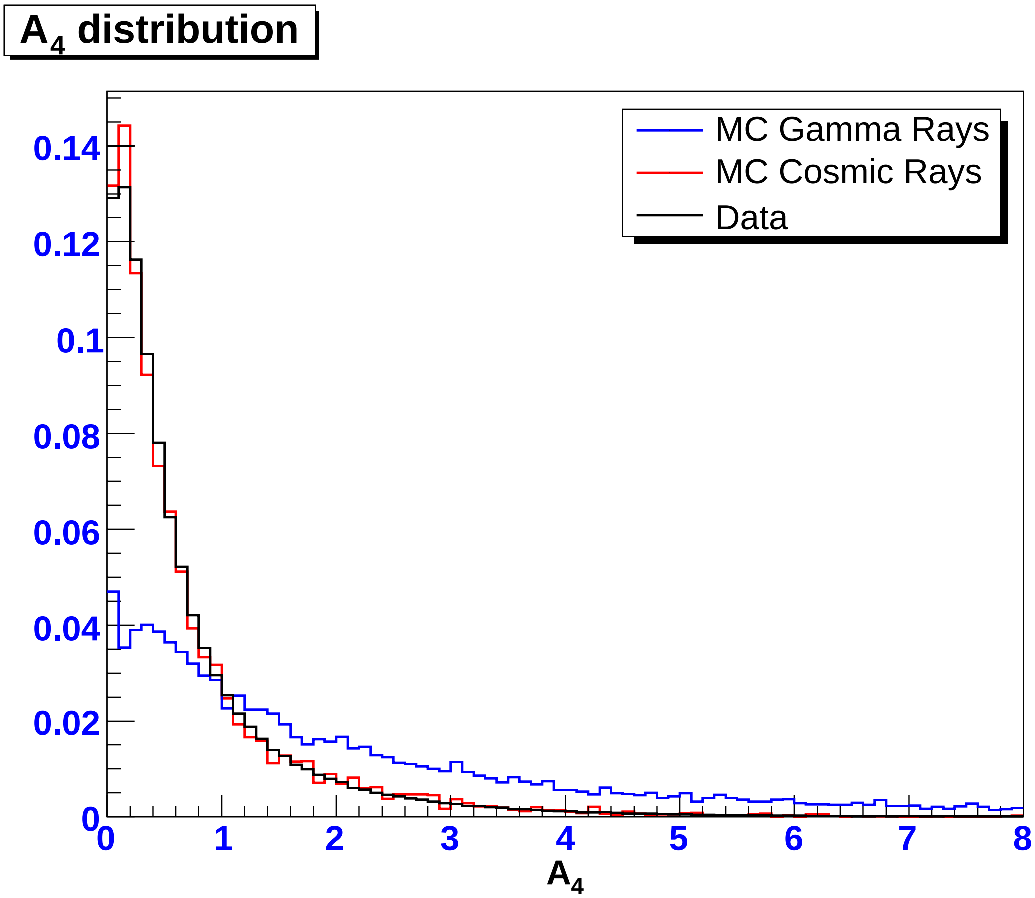

Figure 3.5: A$_4$ distribution for simulated γ-ray showers, simulated cosmic-ray showers, and data. All of the histograms have been normalized to have unit area. Figure taken from [32]

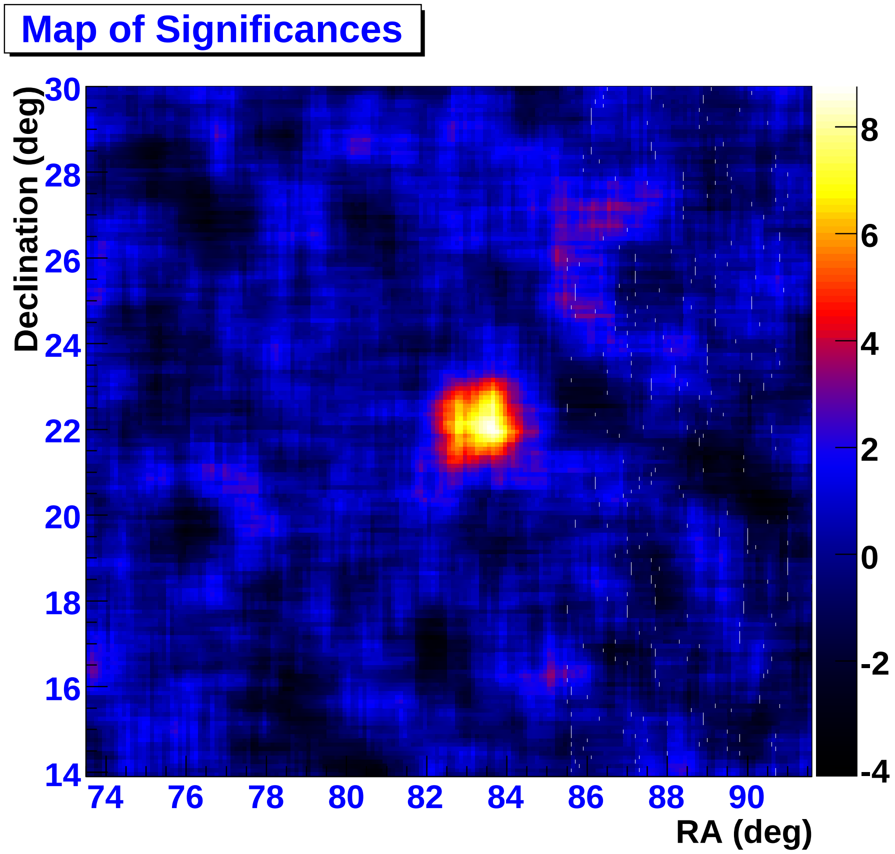

Figure 3.6: Map of the significance around the Crab Nebula with the $A_4 \geq 3.0$ and $\mathrm{N}_{fit} \geq 40$. Taken from [32]

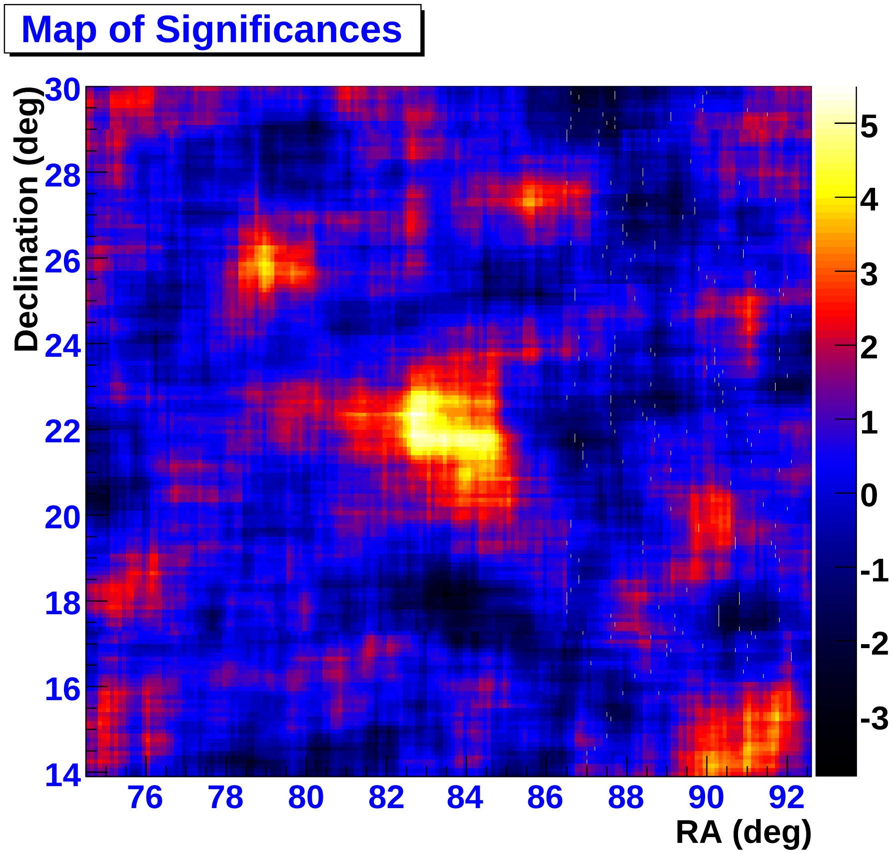

Figure 3.7: Map of the significance around the Crab Nebula with the $X2 \geq 2.5$ and $\mathrm{N}_{fit} \geq 20$. Taken from [32]

Chapter 4

Weighted Analysis Technique

4.1 Milagro Data Set and Epochs

The Milagro data in the analysis of this thesis was taken between July 19, 2000 and October 31, 2007, a total of 2659 days. During this time some of the archived set of reconstructed data which includes runs that have been taken under special conditions are excluded from this analysis. These special runs used non-standard trigger levels to get a sample of events at low trigger levels, test the trigger card or take ADC calibration data, corrupted data due to buffers with overwrites were also removed. Runs containing less 10 sub runs were exclude from the analysis.

During Milagro operation time, there were significant upgrades such as installation of outriggers, different reconstruction algorithms, and different calibration software. Also different trigger types and trigger conditions were used. In order to take into account these changes, the Milagro data has to be split into epochs. Details of each Milagro epoch are listed in Table 4.1. This table includes the start dates of the epochs, the trigger methods, and the core finders used in the event reconstruction[33]. Different simulation sets were generated for different epochs. Seven simulated data sets are available for the nine data taking periods. The same simulated data set is

Epoch No.	Start date	No. of Days	Core Finder	Trigger
1	07/19/2000	109.5	COM	Multiplicity
2	12/10/2000	334.5	Off Pond	Multiplicity
3	01/11/2002	380.8	Off Pond	VME
4	05/18/2003	418.6	Outrigger COM	VME
5	10/06/2004	146.3	3 Layer	VME
6	04/01/2005	141.2	2 Layer	VME
7	09/20/2005	151.4	2 Layer	VME
8	03/17/2006	242.9	2 Layer	mostly Multiplicity
9	01/11/2007	259.5	2 Layer	Multiplicity

Table 4.1: Nine epochs of collected data that are used in this analysis.

used for epoch 2 and 3, and the same simulation is used for epochs 8 and 9. The number of days in each epoch[1] is also listed in Table 4.1.

4.2 Motivations for Weighted Analysis

Andy Smith, a Milagro collaborator at the University of Maryland, developed a method for weighted analysis of Crab data[34]. This method is based on the fact that the significance of the excess from the Crab is almost independent of the γ-hadron cuts applied. When compared to Milagro standard cut ($N_{fit} \geq 20$, $X2 > 2.5$), similar significance is obtained for harder cuts like $N_{fit} \geq 175$ and $X2 > 5.5$. So this phenomenon indicates that the significance of the excess can be substantially increased by combining the independent results from the softer and harder cuts to form a single result of higher significance. Because the signal-to-background ration (S/B) increases when we use harder cuts, which can be seen from table 4.2, events passing harder cuts are more likely to be γ-rays, rather than cosmic-rays.

Similarly, the signal-to-background ratio increases with increasing A_4[32]. When a harder A_4 cut ($A_4 \geq 12.0$) applied on a Crab data set the S/B ratio is higher (60.0%) compared to that with $A_4 \geq 3.0$ (S/B=3.4%). So the events with the higher

---

[1] It is the total integration time of each epoch multiplies by a factor of 0.9 to account for the average instrumental dead time.

Slice	Cuts	Expected No of gammas	Measured bkg total ($\times 10^6$)	Weight
1	(NF$\geq$ 20 && $X2 > 2.5$)&& !(NF$\geq$ 50 && $X2 > 3.0$)	1933	265	1
2	(NF$\geq$ 50 && $X2 > 3.0$)&& !(NF$\geq$ 75 && $X2 > 3.5$)	951	87	1.5
3	(NF$\geq$ 75 && $X2 > 3.5$)&& !(NF$\geq$ 100 && $X2 > 4.0$)	550	30	2.51
4	(NF$\geq$ 100 && $X2 > 4.0$)&& !(NF$\geq$ 100 && $X2 > 4.0$)	366	11.4	4.4
5	(NF$\geq$ 125 && $X2 > 4.5$)&& !(NF$\geq$ 150 && $X2 > 5.0$)	263	4.39	8.2
6	(NF$\geq$ 150 && $X2 > 5.0$)&& !(NF$\geq$ 175 && $X2 > 5.5$)	194	1.71	15.6
7	NF$\geq$ 175 && $X2 > 5.5$	145	0.9	22.1

Table 4.2: List of cuts applied for each $N_{fit} - X2$ bin. The weight is the ratio of the number of γMonte Carlo events to the number of background events passing the cuts. All weights have been normalized that of the first bin. Table taken from [34]

A_4 values are more likely to be γ-rays than the events with lower A_4 values.

The fact that one can achieve a high S/B ratio when applying harder $X2$ or A_4 cuts led to the development of the weighting analysis technique. The technique weights events based on the relative probability that the event was due to a γ-ray, rather than a cosmic-ray. Events with different $X2$ or A_4 values are not counted equally. Instead a weighted sum of events is used where events with higher $X2$ or A_4 values are assigned higher weights. Using this weighting technique will give the best estimate of significance or flux. The weights can be simply assigned as the ratio of expected Monte Carlo γ-ray evens to the measured background events in each $X2$ or A_4 bin [35].

4.3 Determining the A_4 Weights

This section describes the A_4 weighting procedure. It is similar for N_{fit}-$X2$ weighting procedure [4]. Then the results of A_4 weights using two different methods are compared. The first method uses simulated γ-ray events and Milagro background events to derive the A$_4$ weights. The second method uses simulated γ-ray events and simulated background events to derive the A$_4$ weights with error bars. The significance of Crab Nebula demonstrates the improvement of A$_4$ weighted analysis. Finally, the median energy for the unweighted $X2$ and weighted A$_4$ analyses are discussed.

4.3.1 A$_4$ Weighting Procedure

The A$_4$ weighting procedure is carried by assigning to each event a weight that is equal to the expected signal to background ratio within discrete A$_4$ bins. In each of these bins, events with A$_4$ value greater than or equal to the lower end of the bin and smaller than the upper end of the bin are kept in that bin, i.e., only events that satisfy the criteria

$$b_i^{min} \leq A_4 < b_i^{max} \tag{4.1}$$

are kept in the ith bin. Table 4.3 lists the A$_4$ bins used for each epoch. The weights assigned for the ith bin is equal to

$$w_i = \frac{S_i}{B_i} \tag{4.2}$$

where

- S_i is the number of Monte Carlo γ-ray events expected in the ith A$_4$ bin.

- B_i is the number of measured background events in the same bin.

All weights have been normalized to that of the first bin. Table 4.4 lists the A$_4$ weights for each epoch that I used to analyze EGRET sources with Milagro data in Chapter 6.

Pre Outrigger. Epochs 1-3												
Bin Number(i)	1	2	3	4	5	6	7	8	9	10	11	12
b_i^{min}	0.5	1.0	1.5	2.0	2.5	3.0	3.5	4.0	4.5	5.0	5.5	6.0
b_i^{max}	1.0	1.5	2.0	2.5	3.0	3.5	4.0	4.5	5.0	5.5	6.0	∞
Post Outrigger. Epochs 4-9												
Bin Number(i)	1	2	3	4	5	6	7	8	9	10	11	12
b_i^{min}	1	2	3	4	5	6	7	8	9	10	11	12
b_i^{max}	2	3	4	5	6	7	8	9	10	11	12	∞

Table 4.3: A_4 Bins. b_i^{min} and b_i^{max} represent the lower and upper edges of the A_4 bin respectively.

	Weights								
Bin N<u>o</u>	E1	E2	E3	E4	E5	E6	E7	E8	E9
1	1.00	1.00	1.00	1.00	1.00	1.00	1.00	1.00	1.00
2	2.38	2.25	1.87	2.10	2.07	1.83	1.34	1.47	1.47
3	4.60	4.08	2.82	3.69	3.43	2.70	1.62	1.72	1.72
4	8.26	7.11	4.12	5.96	5.11	3.98	1.64	2.22	2.22
5	13.08	11.23	5.51	10.72	7.17	5.26	2.01	2.43	2.43
6	20.28	16.25	6.78	15.32	9.45	6.92	2.08	2.91	2.91
7	29.27	22.04	7.76	17.25	15.93	11.13	2.81	3.70	3.70
8	42.12	27.18	7.96	21.74	20.15	14.81	3.47	4.88	4.88
9	49.72	37.51	8.92	23.88	30.90	20.72	4.56	5.67	5.67
10	51.83	35.34	6.66	22.44	45.75	30.91	5.48	6.50	6.50
11	72.23	55.35	8.02	23.95	62.71	45.31	6.87	8.54	8.54
12	116.17	97.32	10.50	44.22	100.33	116.02	8.24	10.25	10.25

Table 4.4: Gamma-hadron weights for the different epochs. In each epoch, the weights have been normalized to that of the first A_4 bin. Table taken from [32]

4.3.2 Weighted Analysis Using Monte Carlo Events and the Studies of Uncertainties

The Monte Carlo simulated events are weighted in energy E and position r, and statistical errors are introduced[36]. I revised Sensi program of MMCAnalysis.cc in Milinda, the Milagro software, to calculate γ-ray and cosmic-ray Monte Carlo events from a source with a Crab-like spectrum of $E^{-2.62}$ and at Crab declination as well as their errors[37]. For example, the number of γ-ray from the Crab is 14.399 ± 0.258 events/day for $N_{fit} > 40$ and $A_4 > 1.0$ cuts.

The weight of each A_4 bin is the ratio of the expected number of γ-ray events to the expected background (proton and helium) events passing the cuts. Since the weight is relative, the weight for bin 1 is defined to be 1.0 and the other weights are computed relative to it. Assume the weight for the i^{it} bin is $weight[i]$. Then

$$weight[i] = (\frac{ngamma[i]}{nproton[i]})/(\frac{ngamma[1]}{nproton[1]}) \tag{4.3}$$

where

- $ngamma[i]$ is the number of γ-ray events in the i^{th} A_4 bin.
- $nproton[i]$ is the number of background events in the i^{th} A_4 bin.
- $ngamma[1]$ is the number of γ-ray events in the first A_4 bin.
- $nproton[1]$ is the number of background events in the first A_4 bin.

After propagation of uncertainties the error of the A_4 weight of the i^{it} bin is:

$$\begin{aligned} weighterr[i] &= weight[i]\times \\ &\sqrt{(\frac{ngerr[i]}{ngamma[i]})^2 + (\frac{nperr[i]}{nproton[i]})^2 + (\frac{ngerr[l]}{ngamma[1]})^2 + (\frac{nperr[1]}{nproton[1]})^2} \end{aligned} \tag{4.4}$$

where

- *ngerr*[*i*] is the error of the number of γ-ray events in the i^{it} A_4 bin.
- *nperr*[*i*] is the error of the number of background events in the i^{it} A_4 bin.
- *ngerr*[1] is the error of the number of γ-ray events in the first A_4 bin.
- *nperr*[1] is the error of the number of background events in the first A_4 bin.
- Definitions of *weight*[*i*], *ngamma*[*i*], *nproton*[*i*], *ngamma*[1], and *nproton*[1] are the same as equation 4.3.

4.3.3 Monte Carlo A_4 Weights

Using the method discussed in section 4.3.2 the A_4 weighs for every epoch using Monte Carlo γ-rays and background events are calculated. For a high A_4 cut, the number of background events that pass the cut decreases rapidly. For example, there are only 7 Monte Carlo cosmic-ray background events with $A_4 \geq 12.0$ for epoch 7. To get enough statistics I used different A_4 bins for the data sets from table 4.3. Table 4.5 lists the A_4 bins used for the 7 Monte Carlo data sets (epoch 2 and 3 have the same simulated data set, and epoch 8 and 9 have the same simulated data set, so for 9 Milagro data sets there are only 7 Monte Carlo data sets). Table 4.6 lists the Monte Carlo A_4 weights for each epoch. Figure 4.1 to figure 4.7 compare the A_4 weighting results for each epoch using two different methods. In each figure Data (red points) represents the A_4 weights derived from Monte Carlo γ-ray events and measured background events. Monte Carlo (blue points) represents the A_4 weights derived from Monte Carlo γ-ray events and Monte Carlo background events. The big error bars for high A_4 bins are due to the lack of statistics for high energy Monte Carlo background events. From these figures we can see that the A_4 weighting results

Pre Outrigger. Epochs 1-3												
Bin Number(i)	1	2	3	4	5	6	7					
b_i^{min}	0.5	1.0	1.5	2.0	2.5	3.0	3.5					
b_i^{max}	1.0	1.5	2.0	2.5	3.0	3.5	∞					
Post Outrigger. Epochs 4												
Bin Number(i)	1	2	3	4	5	6						
b_i^{min}	1	2	3	4	5	6						
b_i^{max}	2	3	4	5	6	∞						
Post Outrigger. Epoch 5												
Bin Number(i)	1	2	3	4	5	6	7	8	9			
b_i^{min}	1	2	3	4	5	6	7	8	9			
b_i^{max}	2	3	4	5	6	7	8	9	∞			
Post Outrigger. Epoch 6-7												
Bin Number(i)	1	2	3	4	5	6	7	8	9	10		
b_i^{min}	1	2	3	4	5	6	7	8	9	10		
b_i^{max}	2	3	4	5	6	7	8	9	10	∞		
Post Outrigger. Epochs 8-9												
Bin Number(i)	1	2	3	4	5	6	7	8	9	10	11	12
b_i^{min}	1	2	3	4	5	6	7	8	9	10	11	12
b_i^{max}	2	3	4	5	6	7	8	9	10	11	12	∞

Table 4.5: Monte Carlo A_4 Bins. $b_x i^{min}$ and b_i^{max} represent the lower and upper edges of the A_4 bin respectively.

for these two methods are consistent. It also shows that the Milagro Monte Carlo simulations of Extensive Air Showers and detector response are robust.

4.3.4 The A_4 Weights We Choose and Results on the Crab Nebula

Since the Monte Carlo backgrounds do not have enough statistics, I used the A_4 weights derived from Monte Carlo γ-ray events and measured backgrounds for analysis for the rest of this thesis. To test A_4 weighted analysis technique, this technique was applied to the PSF smoothed data set with A_4 γ-hadron cut greater than 1 from July 19, 2000 to October 31, 2008 with and without A_4 weights given in table 4.4. Figure 4.8 shows the map of statistical significance around the Crab Nebula without the A_4 weights applied. The significance at the location of the Crab (RA=83.6°,

	Monte Carlo A_4 Weights						
Bin N<u>o</u>	E1	E2&E3	E4	E5	E6	E7	E8&E9
1	1.00 ± 0.00	1.00 ± 0.00	1.00 ± 0.00	1.00 ± 0.00	1.00 ± 0.00	1.00 ± 0.00	1.00 ± 0.00
2	1.80 ± 0.25	2.20 ± 0.38	2.57 ± 0.42	1.46 ± 0.18	2.30 ± 0.25	1.86 ± 0.20	2.00 ± 0.21
3	3.70 ± 0.64	4.06 ± 1.08	7.55 ± 2.01	3.69 ± 0.66	3.65 ± 0.54	3.15 ± 0.46	3.17 ± 0.42
4	6.78 ± 1.99	12.57 ± 3.75	10.84 ± 4.25	5.59 ± 1.22	5.67 ± 1.06	3.71 ± 0.65	3.62 ± 0.57
5	11.20 ± 3.94	12.03 ± 4.30	18.00 ± 10.76	8.33 ± 2.41	6.66 ± 1.70	8.93 ± 2.13	7.07 ± 1.49
6	40.03 ± 23.89	48.60 ± 33.19	20.60 ± 10.50	14.19 ± 8.37	6.67 ± 3.02	12.19 ± 4.06	8.02 ± 2.24
7	45.72 ± 24.42	72.25 ± 47.04		11.53 ± 6.91	14.03 ± 5.72	15.83 ± 6.03	18.11 ± 8.12
8				26.99 ± 17.14	9.86 ± 4.09	36.74 ± 29.02	14.19 ± 7.02
9				44.48 ± 20.81	28.06 ± 17.07	21.88 ± 12.63	17.17 ± 10.06
10					162.07 ± 89.99	47.03 ± 20.30	12.08 ± 5.66
11							49.26 ± 38.74
12							33.13 ± 14.22

Table 4.6: Monte Carlo A_4 γ-hadron weights for the different epochs. In each epoch, the weights have been normalized to that of the first A_4 bin.

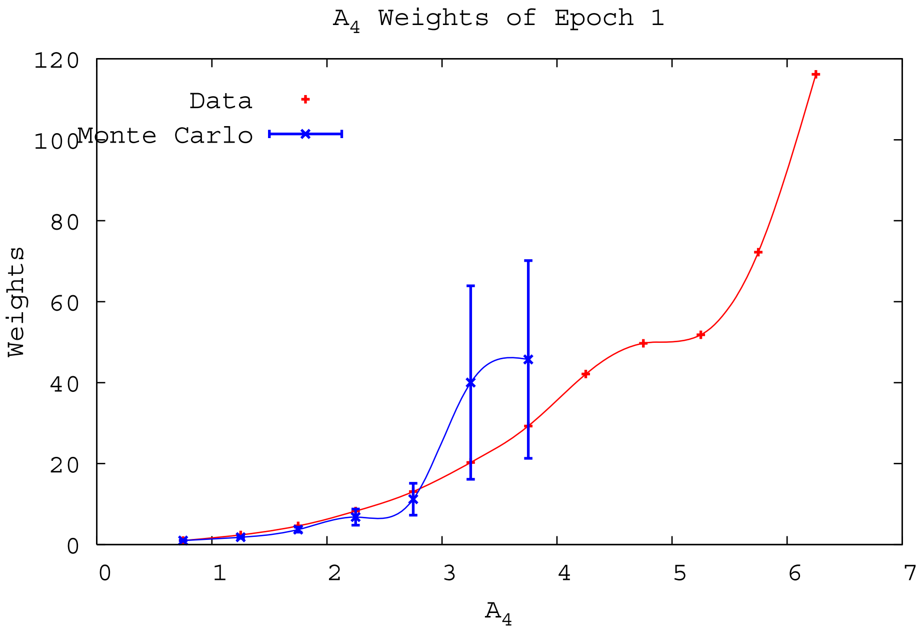

Figure 4.1: Comparison of A_4 weights using Monte Carlo backgrounds and measured backgrounds for epoch 1.

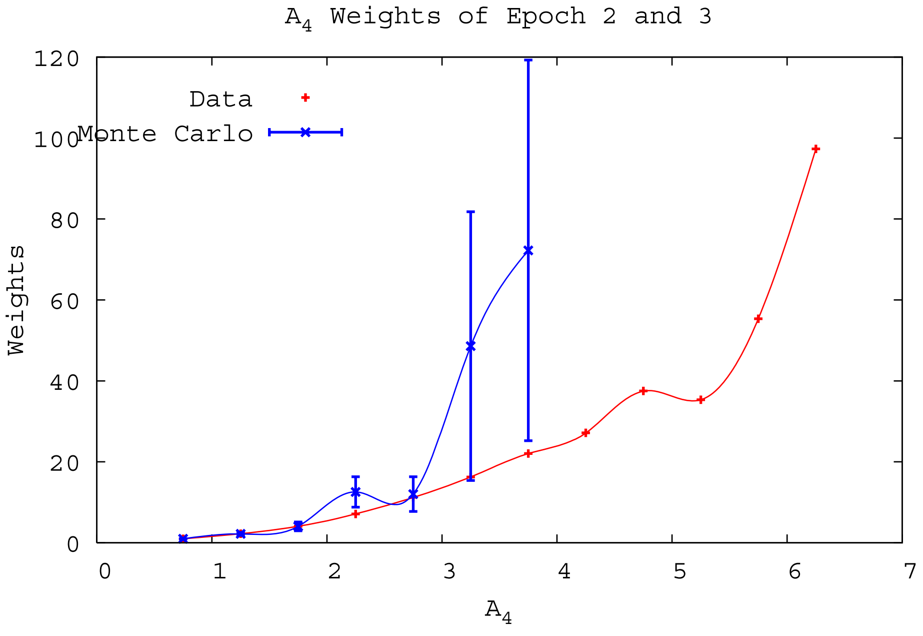

Figure 4.2: Comparison of A_4 weights using Monte Carlo backgrounds and measured backgrounds for epoch 2 & 3.

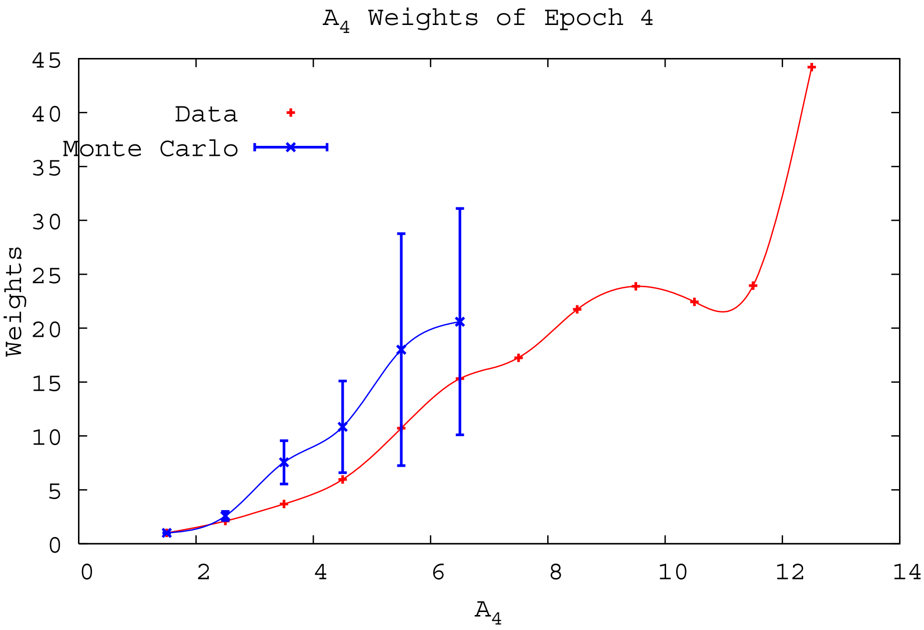

Figure 4.3: Comparison of A_4 weights using Monte Carlo backgrounds and measured backgrounds for epoch 4.

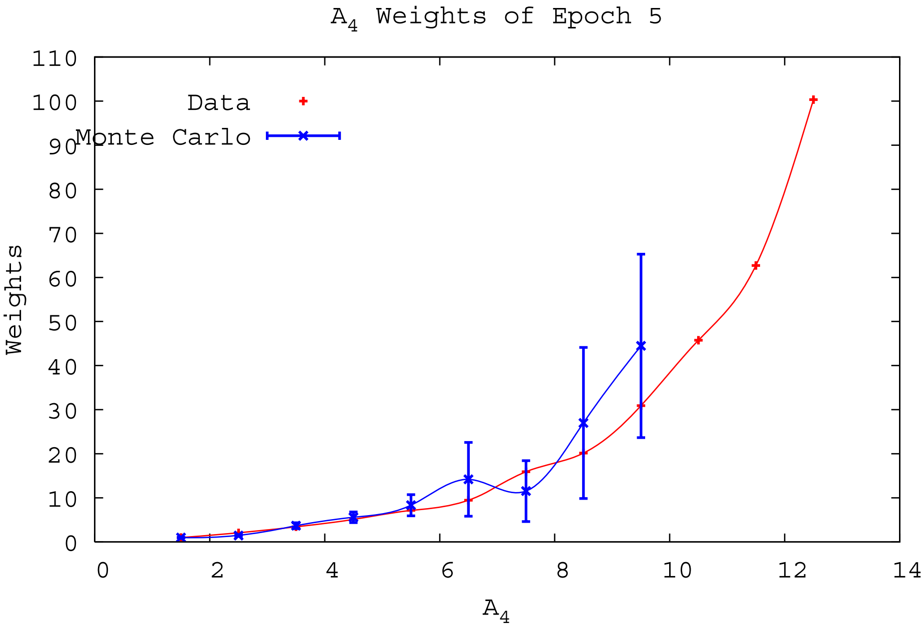

Figure 4.4: Comparison of A_4 weights using Monte Carlo backgrounds and measured backgrounds for epoch 5.

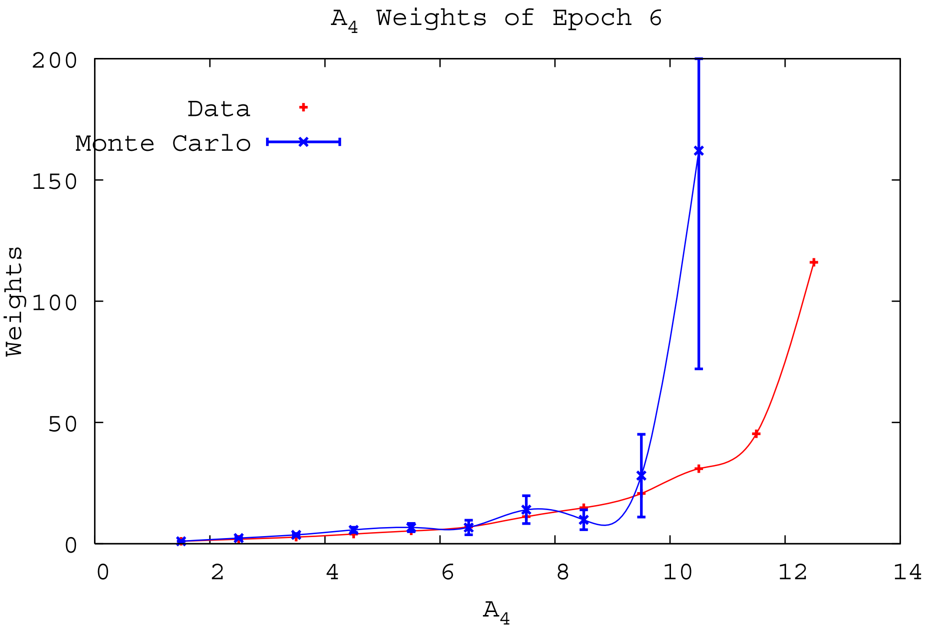

Figure 4.5: Comparison of A_4 weights using Monte Carlo backgrounds and measured backgrounds for epoch 6.

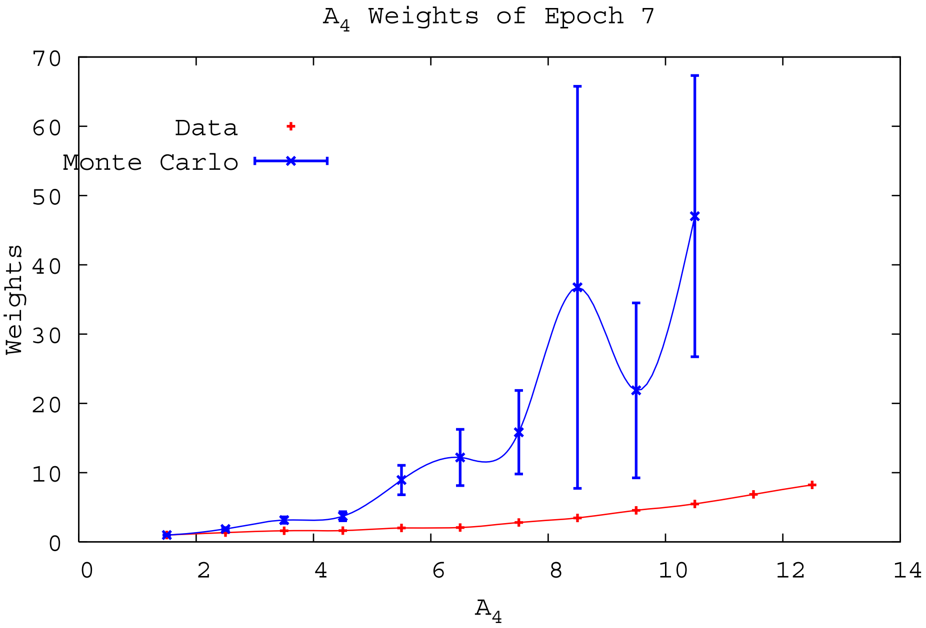

Figure 4.6: Comparison of A_4 weights using Monte Carlo backgrounds and measured backgrounds for epoch 7.

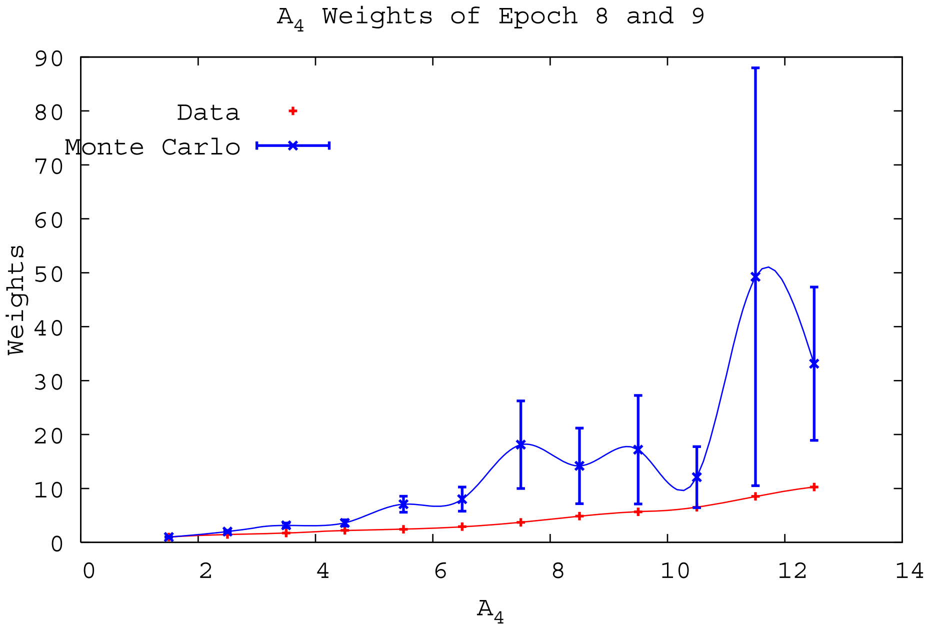

Figure 4.7: Comparison of A_4 weights using Monte Carlo backgrounds and measured backgrounds for epoch 8 & 9.

DEC=22.0°) is 11.93 σ. Figure 4.9 shows the maps of statistical significance around the Crab Nebula with the A_4 weighted analysis applied. The significance at the location of the Crab is 17.56 σ. An increase by 47% over the significance achieved without the A_4 weighted analysis.

4.4 Median Energy for the Weighted Analysis Technique

The weighted analysis technique assigns higher weights for events with higher values of X2 or A_4 and since events with higher values of X2 or A4 have higher median energies, it is expected that the median energy for gamma-ray events using weighted analysis will be higher than the one for triggered events. Tables 4.7 and 4.8 list the median energies for different power law spectra and different declinations for X2 unweighted

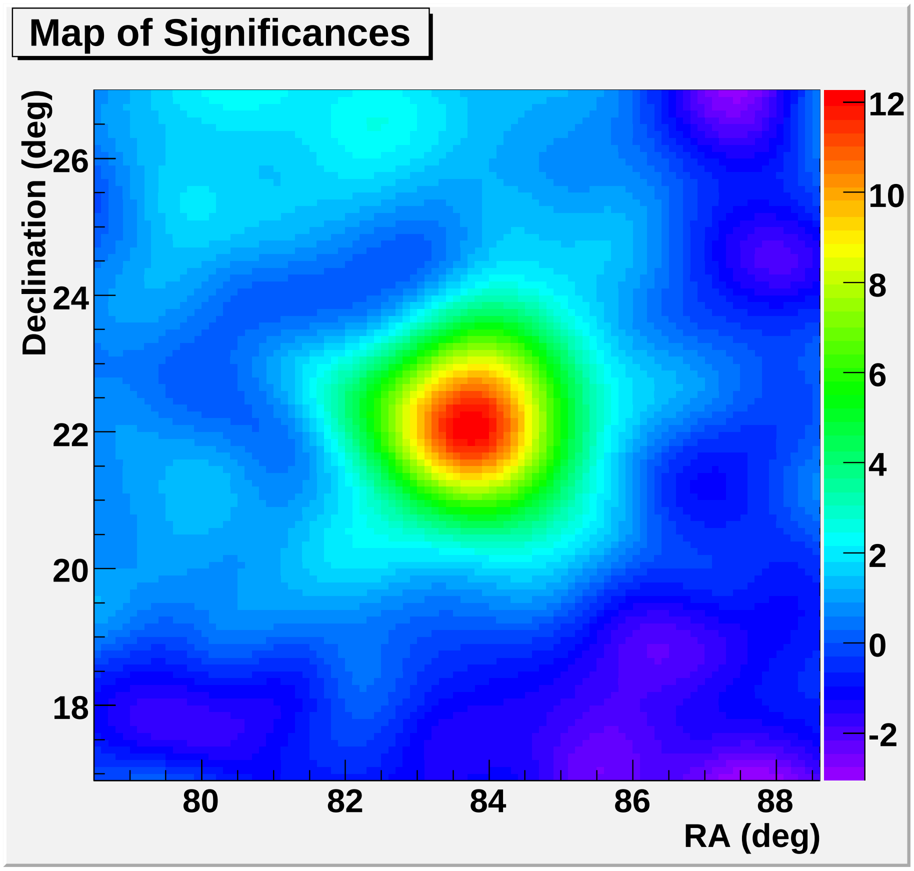

Figure 4.8: Map of the statistical significance around the Crab Nebula without the A_4 weighting analysis method applied.

analysis and A_4 weighted analysis respectively.[2] Three different declinations, 10°, 35°, and 60°, are calculated. Figure 4.10 and figure 4.11 show the median energies versus spectral index. Changing the spectral index of the simulated γ-ray events from $E^{-1.7}$ to $E^{-2.9}$ changes the median energies from ~ 64.9 TeV to ~ 9.8 TeV using A_4 weighted analysis for a declination of 35°.

---

[2] The reasons that unweighted not weighted $X2$ analysis is used in Milagro analysis and the rest of this thesis are because the $X2$ weighted analysis will not improve the significance as much as A_4 weighted analysis and also we want to keep more low energy γ-ray events.

	Median Energy (TeV)		
α	$\delta = 10°$	$\delta = 35°$	$\delta = 60°$
-1.7	38.4	22.0	35.0
-1.9	25.3	14.7	24.0
-2.1	17.7	9.8	16.8
-2.3	12.4	6.7	11.4
-2.5	8.4	4.5	7.7
-2.7	5.7	3.0	5.3
-2.9	3.6	2.0	3.2

Table 4.7: The median energies for the different spectra and 3 different declinations for non-weighted X2 analysis

	Median Energy (TeV)		
α	$\delta = 10°$	$\delta = 35°$	$\delta = 60°$
-1.7	70.6	51.6	66.6
-1.9	58.0	40.2	53.8
-2.1	47.0	32.3	42.2
-2.3	36.8	25.1	33.8
-2.5	27.3	18.8	26.5
-2.7	20.7	14.1	20.2
-2.9	15.7	10.0	15.4

Table 4.8: The median energies for the different spectra and 3 different declinations for weighted A_4 analysis

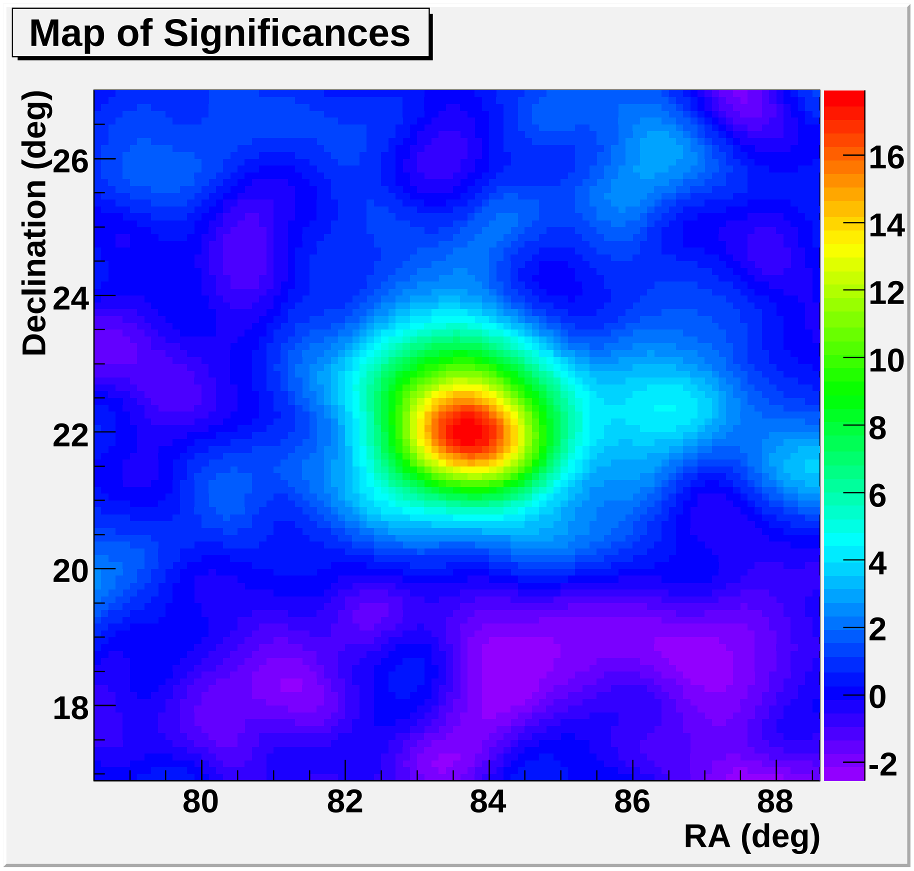

Figure 4.9: Map of the statistical significance around the Crab Nebula with the A_4 weighting analysis method applied.

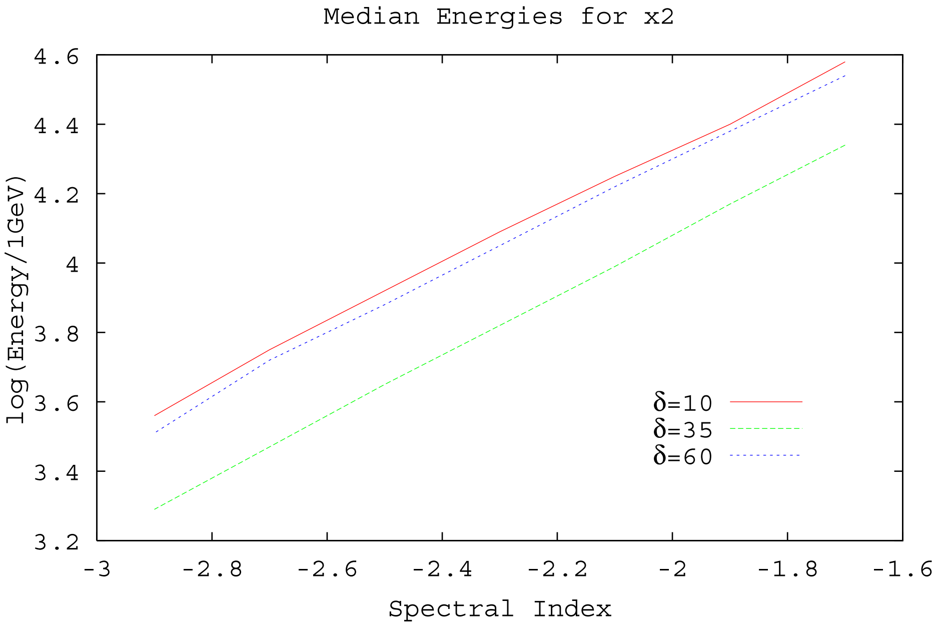

Figure 4.10: Median energies for different spectral indices and declinations for non-weighted x2 analysis.

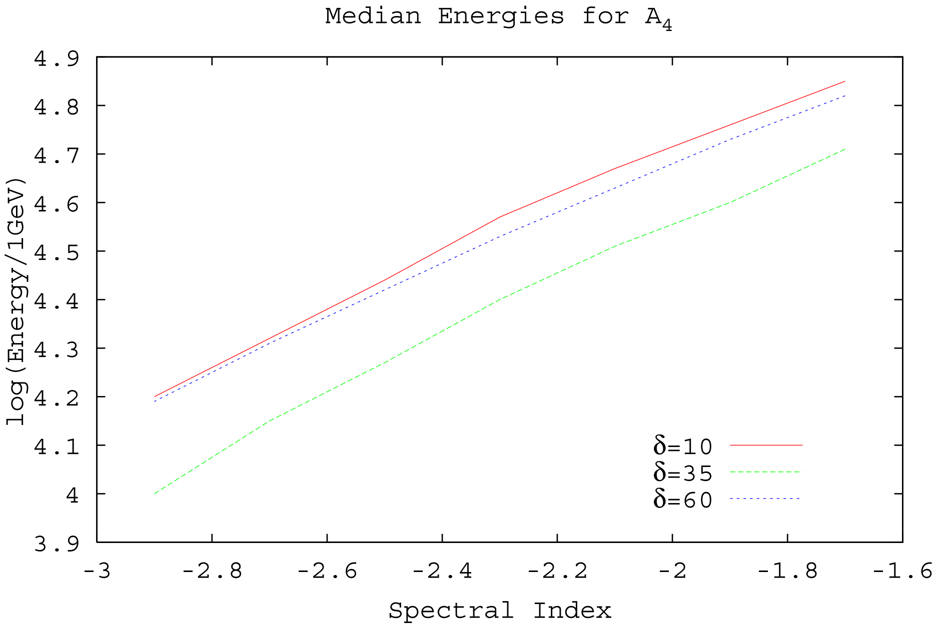

Figure 4.11: Median energies for different spectral indices and declinations for weighted A_4 analysis.

Chapter 5

Searching TeV Sources: Strategy and Simulation

5.1 EGRET Sources and Search Area Configuration

In the third catalog of high-energy γ-ray sources detected by the EGRET telescope on the *Compton Gamma Ray Observatory*, there are 271 sources (E $>$ 100 MeV) that include the single 1991 solar flare, the Large Magellanic Cloud, five pulsars, one probable radio galaxy detection (Cen A), 66 high-confidence identifications of blazars (BL Lac objects, flat-spectrum radio quasars, or unidentified flat-spectrum radio sources), 27 lower confidence potential blazars and 170 not yet identified sources [40]. 129 EGRET are in the Milagro field of view, which is RA $\in [0^\circ, 360^\circ)$ and DEC $\in [-5^\circ, 70^\circ]$. The point-spread function (PSF) of EGRET is $\sim 5^\circ$ at 100 MeV, which is much bigger than the Milagro's PSF[1]. In the third EGRET catalog the 95% confidence level contour has been chosen as representative of the source uncertainties. The error radius quoted in the catalog is the angular radius of a circular cone (rather

---

[1] Milagro PSF is about 0.90° for data without outriggers and 0.35° for data with outriggers.

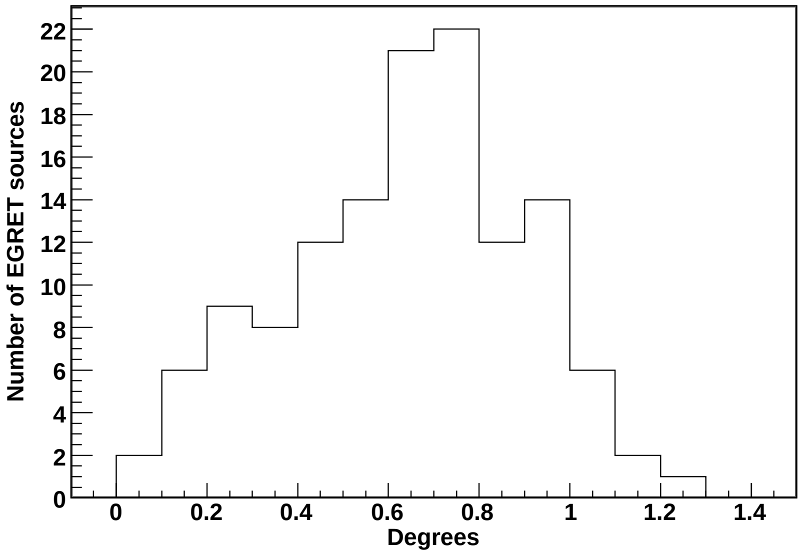

Figure 5.1: Distribution of position errors of 129 EGRET sources in the Milagro field of view

than elliptical, as in 2EG[41] and 2EGS[42] catalogues) which contains the same solid angle as the 95% contour. Figure 5.1 shows the distribution of position errors of the 129 EGRET sources in the Milagro field of view.

The smallest position error is 0.048° (Crab), and the biggest is 1.24°. The average position error for the all 129 EGRET sources is 0.64°. When using Milagro to analysis EGRET data one of the parameters which had to be defined was the area of the sky which had to be searched since the EGRET source positions are generally not the local maximum on the Milagro all sky significance map. Using a single bin on the celestial sphere to search for an EGRET source may not be sufficient and a search area needs to be defined. On the other hand, using a collection of bins to search the sources means the number of trials (which will be discussed in the next section) have to be considered in determining a posttrial significance. So the optimal size of the search area which will give the maximum posttrial significance of the EGRET sources has to be determined by the Monte Carlo simulation.

5.2 What Are Trials?

Using several bins to search an extended area of the sky complicates the determination of the significance of an excess. A famous Chinese idiom *da hai lao zhen*, in English means looking for a needle in a sea, is used to express a situation in which very small possibility generally can not happen. But if one searches enough seas in the world it is very possible to find a needle in some sea, and would think that to find a needle in a sea was not as hard as thought!

The effect on a significance measure of using several bins to a search for a source can be understood by considering the simple example below. A teacher wants to find out at least one student whose birthday is Jan 1^{st} in a school. Assume all students in this school were born in a non-leap year, then the probability that one student's birthday is Jan 1^{st} is 1/365, that is

$$p_0 = \frac{1}{365} \tag{5.1}$$

The probability is quite small and it is not easy to find one if the teacher only checks a few students. Assume he checks N students, then the probability for finding at least one student's birthday is Jan 1^{st} is,

$$P_N = 1 - (1 - p_0)^N \tag{5.2}$$

Table 5.1 lists the number of students and the corresponding probability to find at least one student's birthday is Jan 1^{st}.

N	1	2	3	4	5	...	298	299	300
P_N	0.00274	0.00547	0.00820	0.0109	0.0136	...	0.558	0.560	0.561

Table 5.1: The number of students and the probability of at least one student's birthday is Jan 1^{st}.

Although the probability is small when N is small, the chance to find at least one student with birthday is Jan 1^{th} is more than 56% when N equals 300!

In an analysis using several unsmoothed bins, the number of bins N can be thought of as analogous to the number of students, the probability for detecting an excess of certain significance in a bin as p_0, and the probability for detecting an excess at least as significant as this in at least one bin when N bins are searched , as P_N. N is called the number of *trials*, p_0 is called the *pretrial* probability, and P_N is called the *posttrial* probability.

5.3 A Method of Estimating Trials by Simulations

When using bin smoothed or PSF smoothed methods to search the EGRET sources, calculating the posttrial probability is not as simple as using equation 5.2, since the bins in the search area are correlated. For example, the Milagro data was binned with 0.1° × 0.1°. If the search area is a circle with 1° in radius, then the total number of bins in this area is roughly 314. But the total number of trials is obviously less than 314 because the bins are non-independent. The number of trials can be derived from the Monte Carlo simulation discussed below.

10^8 sky maps with RA from -2.5° to 2.5° and DEC from -2.5° and 2.5°[2] with 0.1° × 0.1° grid were simulated. Signals and backgrounds are populated on each sky map with the same fixed expected number (50,000). Each of the maps are bin smoothed by 1.5°[3]. The search area was 1° in radius around the center of the map and the maximum significance was saved. The equation used to calculate the trials for n σ sources is:

$$\frac{N_m}{N_t} = 1 - (1 - P_n)^{N_{trials}} \tag{5.3}$$

---

[2] The reason why only simulate RA$\in [-2.5°, 2.5°]$ and DEC$\in [-2.5°, 2.5°]$ is because 1) The EGRET source position errors are between 0° and 1.24°, the declination in the search area does not change much. 2) Increase the size of the simulated maps will dramatically increase the time on map smoothing and will not change the simulation results.

[3] The simulation method is similar to PSF smoothed method. Bins as far as 3.5 σ of the PSF are smoothed. See 3.4

where

- N_m is the number of maps with the maximum significance greater than n σ in the search area.

- N_t is the total number of maps (1 billion).

- P_n is the probability greater than n σ (e.g. P_3=0.001349).

- N_{trials} is the number of trials.

From equation 5.3,

$$N_{trials} = \frac{ln(1 - \frac{N_m}{N_t})}{ln(1 - P_n)} \tag{5.4}$$

The error of the number of trials can be calculated from the equation above. In this equation only N_m is a variable, so the error of N_{trials} is

$$\begin{aligned} \delta N_{trials} &= |\frac{dN_{trials}}{dN_m}| \times \delta N_m & (5.5) \\ &= (\frac{1}{N_m - N_t}) \times \frac{1}{ln(1 - P_n)} \times \delta N_m & (5.6) \end{aligned}$$

Since $N_m \gg 1$, $\delta N_m = \sqrt{N_m}$. Then,

$$\delta N_{trials} = \frac{\sqrt{N_m}}{N_m - N_t} \times \frac{1}{ln(1 - P_n)} \tag{5.7}$$

For example, from the results of the simulation in 1 billion maps there were 6,133,710 maps with the maximum significance greater than 3 σ in the search area. Plug the numbers in equation 5.4 and 5.7 the number of trials for 3 σ sources is 46.86 ± 0.02 (much less than 314 which is roughly the total number of bins in the search area). Similarly we can get the trials for other significance sources.

Four different situations were simulated. The bin smoothed sizes were 1.5° and 2.1°, and the search areas were 0.5° and 1.0° in radius at the center of the maps.

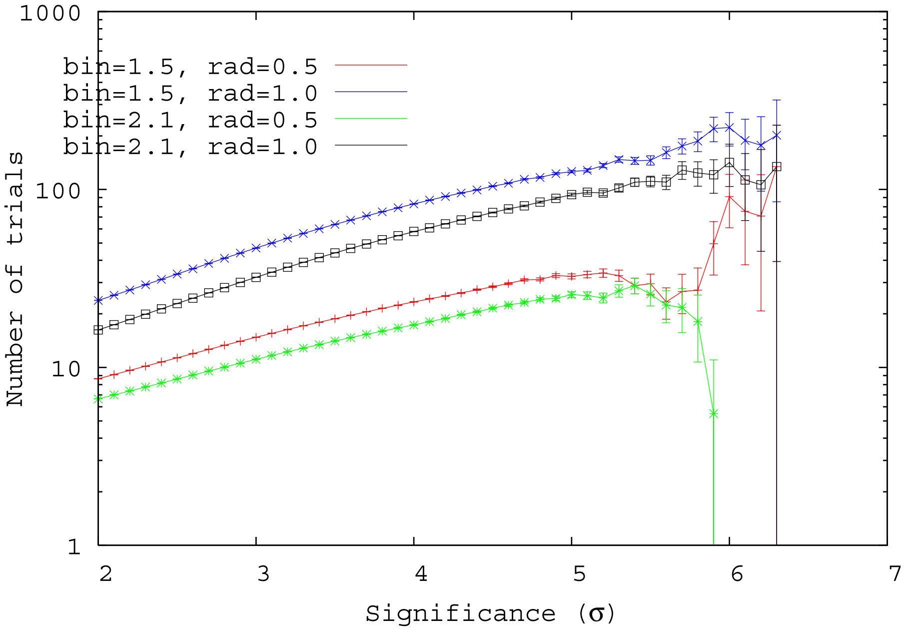

Figure 5.2: Number of trials as a function of significance for different smoothed bin sizes and search areas.

Figure 5.2 shows the results of the simulation. From the results we can see that the number of trials increases with the significance. Above 5 σ there are not enough statistics. In order to get the trials for any significant source, the plot can be fitted between 2σ and 5σ and extrapolated to high significance regions.

5.4 Simulation of Analysis Technique to Study EGRET Sources

More than one method can be used to study the EGRET sources using Milagro data. For either PSF smoothed or bin smoothed method, the search area can be 0.5°, 1.0°, or 1.5° in radius around the sources. The bigger the search area is, the more likely that a higher pretrial Li-Ma significance in certain $0.1^\circ \times 0.1^\circ$ bin can be found. However, as noted in the previous section, using more bins means that a greater number of trials will have to be considered in determining a posttrial significance. If the search area is too large it will increase the trials considerably and result in a smaller posttrial significance compared to that resulting from a search with smaller search area having less trials. Simulations have been done to study the optimum searching strategy.

Assume an EGRET source's position error is r_0, and the corresponding Gaussian parameter is σ_s, we have

$$0.95 = \frac{1}{\sigma_s^2} \int_0^{r_0} r e^{-\frac{r^2}{2\sigma_s^2}} dr \tag{5.8}$$

Solving the equation above can get

$$\sigma_s = \frac{r_0}{\sqrt{-2ln(0.05)}} = \frac{r_0}{2.45} \tag{5.9}$$

When r_0 is 0.5, $\sigma_s = 0.5/2.45 \approx 0.2$, and when r_0 is 1.24, $\sigma_s = 1.24/2.45 \approx 0.5$. The description of the simulation is below.

Step 1: Using the method in the previous section to simulate the number of trials versus source's significance for 3 different search areas with 0.5°, 1.0° and 1.5° in radius around the center of the simulated sky. The simulated sky is from -10° to 10° in RA and DEC with 0.1° × 0.1° in grid. Sigma used in PSF smoothed the maps is 0.73 and the bin size used in bin smoothed maps is 2.1°.

Step 2: Put a source in each simulated sky map. The position of each signal event is based on two parameters. The first is σ_s of the source and the second is the Milagro angular resolution which is 0.73° in the simulation. Assume the total signal events of a source is $NSource$ and the total background events is Bkg. Then from Li-Ma equation[4] 3.3 the significance in each 0.1° × 0.1° bin is,

$$\sigma = \frac{N_{on} - N_{off}}{\sqrt{(1+\alpha)N_{off}}} = \frac{NSource}{\sqrt{2Bkg}} \tag{5.10}$$

---

[4] For each 0.1° × 0.1° bin N_{on} (number of signal plus background events) and N_{off}(number of background events) were simulated respectively. α equals 1 in this case.

Radius	a (PSF)	b (PSF)	c (PSF)	a (bin)	b (bin)	c (bin)
0.5°	0.962	0.364	0.839	1.892	0.552	0.992
1.0°	1.622	0.507	1.678	3.944	0.681	1.317
1.5°	2.502	0.570	2.896	6.059	0.761	3.375

Table 5.2: Fitting results of the trials verse significance for PSF and bin smoothed maps for different search areas.

this is,

$$NSource = \sigma\sqrt{2Bkg} \tag{5.11}$$

If the significance of a source is 4.0, and the expected average number of background events in each 0.1° × 0.1° bin is 50,000, then the total simulated signal events of the source is $4.0 \times \sqrt{2 \times 50000 \times 21 \times 21} \approx 26563$. Three situations were simulated. The first was the source's position error was 0°. That meant $\sigma_S = 0$. The second was $\sigma_S = 0.2°$ which corresponded to a typical EGRET source's position error equals 0.5°. And the third was $\sigma_S = 0.5°$ which corresponded to a EGRET source's position error is 1.24°.

Figure 5.3 shows the number of trials for PSF and bin smoothed maps with search radius equals 1.0°. For the high significant region there are not enough statistics and the trials can be gotten from fitting the low significance region and extrapolating to the high significance region. The fitting equation is,

$$f(x) = a \cdot e^{b \cdot x} + c \tag{5.12}$$

The fitting results are listed in table 5.2

Next apply the results in table 5.2 in step 2. One million maps were simulated with sources at the center of the simulated sky maps, and σ_S equals 0.2 or 0.5. A source of a fixed flux was added to the background. The flux was chosen to be near the detection threshold. For each map the maximum pretrial significances in 4 search areas, circles with radius equal 0 (only look at the center of the map), 0.5°, 1.0° and

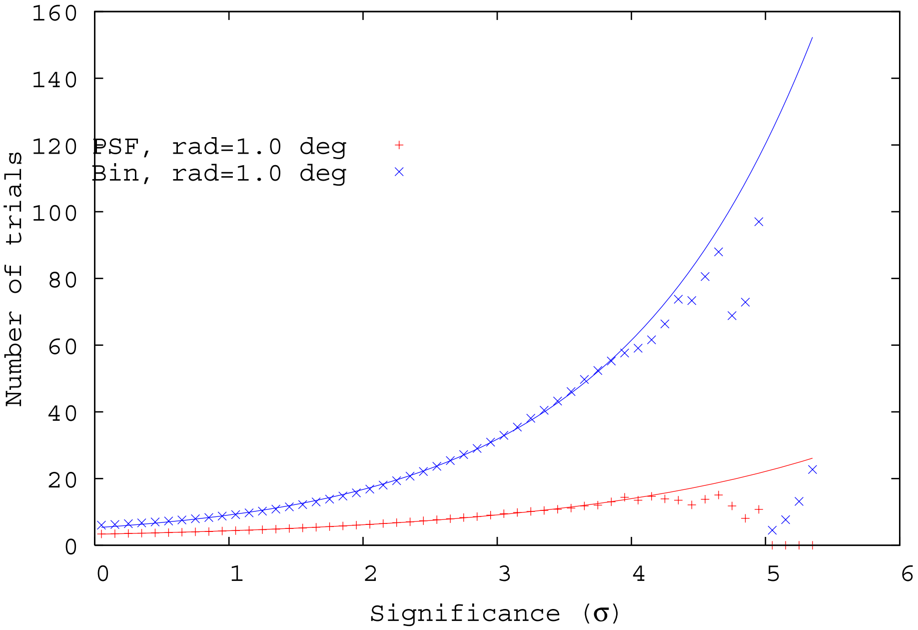

Figure 5.3: The number of trials verse significance for PSF and bin smoothed maps when search radius equals 1.0°.

1.5° were calculated. The posttrial significance was determined by the number of trials calculated from the fitting results in table 5.2. Figure 5.4 shows the distributions of the maximum posttrial significance for PSF and bin smoothed maps when σ_S equals 0.2° and the radius of the search area equals 1.0°. Similar figures for the other σ_S and search areas are shown in Appendix A. The average maximum posttrial significance for all situations are listed in table 5.3.

From table 5.3 we can draw the conclusion that PSF smoothing returns higher significance than binned smoothing. And for PSF smoothing analysis, for the three different EGRET position errors used in the simulation, only looking at an EGRET source positions (i.e radius = 0° in Table 5.3) will give the average higher posttrial significance than searching around the source. For bin smoothed analysis a searching radius equals 0.5° will give the highest average maximum posttrial significance for most EGRET sources (except for the sources with high position errors. For these

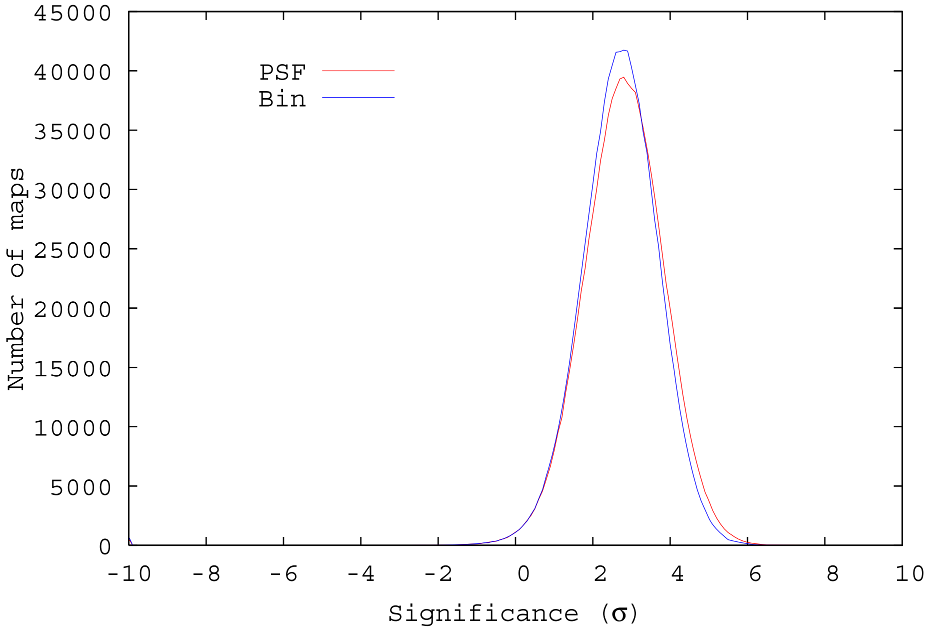

Figure 5.4: Distributions of the maximum posttrial significance for PSF and bin smoothed maps when σ_s equals 0.2° and the radius of the search area equals 1.0°.

	$\sigma_s = 0°$				$\sigma_s = 0.2°$				$\sigma_s = 0.5°$			
Radius	0°	0.5°	1.0°	1.5°	0°	0.5°	1.0°	1.5°	0°	0.5°	1.0°	1.5°
PSF	3.19	3.06	2.80	2.57	3.07	3.03	2.79	2.57	2.56	2.75	2.72	2.56
bin	2.83	2.91	2.72	2.48	2.73	2.85	2.70	2.48	2.27	2.48	2.56	2.44

Table 5.3: Average maximum posttrial significance for different σ_s and different search areas.

sources radius of the search area equals 1.0° will give higher posttrial significance).

5.5 Trials for the Galactic Plane

A survey of the entire northern hemisphere sky for sources of TeV gamma rays has been performed using the Milagro Gamma-Ray Observatory [38]. In 2007 Milagro reported on observations of sources at the energy of $\sim$ 20 TeV and in the region of Galactic longitude $l \in [30°, 220°]$ and latitude $b \in [-10°, 10°]$ [39]. In the Milagro data, four sources (including the Crab) are detected with posttrial significances

PSF σ	Trials Number	Posttrial Probability	Posttrial Significance (σ)
0.35	108700	2.23e-6	4.6
0.73	24500	5.04e-7	4.9
0.90	17040	3.50e-7	5.0

Table 5.4: Posttrial significance of MGRO J2031+41

greater than 4 σ, and four additional lower significance candidates are identified. This section describes my Monte Carlo simulation which account for the trials involved in searching this 3800 deg^2 region and lists the posttrial significance of the eight TeV γ-ray Galactic sources and candidates.

In the Milagro data the signal and background maps are smoothed with the point-spread function (PSF), which varies based on the number of hits in the events. For the early Milagro data the sigma of the PSF is about 0.90 and for the latest it is about 0.35. The sigma of PSF by fitting the whole Crab data is 0.73. The total maps in the simulation are 300,000 with a region of $190° \times 20°$. Using the same method discussed in section 5.3 the number of trials of the Galactic plane were simulated and figure 5.5, figure 5.6 and figure 5.7 show the results. The plots are fitted in the low significance regions and extrapolated to high significance regions since above 5 sigmas they are not enough statistics. The approximate functions of the number of trials for different PSF sigmas are below :

when $\sigma = 0.35$, N$_{trials}$=23000σ-50000
when $\sigma = 0.73$, N$_{trials}$=5000σ-10000
when $\sigma = 0.90$, N$_{trials}$=3600σ-7800

For example, TeV γ-ray source MGRO J2031+41 [39], the pretrial significance measured by Milagro is 6.6 σ. The posttrial significances based on the Monte Carlo simulation with 3 different Milagro PSF are listed in table 5.4.

It is hard to calculate the average sigma for the PSF smoothed map for the whole Milagro data set. Using the Milagro global averaged PSF for the Crab data, 0.73, is a pretty good approximation. The number of trials, the pretrial and posttrial

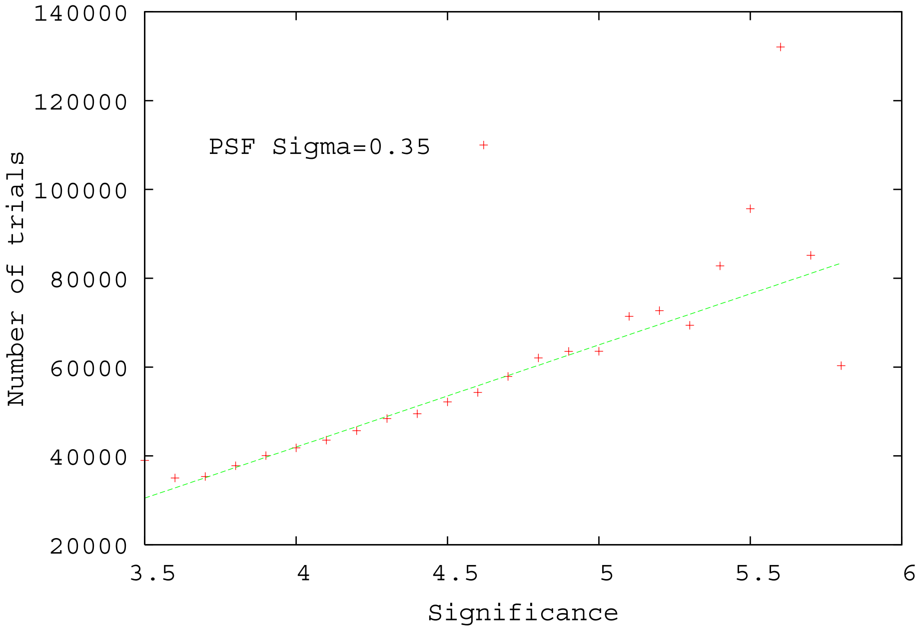

Figure 5.5: Number of trials of the Galactic plane as a function of significance for the PSF smoothed sigma equals 0.35.

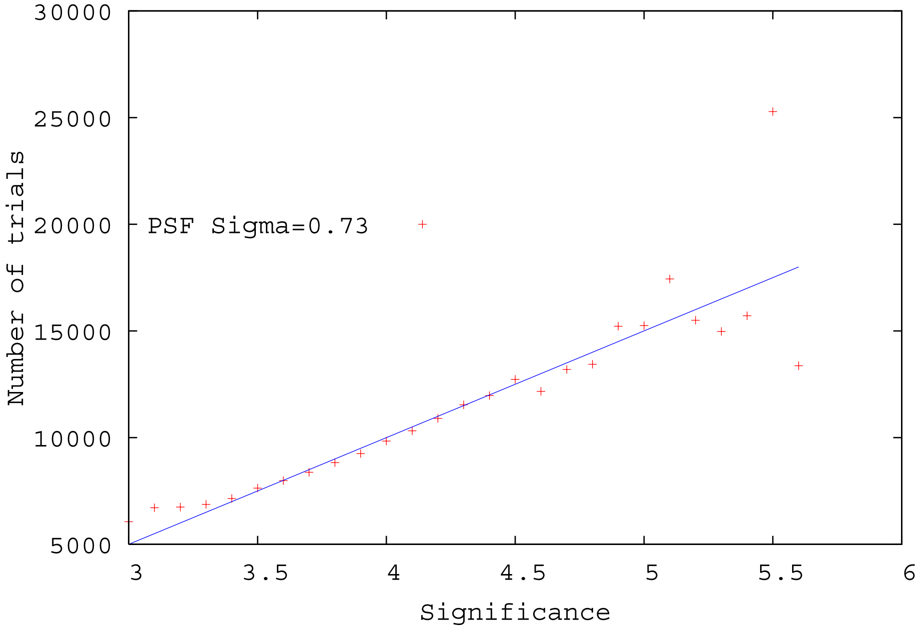

Figure 5.6: Number of trials of the Galactic plane as a function of significance for the PSF smoothed sigma equals 0.73.

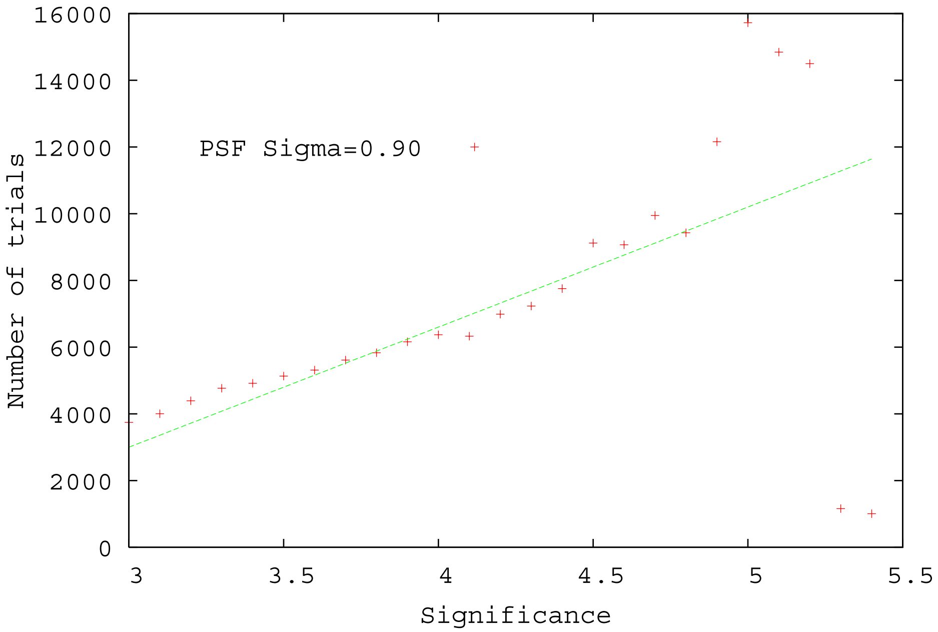

Figure 5.7: Number of trials of the Galactic plane as a function of significance for the PSF smoothed sigma equals 0.90.

significance for the eight Galactic sources and source candidates are listed in table 5.5.

Object	Pretrial Significance (σ)	Trials Number	Posttrial Significance (σ)
Crab	15.0	65000	14.3
MGRO J2019+37	10.4	42000	9.3
MGRO J1908+06	8.3	31500	7.0
MGRO J2031+41	6.6	23000	4.9
C1	5.8	19000	3.8
C2	5.1	15500	2.8
C3	5.1	15500	2.8
C4	5.0	15000	2.6

Table 5.5: Prosttrial significance of Galactic sources and source candidates. These results are also in Milagro's Galactic Plane paper[39].

Chapter 6

Survey of EGRET Sources

6.1 Introduction to EGRET, Whipple and Milagro Results

The third catalog of EGRET telescope includes 271 high-energy γ-ray sources (E $>$ 100 MeV) [40]. The Whipple observatory 10m γ-ray telescope surveyed the error boxes of EGRET unidentified sources in an attempt to find counterparts at energies of 350 GEV and above [48]. Twenty one unidentified sources detected by EGRET were included in Whipple's survey. Whipple did not find statistically significant signals in the EGRET error box in any of the 21 sources. In many cases, this implies that the γ-ray spectra of these sources steepen between 100 MeV and 350 GeV. Whipple derived their flux upper limits for these sources by assuming that the VHE emission is from a source with a spectral index similar to that of the Crab Nebula in the very high energy regime, i.e. $\alpha \approx -2.5$.

In this chapter, I present flux and flux upper limits for 129 EGRET sources that were in Milagro's field of view, using $X2$ and A_4 analyses techniques. The median energies for γ-ray detection from sources by Milagro are 7 TeV for non-weighted psf smoothed $X2$ ($>$ 2.5) analysis and 25 TeV for A_4 weighted analysis (see table 4.7 and table 4.8) for an assumed source spectral index of α=-2.3. This spectral index was chosen based on the average spectrum for galactic sources observed by HESS [50].

I present comparison of Milagro flux or upper limits versus the EGRET fluxes at 100 MeV, as well as plots for Milagro flux or upper limits versus EGRET flux extrapolation to 7 and 25 TeV.

Of the 21 EGRET unidentified sources surveyed by Whipple 18 were also in the Milagro field of view. Milagro results for these 18 sources using $X2$ and A_4 technique are compared with Whipple upper limits measurements at 350 GeV. Whipple upper limits at 350 GeV and Milagro upper limits at 7 and 25 TeV are compared with EGRET measurements extraploated to 25 TeV for these 18 sources.

6.2 Significances of EGRET Sources

From the simulation result in section 5.4 we know that for Milagro PSF smoothed analysis the best strategy to search for TeV emission from EGRET sources is to just look at the significance at EGRET source positions. This will give the highest posttrial significance. Figure 6.1 and figure 6.2 show the significance distributions of the 129 EGRET sources using non-weighted psf smoothed $X2$ and weighted psf smoothed A_4 analysis respectively. For $X2$ analysis, 15 EGRET sources' significances are greater than 2 σ, and 114 are less than 2 σ. For A_4 analysis 21 are greater than 2 σ, and 108 are less than 2 σ. The number of sources with greater than 2 σ by chance is about 3.

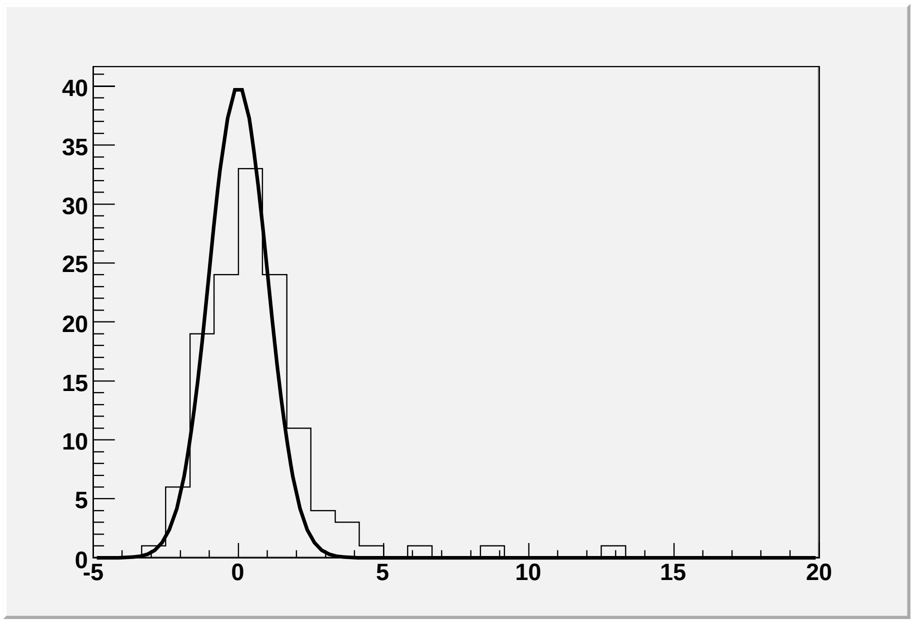

Figure 6.1: Distribution of the significance of 129 EGRET sources for Milagro $X2$ analysis.

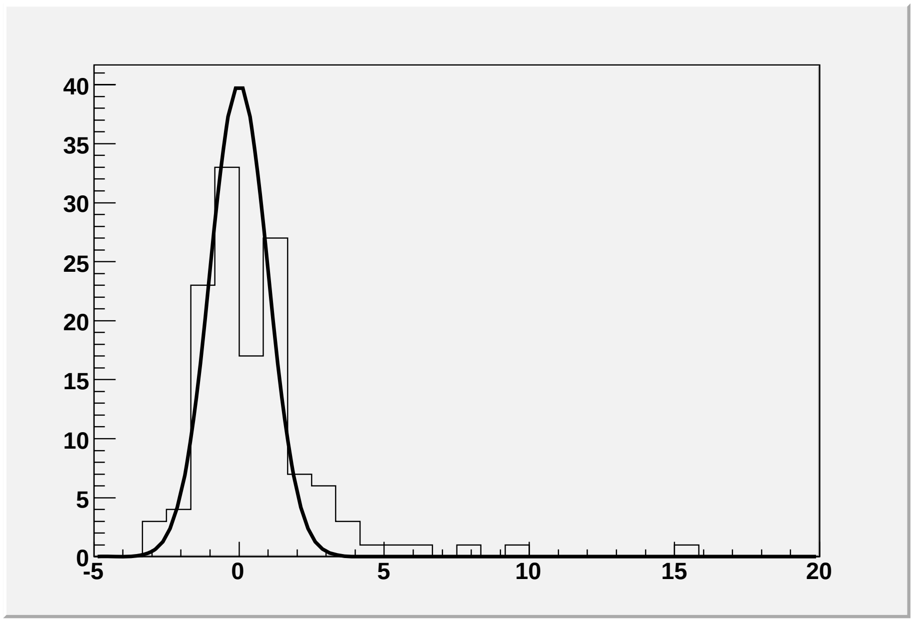

Figure 6.2: Distribution of the significance of 129 EGRET sources for Milagro A_4 analysis.

6.3 Flux Calculation

6.3.1 Flux in the Third EGRET Catalog and Whipple Flux Upper Limits

Typically the fluxes from VHE γ-ray sources have a power law spectrum. The differential γ-ray flux for a given source is defined as the number of photons from that source per unit area per unit energy per unit time. It is given by:

$$dN/dE = kE^{-\alpha} \tag{6.1}$$

where k is a constant which gives the photon flux from a source at a specific energy and α is the spectral index defining the shape of the energy spectrum. The function is simple to manipulate and is a good approximation to the emission expected from VHE γ-ray sources. Assume the flux above energy E_0 is F, then

$$\begin{aligned} F(\geq E_0) &= \int_{E_t}^{\infty} \frac{dN}{dE} dE & (6.2) \\ &= \int_{E_t}^{\infty} kE^{-\alpha} dE & (6.3) \\ &= \frac{k}{\alpha - 1} E_0^{-\alpha+1} & (6.4) \end{aligned}$$

From equations above if the flux is known then k is given by,

$$k = \frac{F(\alpha - 1)}{E_0^{-\alpha+1}} \tag{6.5}$$

In the 3EG catalog F is the flux above 100 MeV (E_0) in units $10^{-8}\mathrm{cm}^{-2}\mathrm{s}^{-1}$. After some calculation we can get the flux of EGRET sources above 100 MeV, extrapolated to 7 TeV and 25 TeV respectively,

$$E^2\frac{dN}{dE}(\geq 100MeV) = F(\alpha-1)1.602\cdot 10^{-12}\ ergs\cdot cm^{-2}\cdot s^{-1} \tag{6.6}$$

$$E^2\frac{dN}{dE}(\geq 7TeV) = F(\alpha-1)(7\cdot 10^{4})^{-\alpha+1}11\cdot 10^{-8}\ ergs\cdot cm^{-2}\cdot s^{-1} \tag{6.7}$$

$$E^2\frac{dN}{dE}(\geq 25TeV) = F(\alpha-1)(2.5\cdot 10^{5})^{-\alpha+1}40\cdot 10^{-8}\ ergs\cdot cm^{-2}\cdot s^{-1} \tag{6.8}$$

In these three equations above the units of F are taken out, so F is just the scalar number in the third EGRET catalog. For most of the EGRET sources, the 3EG catalog also lists the 1 σ statistical uncertainty in the flux F, the photon spectral index α and 1 σ error of the index. So the flux errors for the sources at 100 MeV can be extrapolated to 7 TeV and 25 TeV.

The Whipple observatory 10 m γ-ray telescope surveyed EGRET unidentified sources and derived upper limits on the intergral γ-ray flux above 350 GeV for 21 of them assuming the Crab Nebula spectral index ($\alpha \approx -2.5$) [48]. Eighteen of the 21 souces are also in the Milagro field of view. Similarly to the EGRET sources, the equations of flux upper limits above 350 GeV and extrapolation to 7 TeV and 25 TeV are below (using the Whipple fits at 350 GeV),

$$E^2\frac{dN}{dE}(\geq 350GeV) = F(\alpha-1)5.607\cdot 10^{-12}\ ergs\cdot cm^{-2}\cdot s^{-1} \tag{6.9}$$

$$E^2\frac{dN}{dE}(\geq 7TeV) = F(\alpha-1)20^{-\alpha+1}11\cdot 10^{-11}\ ergs\cdot cm^{-2}\cdot s^{-1} \tag{6.10}$$

$$E^2\frac{dN}{dE}(\geq 25TeV) = F(\alpha-1)71.4^{-\alpha+1}40\cdot 10^{-11}\ ergs\cdot cm^{-2}\cdot s^{-1} \tag{6.11}$$

6.3.2 Flux Calculation for A_4 Analysis

The procedure to calculate the flux from an EGRET source is similar to the flux calculation in Milagro's Galactic Plane paper [39, 43]. As discussed in Chapter 4 for Milagro analysis, although there are 9 different data epochs, there are only seven epochs for the Monte Carlo simulation. The epoch 2 & 3, and epoch 8 & 9 can be combined. The data are further divided into 12 A_4 bins. Weights are applied per bin based on how likely the events in that bin are actually γ-rays and not background events, and the data is recombined into a final weighted events map of the sky. Only Declinations $\delta \in [-2^\circ, 70^\circ]$ are used, as the fluctuations grow rapidly beyond these limits, especially for the low Declinations. Milagro's simulation program is run to determine the number of Monte Carlo γ-ray events per day as a function of Declination, $(N_\gamma/\mathrm{day})(\delta)$. These numbers were obtained assuming a spectral index -2.3 and a flux of 10 times of Crab at 1 TeV of 2.83×10^{-10} $\mathrm{TeV}^{-1}\mathrm{cm}^{-2}\mathrm{s}^{-1}$. This is done for all A_4 bins and in all seven epochs. The $(N_\gamma/\mathrm{day})(\delta)$ is multiplied by the A_4 weights for each bin and the days in each epoch (with a 0.9 factor to account for instrumental deadtime) and then summed to give a final total number of weighted events as a function of declination:

$$W(\delta) = \sum_{i=1}^{7} \sum_{j=1}^{12} N_\gamma^{ij}(\delta) \times wgt^{ij}(\gamma) \times N_{day}(i) \tag{6.12}$$

The first summation is over the number of epochs while the second summation is over the number of A_4 bins in each epoch, $N_\gamma^{ij}(\delta)$ is the number of gammas per day as a function of declination for the j'th A_4 bin in the i'th epoch. $wgt^{ij}(\gamma)$ is the gamma-hadron weight for the j'th A_4 bin in the i'th epoch, and $N_{day}(i)$ is the number of days in the i'th epoch.

This Declination dependent weighted number of events is used to remove the Declination dependence of the data excess map to give a map in units of Crab flux:

$$\phi_c = \frac{excess(\delta)}{W(\delta)} \tag{6.13}$$

where ϕ_c is the flux in units of the Crab flux, and $excess(\delta)$ is the excess as a function of Declination. To get the flux in units of $\text{TeV}^{-1}\text{cm}^{-2}\text{s}^{-1}$, a further normalization factor is needed:

$$\phi = \phi_c \times \frac{dN}{dE} \tag{6.14}$$

The median energy of the weighted A_4 analysis is 25 TeV. So to get the flux in units of $\text{TeV/cm}^{-2}\text{s}^{-1}$ another factor 25^2 need to be mutiplied at the right side of equation 6.14.

6.3.3 Flux Calculation for $X2$ Analysis

The flux calculation for $X2$ analysis is almost the same as for A_4 analysis. The only difference is that I used non-weighted $X2$ analysis. So equation 6.12 will become:

$$W(\delta) = \sum_{i=1}^{7} N_{\gamma}^{i}(\delta) \times N_{day}(i) \tag{6.15}$$

$N_{\gamma}^{i}(\delta)$ is the number of gammas per day as a function of declination for the whole i'th epoch, and $N_{day}(i)$ is the number of days in the i'th epoch. Since the median energy of the non-weighted $X2$ analysis is 7 TeV, to get the flux in units of $\text{TeV/cm}^{-2}\text{s}^{-1}$ another factor 7^2 need to be multiplied.

6.4 Flux Upper Limit

Figure 6.1 and figure 6.2 show that the significance for most of the EGRET sources are low ($< 2.0\sigma$) using either $X2$ or A_4 analysis. In this situation we cannot decide about whether the source exists or not. We can only say that the events in the source area is less than or comparable to the background statistical fluctuation. An upper limit on the source can be computed. This is the value that the source flux must have been less than, at some confidence level, in order for it have not been detected. In this chapter any upper limit will be quoted at the 95% confidence level.

The value of the flux upper limit is calculated following the method of Helene[44]. The number of events in Milagro is large, this method will be utilized under the assumption that he number of γ-ray events detected from a source follows a Gaussian distribution. This distribution is centered on the measured value for the excess of the source and has σ_{excess} where σ_{excess} is the statistical error on the measured excess. So after calculating the flux and the statistical error of the flux, the flux upper limit can be calculated from these two numbers. Details of the method to calculate the flux upper limit is in Appendix B.

6.5 Results

6.5.1 Put All Results Together

Table 6.1 to table 6.5 list the detailed results of 129 EGRET sources. Due to the limit space in these tables, the EGRET measurement extrapolations to 7 and 25 TeV with errors, and the Whipple upper limit extrapolations to 7 and 25 TeV with errors are not included in these tables. They can be derived from the equations in section 6.3.1. In these tables Name, Location (RA, Dec), Flux ($>$ 100MeV, in unit of 10^{-11}ergs cm^{-2} s^{-1}), and the spectral index are taken from the third EGRET catalog. Whipple U.L. ($>$ 350 GeV, in unit of 10^{-11}ergs cm^{-2} s^{-1}) is the upper limits of 18 unidentified EGRET sources measured by Whipple telescope. Flux and U.L. are the Milagro measured flux and upper limit of the 129 EGRET sources using non-weighted $X2$ (in unit of 10^{-12}ergs cm^{-2} s^{-1}) and weighted A$_4$ (in unit of 10^{-13}ergs cm^{-2} s^{-1}) analyses.

	Name	Location		Significance (σ)		Flux		U.L.		Flux	Spectral Index	Whippl
No.	(3EG)	RA	Dec	$X2$	A_4	$X2$	A_4	$X2$	A_4	(>100MeV)	(α)	(>350
1	J0010+7309	2.6	73.2	-0.4	0.9	-5.2 ± 7.7	7.5 ± 8.0	12.1	21.5	5.8 ± 1.0	1.85 ± 0.1	1.
2	J0118+0248	19.6	2.8	1.2	-0.9	7.0 ± 7.1	-7.9 ± 9.0	19.3	13.2	1.3 ± 0.9	2.63 ± 0.66	
3	J0204+1458	31.1	15.0	-1.3	1.0	-4.9 ± 4.0	6.7 ± 5.1	5.3	15.3	1.7 ± 0.7	2.23 ± 0.28	
4	J0215+1123	34.0	11.4	1.0	0.5	2.6 ± 4.6	3.9 ± 5.7	10.8	14.1	1.5 ± 0.9	2.03 ± 0.62	
5	J0222+4253	35.7	42.9	0.1	1.0	-0.9 ± 3.1	4.0 ± 4.0	5.4	10.9	3.0 ± 0.6	2.01 ± 0.14	
6	J0229+6151	37.3	61.9	0.2	0.1	-2.5 ± 3.9	0.2 ± 4.8	6.2	9.4	7.8 ± 1.7	2.29 ± 0.18	
7	J0237+1635	39.4	16.6	1.8	0.9	5.3 ± 3.9	3.8 ± 5.0	11.9	12.5	3.5 ± 0.7	1.85 ± 0.12	
8	J0239+2815	40.0	28.3	-1.1	-1.3	-2.1 ± 3.3	-5.2 ± 4.2	5.2	5.5	3.4 ± 0.8	2.53 ± 0.22	
9	J0241+6103	40.4	61.1	1.3	0.0	2.8 ± 3.9	3.5 ± 4.8	9.8	11.9	13.4 ± 1.4	2.21 ± 0.07	1.
10	J0245+1758	41.4	18.0	-0.9	-0.2	-4.8 ± 3.8	0.0 ± 4.9	5.0	9.6	2.3 ± 1.0	2.61 ± 0.44	
11	J0253-0345	43.5	-3.8	-0.1	0.2	-5.8 ± 11.7	-4.6 ± 13.2	19.5	23.1	0.0 ± 0.0		
12	J0323+5122	50.9	51.4	0.4	0.8	-0.2 ± 3.3	1.0 ± 4.3	6.4	9.0	2.1 ± 1.0	2.38 ± 0.41	
13	J0329+2149	52.4	21.8	-0.7	-0.4	-2.0 ± 3.6	-4.7 ± 4.7	5.9	6.7	1.9 ± 0.8	2.61 ± 0.33	
14	J0340-0201	55.0	-2.0	0.7	-1.3	10.2 ± 10.1	-3.3 ± 11.8	27.6	21.1	2.0 ± 0.8	1.84 ± 0.25	
15	J0348+3510	57.0	35.2	0.4	-0.9	3.0 ± 3.2	-6.1 ± 4.2	8.6	5.2	2.1 ± 0.7	2.16 ± 0.27	
16	J0404+0700	61.2	7.0	0.5	2.2	1.0 ± 5.3	15.5 ± 6.6	11.1	26.4	2.9 ± 0.9	2.65 ± 0.26	
17	J0407+1710	61.8	17.2	-2.9	-1.5	-7.8 ± 3.9	-11.6 ± 5.0	4.2	4.8	2.3 ± 0.9	2.93 ± 0.37	
18	J0416+3650	64.0	36.8	0.3	-0.9	1.0 ± 3.2	-1.8 ± 4.1	7.0	6.9	3.3 ± 0.9	2.59 ± 0.32	
19	J0422-0102	65.7	-1.0	0.6	1.7	3.4 ± 9.4	15.8 ± 10.9	20.7	34.1	3.8 ± 0.9	2.44 ± 0.19	
20	J0423+1707	65.9	17.1	-0.9	-1.0	-1.2 ± 3.9	-5.5 ± 5.0	6.9	6.8	3.6 ± 0.8	2.43 ± 0.21	5.
21	J0426+1333	66.7	13.6	0.1	-0.8	2.6 ± 4.3	-3.1 ± 5.5	10.2	8.9	2.6 ± 0.7	2.17 ± 0.25	
22	J0429+0337	67.4	3.6	3.0	1.3	13.5 ± 6.6	13.1 ± 8.4	24.4	27.1	3.9 ± 1.0	3.02 ± 0.27	
23	J0433+2908	68.4	29.1	-1.0	1.2	-3.5 ± 3.2	5.6 ± 4.3	4.3	12.9	3.2 ± 0.5	1.9 ± 0.1	1.
24	J0435+6137	68.9	61.6	-1.3	-0.1	-3.5 ± 4.0	-1.8 ± 4.9	5.8	8.4	3.7 ± 1.2	2.46 ± 0.35	
25	J0439+1555	69.8	15.9	1.7	1.2	4.3 ± 4.1	12.7 ± 5.2	11.3	21.3	1.0 ± 0.6	2.27 ± 0.44	
26	J0439+1105	69.8	11.1	0.6	-0.1	2.2 ± 4.5	4.0 ± 5.8	10.4	14.3	2.2 ± 0.7	2.44 ± 0.29	

Table 6.1: Fluxes and upper limits of 129 EGRET sources measured by Milagro.

	Name	Location		Significance (σ)		Flux		U.L.		Flux	Spectral Index	Whipp
No.	(3EG)	RA	Dec	$X2$	A_4	$X2$	A_4	$X2$	A_4	(>100MeV)	(α)	(>35
27	J0442-0033	70.6	-0.6	1.7	1.0	14.4 ± 9.6	16.6 ± 11.2	30.6	35.3	2.7 ± 0.7	2.37 ± 0.18	
28	J0450+1105	72.6	11.1	1.3	0.5	7.4 ± 4.5	4.3 ± 5.8	14.9	14.6	3.0 ± 0.6	2.27 ± 0.16	4
29	J0459+0544	74.9	5.8	-0.5	0.1	-3.5 ± 5.9	-11.7 ± 7.1	9.4	8.3	1.3 ± 0.6	2.36 ± 0.4	
30	J0459+3352	74.8	33.9	-1.2	-2.0	-1.5 ± 3.2	1.9 ± 4.3	5.4	9.8	3.3 ± 0.8	2.54 ± 0.24	
31	J0500+2529	75.1	25.5	0.1	1.3	-1.0 ± 3.3	5.8 ± 4.3	5.9	13.1	1.2 ± 0.6	2.52 ± 0.32	
32	J0500-0159	75.1	-2.0	2.2	0.5	17.9 ± 10.1	13.9 ± 11.9	34.6	34.2	2.6 ± 0.7	2.45 ± 0.27	
33	J0510+5545	77.6	55.8	-2.2	-1.9	-8.2 ± 3.5	-11.9 ± 4.4	3.4	3.8	4.1 ± 1.0	2.19 ± 0.2	
34	J0516+2320	79.1	23.4	0.5	-1.4	3.8 ± 3.6	-5.0 ± 4.8	9.9	6.6	45.2 ± 10.5	2.67 ± 0.33	
35	J0520+2556	80.1	25.8	2.7	1.3	11.0 ± 3.3	9.0 ± 4.4	16.5	16.2	4.6 ± 1.0	2.83 ± 0.24	
36	J0521+2147	80.4	21.8	0.4	1.1	2.2 ± 3.7	3.9 ± 4.9	8.8	12.4	4.9 ± 0.9	2.48 ± 0.15	
37	J0530+1323	82.7	13.4	-1.9	-1.9	-8.2 ± 4.4	-13.6 ± 5.6	4.8	5.2	21.9 ± 1.0	2.46 ± 0.04	
38	J0533+4751	83.3	47.9	-0.1	-0.6	0.0 ± 3.1	-3.5 ± 4.1	6.1	6.0	3.5 ± 0.9	2.55 ± 0.23	
39	J0534+2200	83.6	22.0	12.6	17.1	33.3 ± 3.6	80.4 ± 5.0	39.3	88.5	43.1 ± 1.2	2.19 ± 0.02	
40	J0542+2610	85.7	26.2	1.4	1.6	1.2 ± 3.3	7.0 ± 4.3	7.4	14.2	3.9 ± 1.0	2.67 ± 0.22	
41	J0546+3948	86.6	39.8	-2.0	-2.7	-4.3 ± 3.2	-9.4 ± 4.3	4.0	4.3	4.1 ± 0.9	2.85 ± 0.21	
42	J0556+0409	89.1	4.2	-2.4	-0.9	-17.4 ± 6.4	-12.3 ± 8.4	5.6	10.2	3.9 ± 0.7	2.45 ± 0.16	
43	J0613+4201	93.5	42.0	1.0	-1.0	5.3 ± 3.1	-4.9 ± 4.2	10.5	5.6	1.3 ± 0.5	1.92 ± 0.26	3
44	J0617+2238	94.3	22.6	2.0	1.5	4.6 ± 3.6	7.3 ± 4.8	10.7	15.3	8.3 ± 0.8	2.01 ± 0.06	
45	J0628+1847	97.2	18.8	0.1	1.3	-1.5 ± 3.8	6.1 ± 5.0	6.5	14.6	5.0 ± 0.9	2.3 ± 0.1	3
46	J0631+0642	97.9	6.7	-0.1	1.1	-2.2 ± 5.5	9.4 ± 7.0	9.4	21.2	2.4 ± 0.7	2.06 ± 0.15	5
47	J0633+1751	98.5	17.9	2.3	5.0	4.8 ± 3.9	22.5 ± 5.1	11.4	30.9	37.3 ± 0.8	1.66 ± 0.01	
48	J0634+0521	98.5	5.4	-0.2	1.7	-3.6 ± 6.1	17.9 ± 7.4	9.7	30.1	2.5 ± 0.9	2.03 ± 0.26	4
49	J0721+7120	110.4	71.4	-0.7	-1.1	-4.9 ± 6.4	-2.3 ± 7.3	9.7	12.8	3.4 ± 0.5	2.19 ± 0.11	
50	J0737+1721	114.5	17.4	0.7	0.7	4.1 ± 3.9	5.1 ± 5.1	10.9	13.9	4.2 ± 1.1	2.6 ± 0.28	
51	J0743+5447	115.8	54.8	1.4	-0.2	4.2 ± 3.5	0.1 ± 4.4	10.0	8.7	1.8 ± 0.5	2.03 ± 0.2	
52	J0808+4844	122.2	48.8	0.6	0.4	5.6 ± 3.1	-5.0 ± 4.0	10.8	5.3	2.0 ± 0.9	2.15 ± 0.45	

Table 6.2: Continued from previous page

No.	Name (3EG)	Location RA	Dec	Significance (σ) $X2$	A_4	Flux $X2$	A_4	U.L. $X2$	A_4	Flux (>100MeV)	Spectral Index (α)	Whip (>35
53	J0808+5114	122.2	51.2	0.7	-0.4	2.3 ± 3.3	-1.8 ± 4.3	8.2	7.4	2.5 ± 0.8	2.76 ± 0.34	
54	J0828+0508	127.0	5.1	-0.4	-0.3	-4.4 ± 5.9	3.2 ± 7.2	9.1	16.3	3.7 ± 1.5	2.47 ± 0.4	
55	J0829+2413	127.5	24.2	0.2	0.1	2.1 ± 3.4	3.5 ± 4.4	8.1	11.1	5.7 ± 1.2	2.42 ± 0.21	
56	J0845+7049	131.5	70.8	1.3	0.8	9.2 ± 6.1	0.8 ± 6.9	19.4	14.1	2.6 ± 0.5	2.62 ± 0.16	
57	J0853+1941	133.4	19.7	1.2	0.3	3.6 ± 3.7	-1.7 ± 4.7	9.9	8.2	1.7 ± 0.8	2.03 ± 0.35	
58	J0910+6556	137.6	65.9	-0.3	0.0	-3.0 ± 4.6	1.8 ± 5.4	7.2	11.8	1.1 ± 0.4	2.2 ± 0.26	
59	J0917+4427	139.3	44.5	3.0	2.5	8.8 ± 3.1	11.7 ± 4.0	13.9	18.4	2.6 ± 0.5	2.19 ± 0.14	
60	J0952+5501	148.0	55.0	0.2	-0.6	1.2 ± 3.5	-1.0 ± 4.3	7.7	7.9	1.6 ± 0.4	2.12 ± 0.18	
61	J0958+6533	149.6	65.6	0.1	1.1	0.5 ± 4.6	1.6 ± 5.4	9.4	11.6	1.0 ± 0.3	2.08 ± 0.24	
62	J1009+4855	152.3	48.9	-1.3	-1.7	-3.6 ± 3.1	-6.2 ± 4.0	4.2	4.7	0.7 ± 0.3	1.9 ± 0.37	
63	J1052+5718	163.2	57.3	0.9	-0.9	1.9 ± 3.6	-2.2 ± 4.4	8.3	7.2	1.2 ± 0.5	2.51 ± 0.46	
64	J1104+3809	166.1	38.2	8.7	6.1	22.6 ± 3.2	31.0 ± 4.1	27.9	37.7	1.3 ± 0.4	1.57 ± 0.15	
65	J1133+0033	173.4	0.6	0.6	2.1	-3.4 ± 8.2	15.9 ± 10.1	14.1	32.9	1.0 ± 0.6	2.73 ± 0.63	
66	J1200+2847	180.1	28.8	0.7	0.3	0.3 ± 3.2	1.0 ± 4.1	6.4	8.8	1.2 ± 0.4	1.98 ± 0.22	
67	J1212+2304	183.2	23.1	-1.7	-2.5	-3.7 ± 3.5	-12.4 ± 4.5	4.8	3.9	0.9 ± 0.3	2.76 ± 0.6	
68	J1222+2315	185.6	23.3	-1.2	-1.6	-4.3 ± 3.5	-7.5 ± 4.5	4.6	5.3	0.0 ± 0.0		
69	J1222+2841	185.8	28.7	-1.1	-0.4	-2.0 ± 3.2	-3.1 ± 4.1	5.1	6.3	1.3 ± 0.4	1.73 ± 0.18	
70	J1224+2118	186.1	21.3	1.4	1.3	3.3 ± 3.6	4.4 ± 4.7	9.6	12.5	2.9 ± 0.5	2.28 ± 0.13	
71	J1227+4302	186.8	43.0	-1.1	-0.6	-3.0 ± 3.0	-3.1 ± 4.0	4.3	6.0	0.0 ± 0.0		
72	J1229+0210	187.3	2.2	0.4	-2.0	7.5 ± 7.2	-10.5 ± 8.8	19.9	11.6	3.9 ± 0.5	2.58 ± 0.09	
73	J1230-0247	187.7	-2.8	-0.9	-0.5	-14.6 ± 10.8	-2.7 ± 11.9	13.6	21.6	2.0 ± 0.6	2.85 ± 0.3	
74	J1235+0233	188.8	2.6	1.8	1.2	14.8 ± 7.0	10.4 ± 8.8	26.3	25.4	1.5 ± 0.5	2.39 ± 0.35	
75	J1236+0457	188.9	5.0	-0.7	-0.1	-2.5 ± 5.9	1.3 ± 6.9	10.0	14.3	1.5 ± 0.6	2.48 ± 0.46	
76	J1323+2200	200.8	22.0	0.3	1.0	0.5 ± 3.6	2.2 ± 4.6	7.3	10.6	0.7 ± 0.4	1.86 ± 0.35	
77	J1329+1708	202.4	17.1	0.2	-0.3	1.8 ± 3.9	0.2 ± 4.8	8.9	9.6	1.0 ± 0.5	2.41 ± 0.47	
78	J1337+5029	204.4	50.5	1.3	2.0	2.5 ± 3.3	8.5 ± 4.2	8.4	15.4	1.2 ± 0.5	1.83 ± 0.29	

Table 6.3: Continued from previous page

	Name	Location		Significance (σ)		Flux		U.L.		Flux	Spectral Index	Whi
No.	(3EG)	RA	Dec	$X2$	A_4	$X2$	A_4	$X2$	A_4	(>100MeV)	(α)	(>3
79	J1347+2932	206.8	29.5	1.8	0.0	5.8 ± 3.1	5.0 ± 4.1	11.0	12.0	2.3 ± 1.2	2.51 ± 0.61	
80	J1424+3734	216.2	37.6	-0.4	-2.1	0.1 ± 3.2	-4.5 ± 4.1	6.3	5.6	3.9 ± 1.6	3.25 ± 0.46	
81	J1600-0351	240.2	-3.9	1.4	0.4	16.3 ± 11.6	9.0 ± 12.9	35.8	31.9	2.6 ± 0.9	2.65 ± 0.59	
82	J1605+1553	241.3	15.9	-1.3	-1.5	-6.8 ± 4.0	-7.5 ± 5.1	4.7	6.2	2.2 ± 1.1	2.06 ± 0.41	
83	J1608+1055	242.1	10.9	1.5	-0.1	8.9 ± 4.6	3.8 ± 5.8	16.5	14.2	6.5 ± 1.5	2.63 ± 0.24	
84	J1614+3424	243.5	34.4	0.9	-0.6	3.4 ± 3.2	-1.6 ± 4.1	8.9	7.1	6.0 ± 1.1	2.42 ± 0.15	
85	J1635+3813	248.9	38.2	-0.5	-1.3	-0.3 ± 3.2	-2.9 ± 4.1	6.1	6.4	10.8 ± 1.3	2.15 ± 0.09	
86	J1652-0223	253.0	-2.4	0.4	1.5	5.0 ± 10.3	14.8 ± 12.0	23.8	35.3	4.1 ± 1.1	2.53 ± 0.24	
87	J1719-0430	259.8	-4.5	0.0	0.7	5.4 ± 12.0	4.3 ± 13.9	27.5	30.2	3.1 ± 0.9	2.2 ± 0.24	
88	J1727+0429	262.0	4.5	-1.2	-0.7	-5.6 ± 6.1	-10.0 ± 7.4	8.8	9.4	4.8 ± 1.3	2.67 ± 0.26	
89	J1733+6017	263.3	60.3	1.1	-2.2	4.0 ± 3.9	-4.2 ± 4.6	10.6	6.7	2.8 ± 1.2	3 ± 0.38	
90	J1738+5203	264.6	52.1	1.2	0.1	5.4 ± 3.3	0.8 ± 4.2	10.9	8.7	4.1 ± 1.0	2.42 ± 0.23	
91	J1744-0310	266.0	-3.2	-1.3	-0.8	-18.7 ± 11.3	-22.4 ± 12.8	13.1	14.5	2.7 ± 1.1	2.42 ± 0.42	
92	J1800-0146	270.2	-1.8	-0.3	-0.5	0.6 ± 10.2	-14.6 ± 12.1	20.4	16.0	4.5 ± 1.2	2.79 ± 0.22	
93	J1822+1641	275.6	16.7	-0.5	-0.3	-0.2 ± 4.0	-0.9 ± 5.0	7.6	9.3	2.3 ± 1.5	3.06 ± 0.68	
94	J1824+3441	276.2	34.7	1.7	1.8	5.1 ± 3.2	9.7 ± 4.2	10.5	16.6	1.3 ± 0.6	2.03 ± 0.5	
95	J1825+2854	276.3	28.9	-0.4	0.5	-0.3 ± 3.2	1.8 ± 4.2	6.2	9.6	3.6 ± 1.2	4.47 ± 1.15	
96	J1828+0142	277.3	1.7	-0.3	0.0	-0.1 ± 7.5	0.4 ± 9.4	14.7	18.7	4.7 ± 1.0	2.76 ± 0.39	
97	J1835+5918	278.9	59.3	-0.5	-0.4	-3.7 ± 3.8	-5.0 ± 4.6	5.3	6.3	6.7 ± 0.8	1.69 ± 0.07	
98	J1837-0423	279.4	-4.4	-0.7	0.0	2.0 ± 12.2	-1.7 ± 14.0	25.2	26.4	5.2 ± 1.3	2.71 ± 0.44	
99	J1850+5903	282.5	59.1	1.3	-0.4	1.3 ± 3.8	-2.0 ± 4.6	8.3	7.8	3.2 ± 0.8	2.58 ± 0.41	
100	J1856+0114	284.1	1.2	2.0	3.4	7.9 ± 8.0	39.8 ± 10.2	21.8	56.5	10.1 ± 1.7	1.93 ± 0.1	
101	J1903+0550	285.9	5.8	1.9	3.7	8.3 ± 5.8	27.3 ± 7.1	18.2	38.9	13.7 ± 2.6	2.38 ± 0.17	
102	J1928+1733	292.1	17.6	0.0	3.3	-0.5 ± 3.9	16.8 ± 5.0	7.3	24.9	4.1 ± 1.7	2.23 ± 0.32	
103	J1940-0121	295.2	-1.4	-0.4	0.0	-2.7 ± 9.7	2.3 ± 11.2	17.2	23.6	3.0 ± 1.2	3.15 ± 0.39	
104	J1958+2909	299.7	29.2	3.1	3.0	9.1 ± 3.2	12.7 ± 4.2	14.3	19.7	3.7 ± 1.1	1.85 ± 0.2	

Table 6.4: Continued from previous page

	Name	Location		Significance (σ)		Flux		U.L.		Flux	Spectral Index	Whipp
No.	(3EG)	RA	Dec	$X2$	A_4	$X2$	A_4	$X2$	A_4	(>100MeV)	(α)	(>350
105	J1959+6342	299.8	63.7	-2.4	-3.0	-8.6 ± 4.2	-16.4 ± 5.2	4.3	4.1	3.1 ± 0.9	2.45 ± 0.25	
106	J2016+3657	304.1	36.9	4.7	8.5	11.3 ± 3.2	30.3 ± 4.1	16.6	37.0	6.1 ± 1.2	2.09 ± 0.11	4.
107	J2020+4017	305.3	40.3	3.9	4.4	11.2 ± 3.2	19.6 ± 4.2	16.4	26.5	21.4 ± 1.4	2.08 ± 0.04	
108	J2021+3716	305.3	37.3	6.0	10.1	14.3 ± 3.2	35.1 ± 4.1	19.6	41.9	8.1 ± 1.3	1.86 ± 0.1	3.
109	J2022+4317	305.5	43.3	3.4	2.1	9.3 ± 3.1	11.6 ± 4.1	14.5	18.3	5.2 ± 1.3	2.31 ± 0.19	
110	J2027+3429	307.0	34.5	-1.3	-1.0	-3.2 ± 3.3	-4.9 ± 4.2	4.6	5.6	5.3 ± 1.1	2.28 ± 0.15	
111	J2033+4118	308.4	41.3	3.6	6.5	8.3 ± 3.1	27.8 ± 4.2	13.5	34.6	11.2 ± 1.6	1.96 ± 0.1	
112	J2035+4441	308.9	44.7	1.6	2.2	6.3 ± 3.2	9.8 ± 4.0	11.6	16.4	5.1 ± 1.5	2.08 ± 0.26	
113	J2036+1132	309.2	11.5	-0.6	0.1	-0.3 ± 4.5	2.3 ± 5.6	8.6	12.6	3.9 ± 1.1	2.83 ± 0.26	
114	J2046+0933	311.6	9.6	1.0	1.5	5.1 ± 4.7	8.3 ± 6.0	13.1	18.4	1.5 ± 0.8	2.22 ± 0.51	
115	J2100+6012	315.2	60.2	-1.1	-0.1	-4.3 ± 3.9	0.0 ± 4.6	5.3	9.1	3.8 ± 1.1	2.21 ± 0.25	
116	J2202+4217	330.6	42.3	0.3	-0.7	-0.1 ± 3.1	-3.4 ± 4.0	6.0	6.0	2.8 ± 0.9	2.6 ± 0.28	
117	J2206+6602	331.6	66.1	2.1	3.1	8.3 ± 4.7	12.4 ± 5.4	16.2	21.3	5.0 ± 1.5	2.29 ± 0.26	
118	J2209+2401	332.4	24.0	-0.2	0.6	-0.8 ± 3.3	4.2 ± 4.2	6.0	11.5	1.6 ± 0.8	2.48 ± 0.5	
119	J2227+6122	336.8	61.4	1.2	4.7	1.1 ± 3.9	19.2 ± 4.7	8.4	27.0	8.2 ± 1.5	2.24 ± 0.14	3.
120	J2232+1147	338.1	11.8	0.8	2.4	4.2 ± 4.5	13.5 ± 5.6	12.1	22.8	4.5 ± 0.8	2.45 ± 0.14	
121	J2243+1509	340.8	15.2	1.1	-0.8	6.6 ± 4.0	-0.2 ± 5.1	13.3	9.8	0.0 ± 0.0		
122	J2248+1745	342.2	17.8	-1.2	-1.6	-1.3 ± 3.9	-7.5 ± 4.9	6.8	5.9	2.3 ± 1.0	2.11 ± 0.39	4.
123	J2254+1601	343.5	16.0	-0.1	0.7	0.1 ± 4.0	0.8 ± 5.0	7.9	10.3	10.4 ± 0.9	2.21 ± 0.06	
124	J2255+1943	344.0	19.7	0.1	2.0	-3.0 ± 3.7	9.5 ± 4.6	5.5	17.1	1.3 ± 0.8	2.36 ± 0.61	
125	J2314+4426	348.7	44.4	1.1	-1.0	4.2 ± 3.1	-3.1 ± 4.0	9.4	6.0	3.0 ± 1.1	2.34 ± 0.32	
126	J2321-0328	350.4	-3.5	0.3	-0.9	-3.6 ± 10.9	-9.2 ± 12.2	19.1	18.7	0.0 ± 0.0		
127	J2352+3752	358.1	37.9	-1.6	-0.9	-2.2 ± 3.2	-2.5 ± 4.1	5.0	6.6	1.4 ± 1.0	2.47 ± 0.68	
128	J2358+4604	359.6	46.1	0.8	1.9	2.6 ± 3.1	6.6 ± 4.0	8.1	13.2	3.2 ± 1.2	2.38 ± 0.38	
129	J2359+2041	360.0	20.7	0.5	-0.3	2.4 ± 3.6	0.6 ± 4.7	8.9	9.5	1.4 ± 0.7	2.09 ± 0.35	

Table 6.5: Continued from previous page

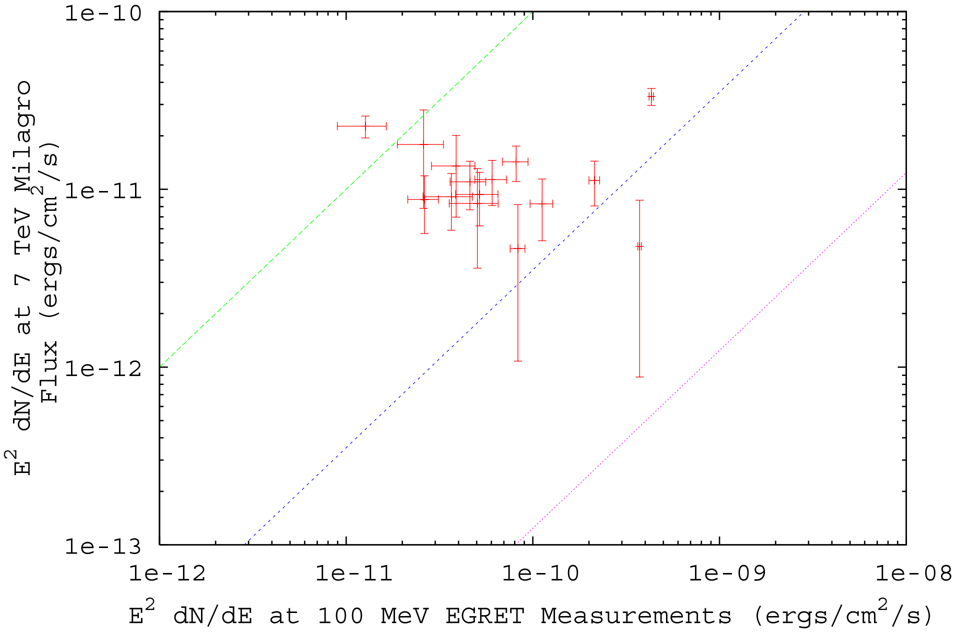

Figure 6.3: Milagro fluxes at 7 TeV versus EGRET measurements at 100 MeV. The green, blue and pink lines represent the equal energy flux lines assuming the flux power law α equal -2.0, -2.3 and -2.6 respectively from EGRET energy to Milagro energy.

6.5.2 Comparison of Milagro and EGRET Results

Figure 6.3 to figure 6.10 compare Milagro measurements at 7 TeV (for $X2$ analysis) and 25 TeV (for A_4 analysis) with EGRET measurements at 100 MeV and EGRET extrapolations to 7 TeV and 25 TeV respectively. For any EGRET source if the significance measured by Milagro is greater than 2 σ the flux is plotted and if less than 2 σ then the upper limit for 95% confidence level is plotted for both $X2$ and A_4 analyses. The spectral indices are taken from 3EG catalog. In the 129 EGRET sources, 5 of them do not have measured spectral index by EGRET, so they are not included in these plots.

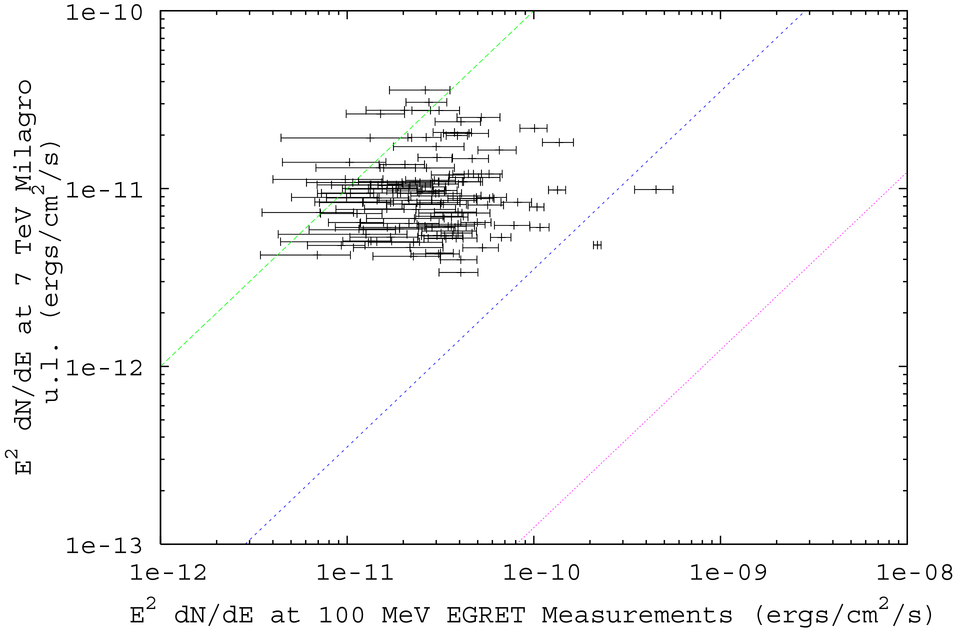

Figure 6.4: Milagro upper limits at 7 TeV versus EGRET measurements at 100 MeV. The green, blue and pink lines represent the equal energy flux lines assuming the flux power law α equal -2.0, -2.3 and -2.6 respectively from EGRET energy to Milagro energy.

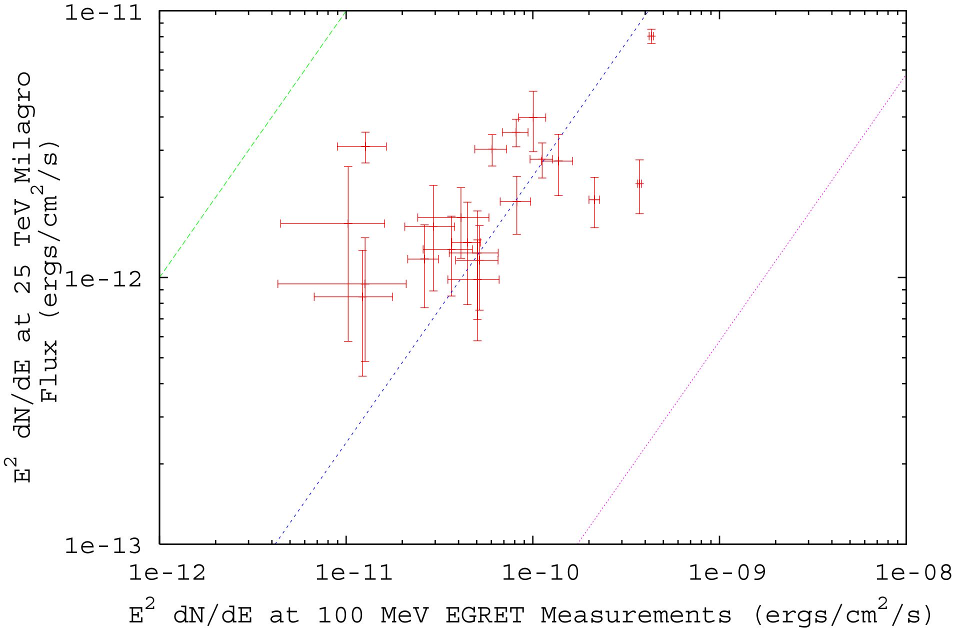

Figure 6.5: Milagro fluxes at 25 TeV versus EGRET measurements at 100 MeV. The green, blue and pink lines represent the equal energy flux lines assuming the flux power law α equal -2.0, -2.3 and -2.6 respectively from EGRET energy to Milagro energy.

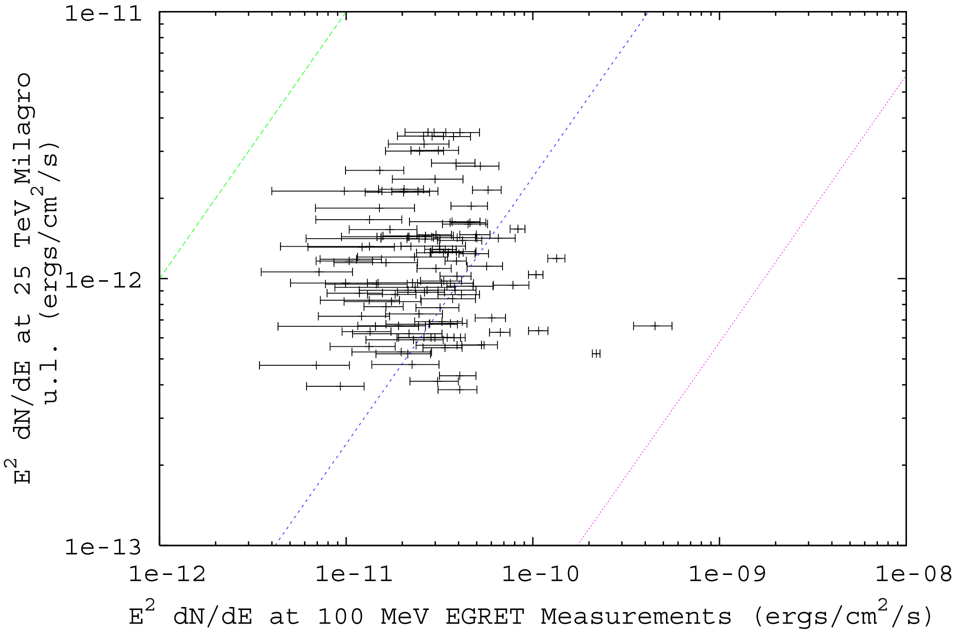

Figure 6.6: Milagro upper limits at 25 TeV versus EGRET measurements at 100 MeV. The green, blue and pink lines represent the equal energy flux lines assuming the flux power law α equal -2.0, -2.3 and -2.6 respectively from EGRET energy to Milagro energy.

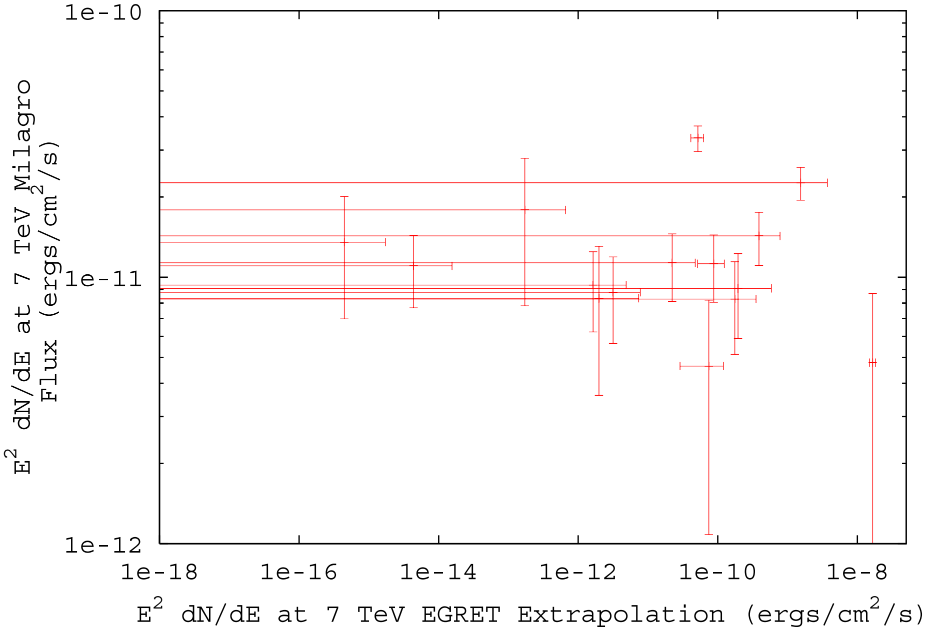

Figure 6.7: Milagro fluxes at 7 TeV versus EGRET extrapolation to 7 TeV.

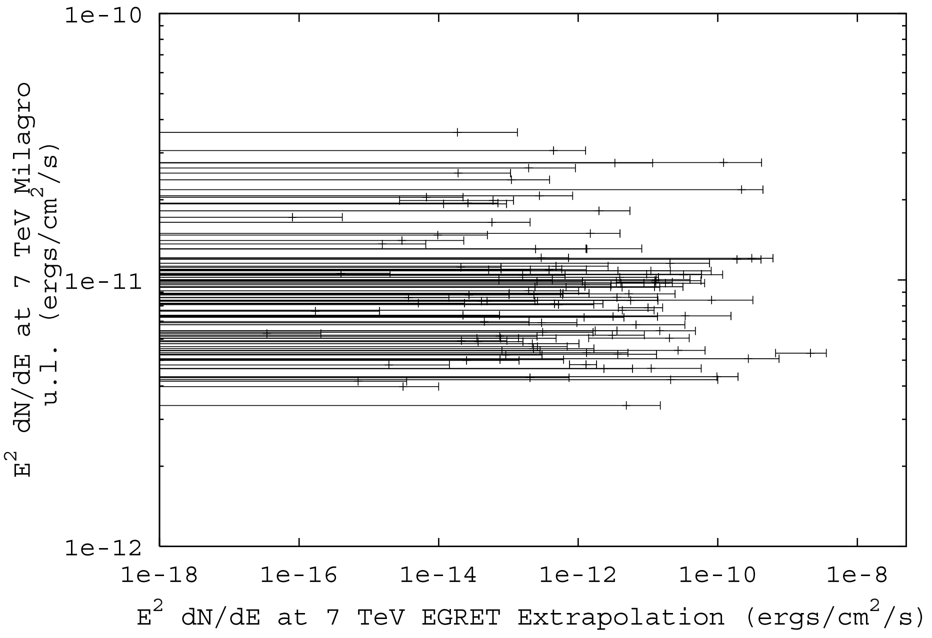

Figure 6.8: Milagro upper limits at 7 TeV versus EGRET extrapolation to 7 TeV.

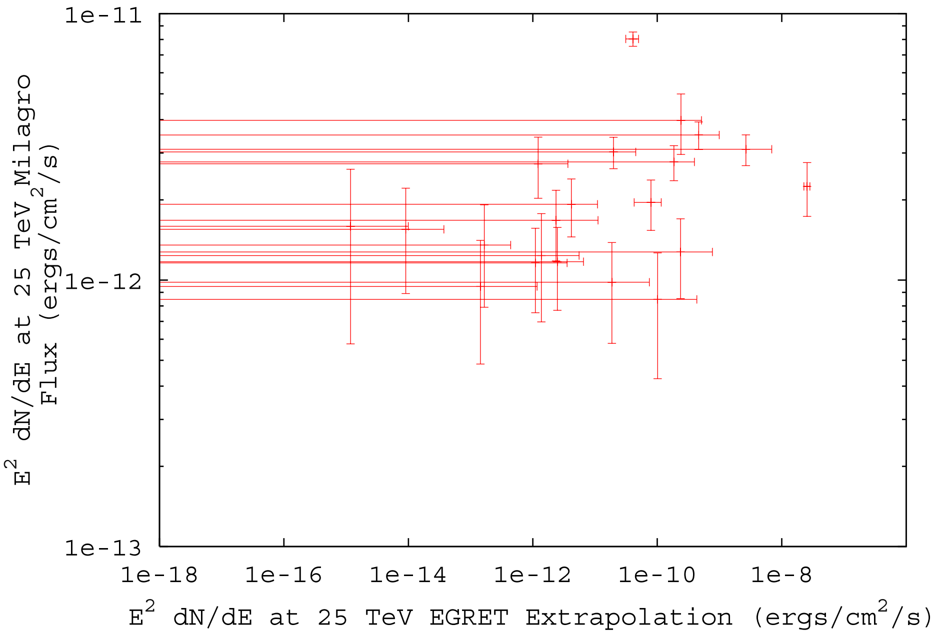

Figure 6.9: Milagro fluxes at 25 TeV versus EGRET extrapolation to 25 TeV.

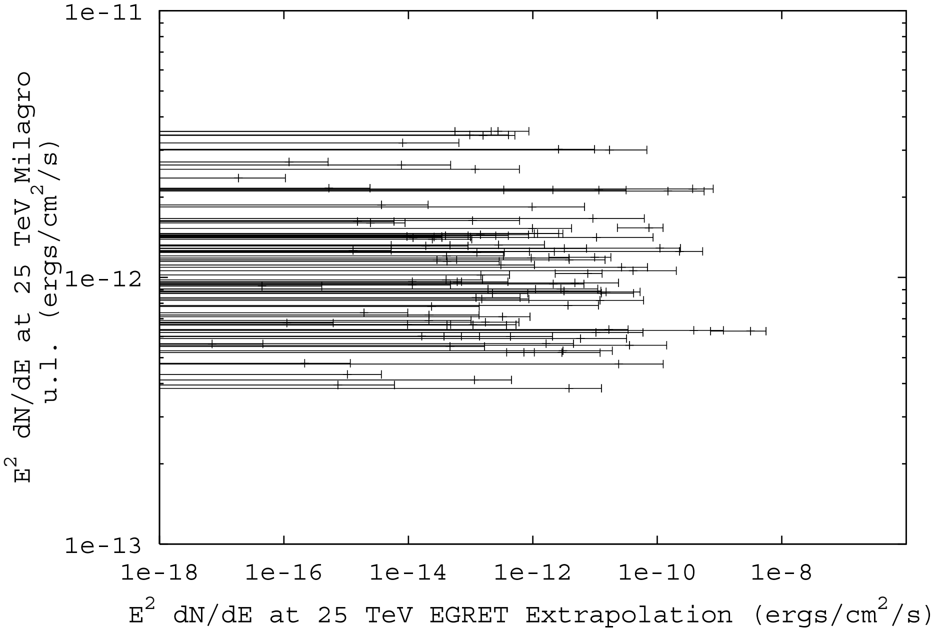

Figure 6.10: Milagro upper limits at 25 TeV versus EGRET extrapolation to 25 TeV.

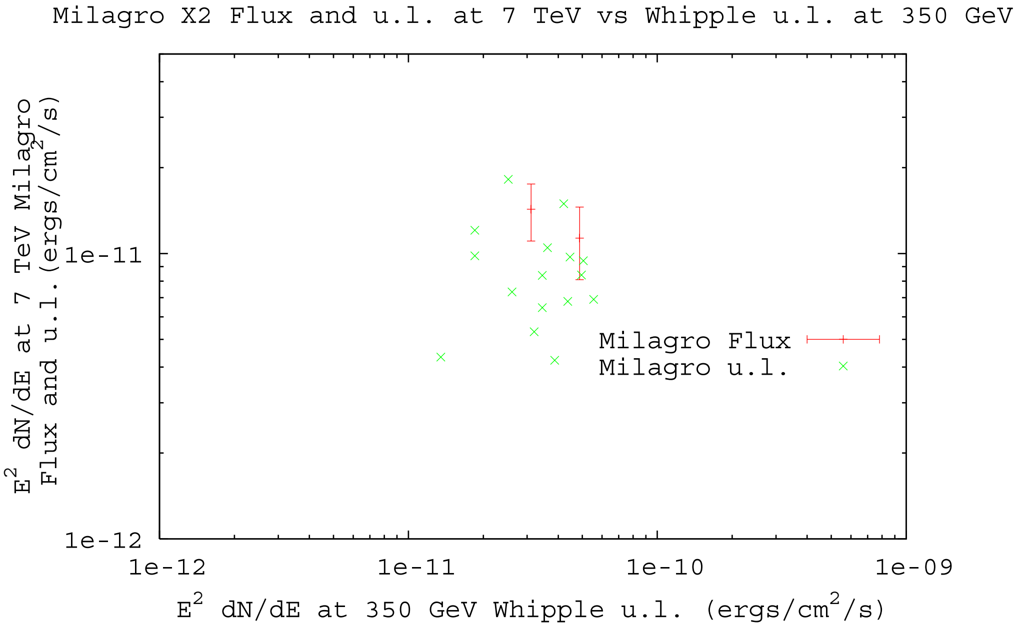

Figure 6.11: Milagro flux and u.l. at 7 TeV versus Whipple u.l. at 350GeV.

6.5.3 Comparison of Milagro and Whipple Results

Figure 6.11 to 6.14 compare Milagro measurements of 18 unidentified sources at 7 TeV (for $X2$ analysis) and 25 TeV (for A_4 analysis) with Whipple measurements at 350 GeV and Whipple extrapolation to 7 TeV and 25 TeV respectively. For any source if the significance measured by Milagro is greater than 2 σ the flux is plotted and if less than 2 σ then the upper limit for 95 % confidence level is plotted for either $X2$ or A_4 analysis. The spetral index used to extrapolate Whipple upper limits from 350 GeV to 7 TeV and 25 TeV is a Crab like spectrum (≈ -2.5) which was measurement by Whipple observatory [48].

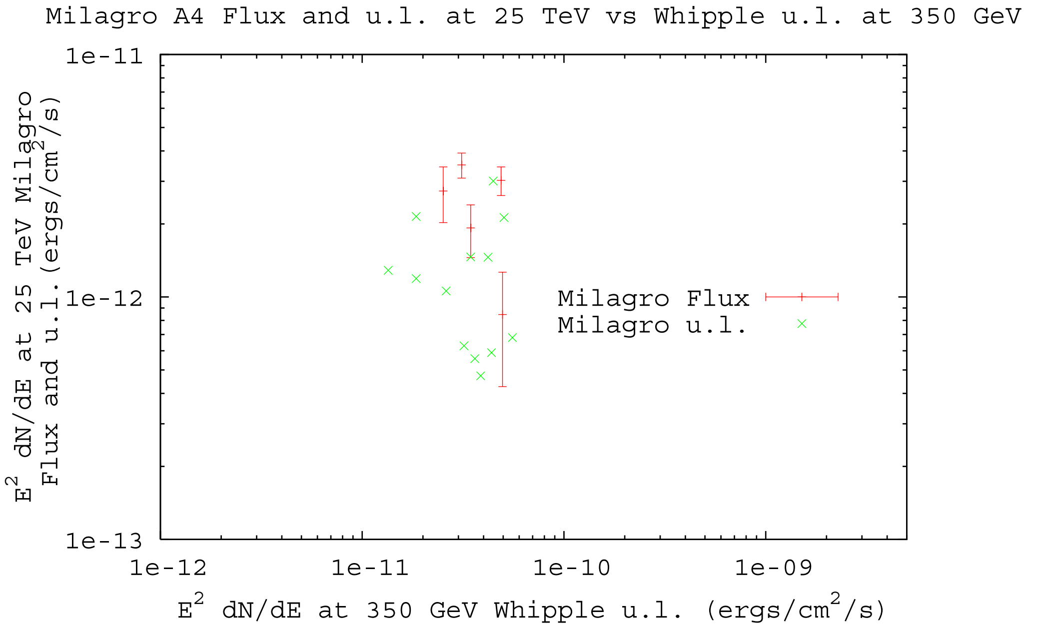

Figure 6.12: Milagro flux and u.l. at 25 TeV versus Whipple u.l. at 350 GeV.

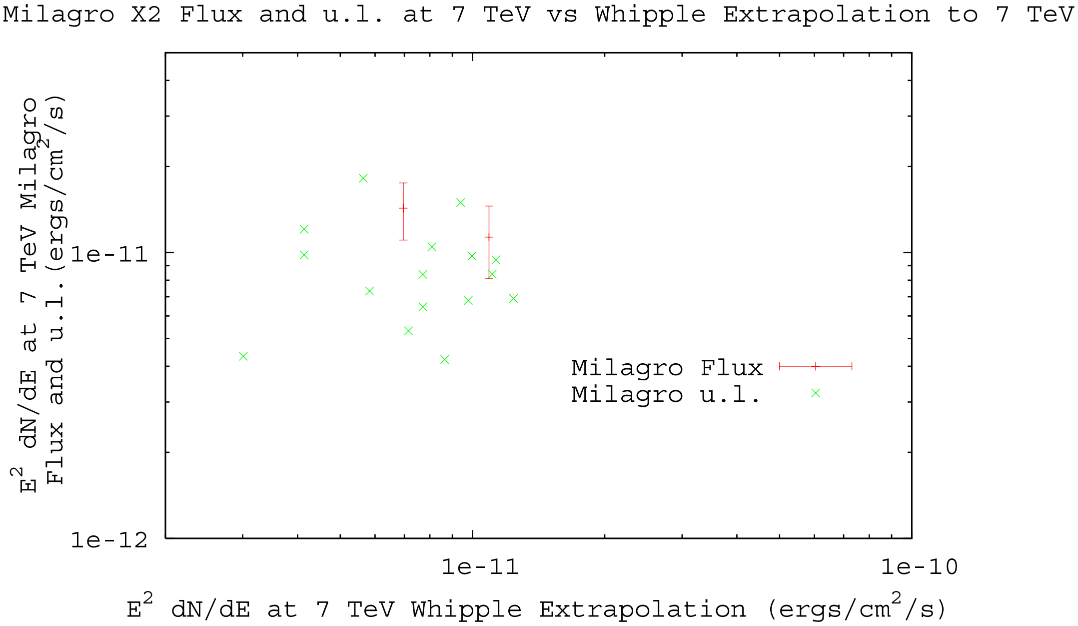

Figure 6.13: Milagro flux and u.l. at 7 TeV versus Whipple extrapolation to 7 TeV.

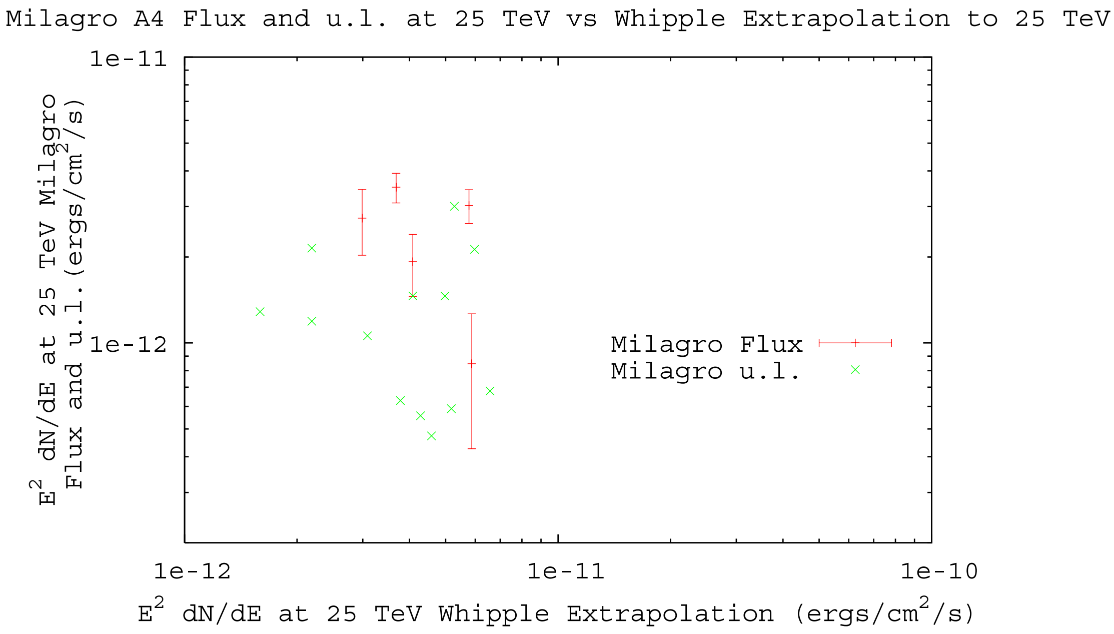

Figure 6.14: Milagro flux and u.l. at 25 TeV versus Whipple extrapolation to 25 TeV.

6.5.4 Spectra of EGRET Sources with Whipple and Milagro Upper Limits

The plots in this section show the spectral measurments from the EGRET observations together with an extrapolation of the power law spectrum to 25 TeV and the upper limits from Whipple upper limits above 350 GeV and Milagro upper limits above 7 TeV and 25 TeV. The three lines in each plot represent spectrum and ± 1σ error on the spectrum. Detailed results for each source are followed up.

1. **3EG J0010+7309** (figure 6.15): Whipple and Milagro upper limits are all below the EGRET spectrum. A cut-off is required in the spectrum between 100 MeV and 350 GeV.

2. **3EG J0241+6103** (figure 6.16): Whipple upper limit at 350 GeV and Milagro upper limit at 7 TeV do not constrain the extrapolated EGRET spectrum. But EGRET spectrum is constrained by the Milagro upper limit at 25 TeV. A cut-off is required between 7 TeV and 25 TeV.

3. **3EG J0423+1707** (figure 6.17): In the case of J0423+1707 the soft EGRET spectrum is not constrained by the Whipple and Milagro VHE upper limits.

4. **3EG J0433+2908** (figure 6.18): Figure J0433+2908 shows the EGRET power-law spectrum extrapolation to 25 TeV, with the Whipple and Milagro upper limits superimposed. A cut-off in the spectrum is required between 100 MeV to 350 GeV to reconcile these observations.

5. **3EG J0450+1105** (figure 6.19): The EGRET spectrum is not constrained by the Whipple and Milagro upper limits.

6. **3EG J0613+4201** (figure 6.20): For EGRET unidentified source J0613+4201 the limits derived from Whipple and Milagro observations are not sensitive enough to rule out a simple extrapolation of the EGRET spectrum into the VHE regime between 100 MeV and 7 TeV. But a cut-off is required between 7 TeV and 25 TeV.

7. **3EG J0628+1847** (figure 6.21): The EGRET spectrum is not constrained by the Whipple and Milagro upper limits.

8. **3EG J0631+0642** (figure 6.22): Due to the large uncertainty in the EGRET spectrum, an extrapolation of the EGRET spectrum to 350 GeV, 7 TeV and 25 TeV is not significantly constrained by Whipple and Milagro upper limits.

9. **3EG J0634+0521** (figure 6.23): The EGRET spectrum is not significantly constrained by Whipple and Milagro upper limits.

10. **3EG J1009+4855** (figure 6.24): The EGRET spectrum is not significantly constrained by Whipple and Milagro upper limits.

11. **3EG J1323+2200** (figure 6.25): The EGRET spectrum is not significantly constrained by Whipple and Milagro upper limits at VHE energy ranges due to the large uncertainty in the EGRET spectrum.

12. **3EG J1337+5029** (figure 6.26): Whipple upper limit at 350 GeV and Milagro upper limit at 7 TeV do not constrain the extrapolated EGRET spectrum. But EGRET spectrum is constrained by the Milagro upper limit at 25 TeV. A cut-off

is required between 7 TeV and 25 TeV.

13. **3EG J1835+5918** (figure 6.27): Whipple and Milagro upper limits constrain the EGRET spectrum. A cut-off of EGRET spectrum between 100 MeV and 350 GeV is required.

14. **3EG J1903+0550** (figure 6.28): The EGRET spectrum is not significantly constrained by Whipple and Milagro upper limits.

15. **3EG J2016+3657** (figure 6.29): The EGRET spectrum is not significantly constrained by Whipple and Milagro upper limit at 7 TeV. But a cut-off is required between 7 TeV and 25 TeV.

16. **3EG J2021+3716** (figure 6.30): A cut-off of EGRET spectrum between 100 MeV and 25 TeV is required due to the Whipple and Milagro upper limits at 350 GeV, 7 TeV and 25 TeV.

17. **3EG J2227+6122** (figure 6.31): The EGRET spectrum between 100 MeV and 25 TeV is not significantly constrained by Whipple and Milagro upper limits.

18. **3EG J2248+1745** (figure 6.32): The EGRET spectrum is not significantly constrained by Whipple and Milagro upper limits due to the large spectrum uncertainty of EGRET measurement at 100 MeV.

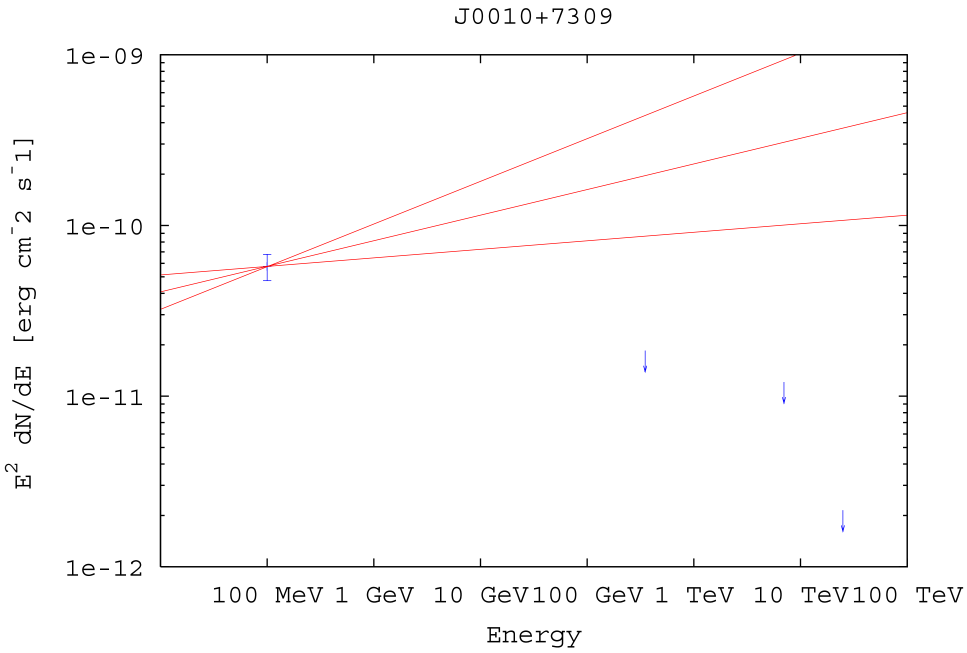

Figure 6.15: Spectrum of J0010+7309 with the upper limits at 350 GeV from Whipple observation, and 7 TeV and 25 TeV from Milagro observation.

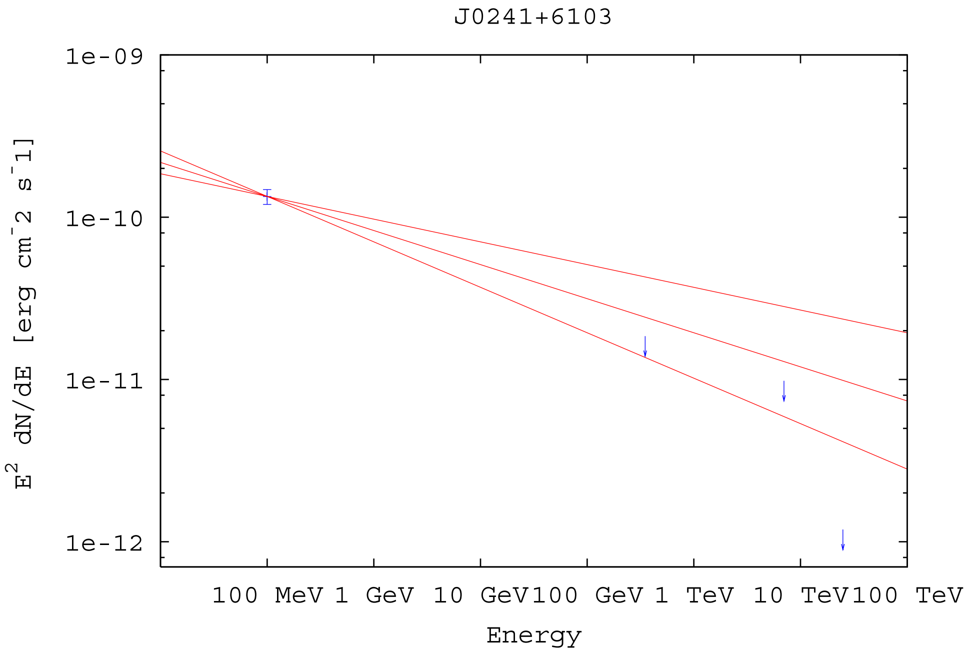

Figure 6.16: Spectrum of J0241+6103 with the upper limits at 350 GeV from Whipple observation, and 7 TeV and 25 TeV from Milagro observation.

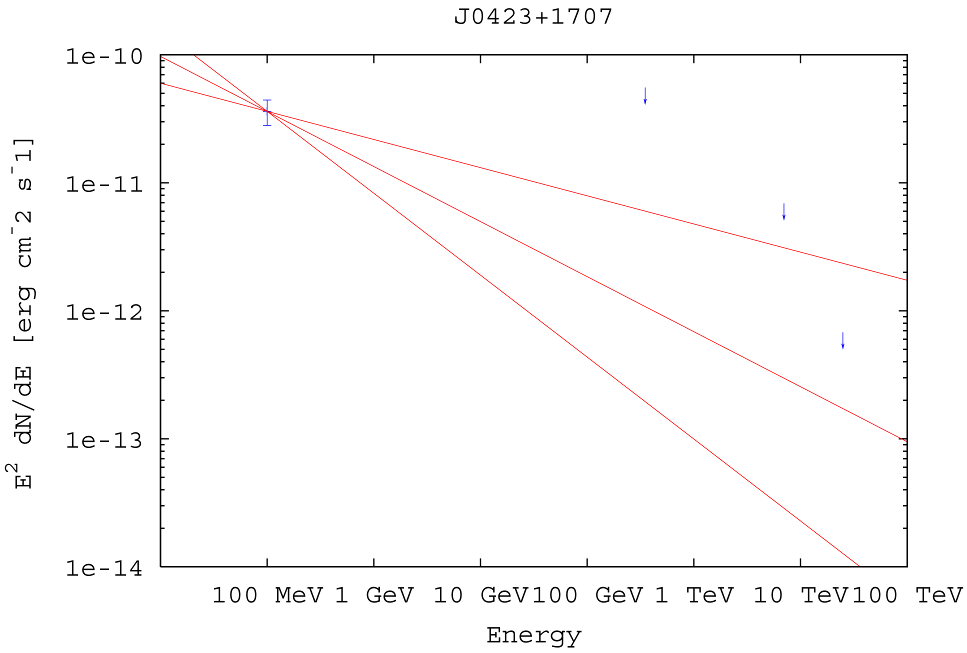

Figure 6.17: Spectrum of J0423+1707 with the upper limits at 350 GeV from Whipple observation, and 7 TeV and 25 TeV from Milagro observation.

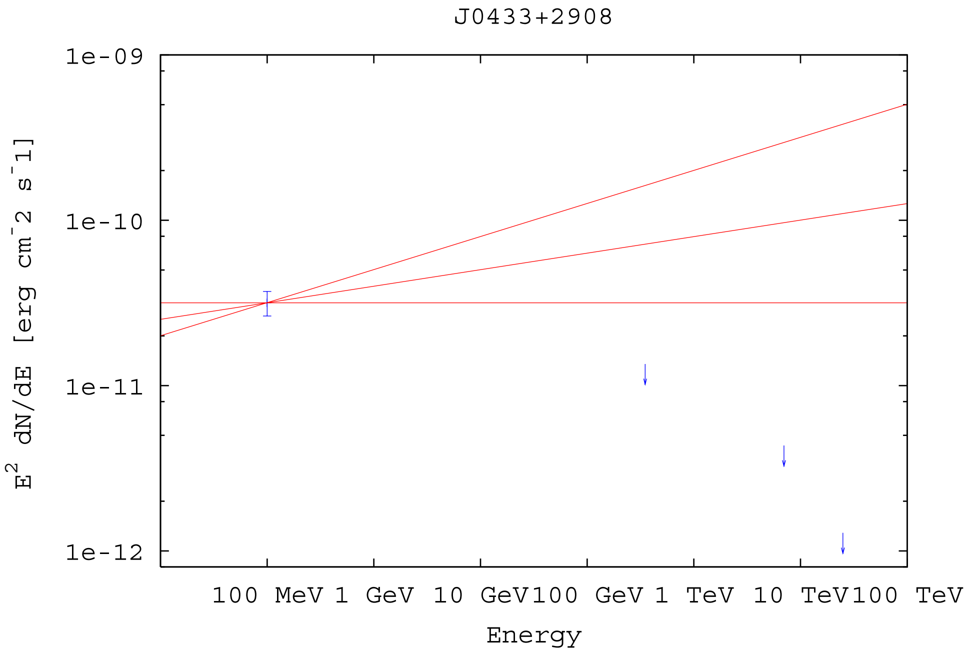

Figure 6.18: Spectrum of J0433+2908 with the upper limits at 350 GeV from Whipple observation, and 7 TeV and 25 TeV from Milagro observation.

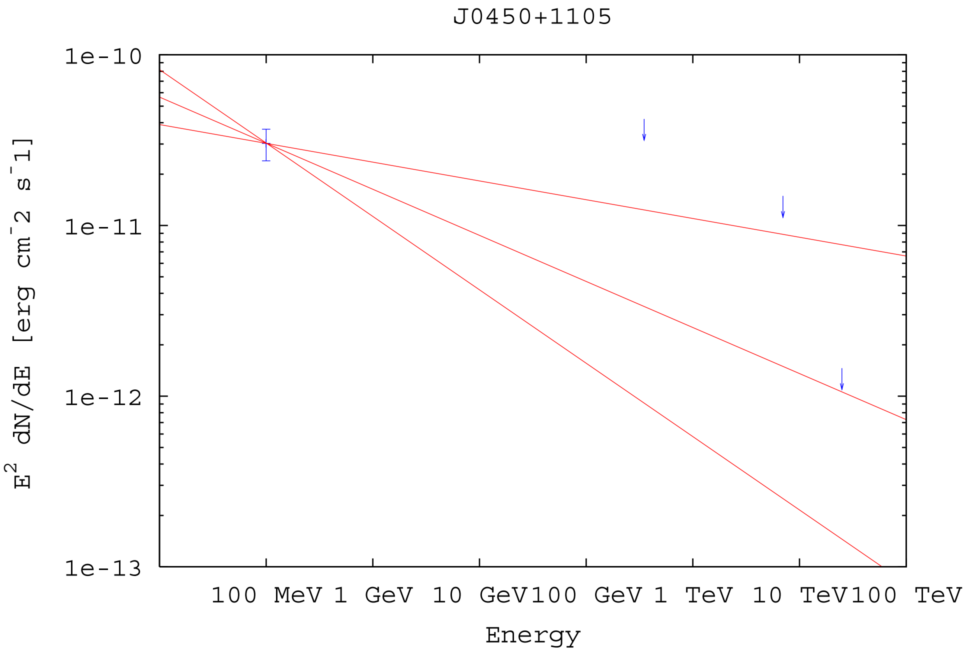

Figure 6.19: Spectrum of J0450+1105 with the upper limits at 350 GeV from Whipple observation, and 7 TeV and 25 TeV from Milagro observation.

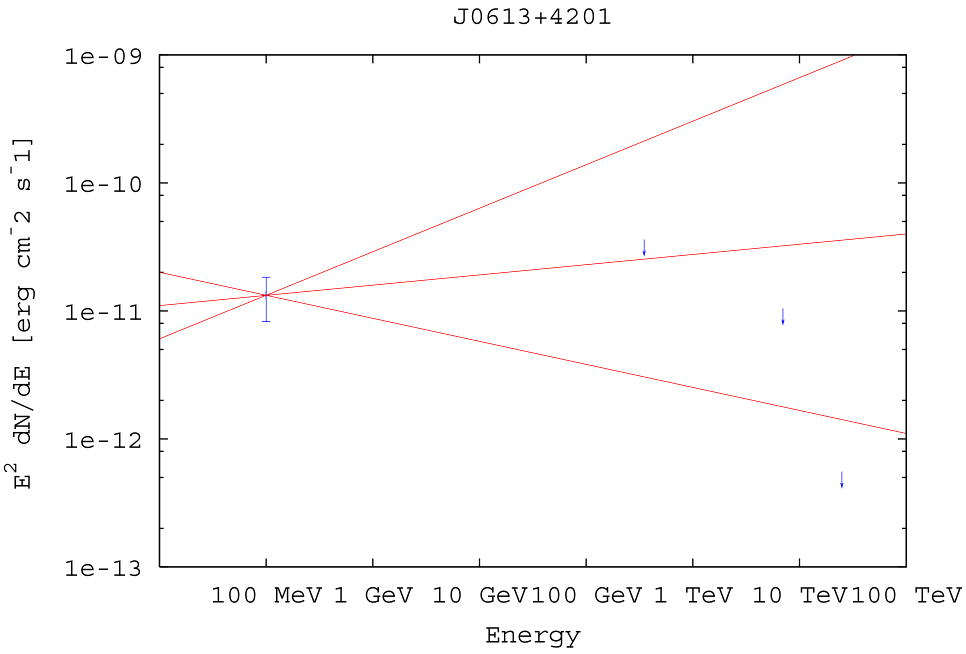

Figure 6.20: Spectrum of J0613+4201 with the upper limits at 350 GeV from Whipple observation, and 7 TeV and 25 TeV from Milagro observation.

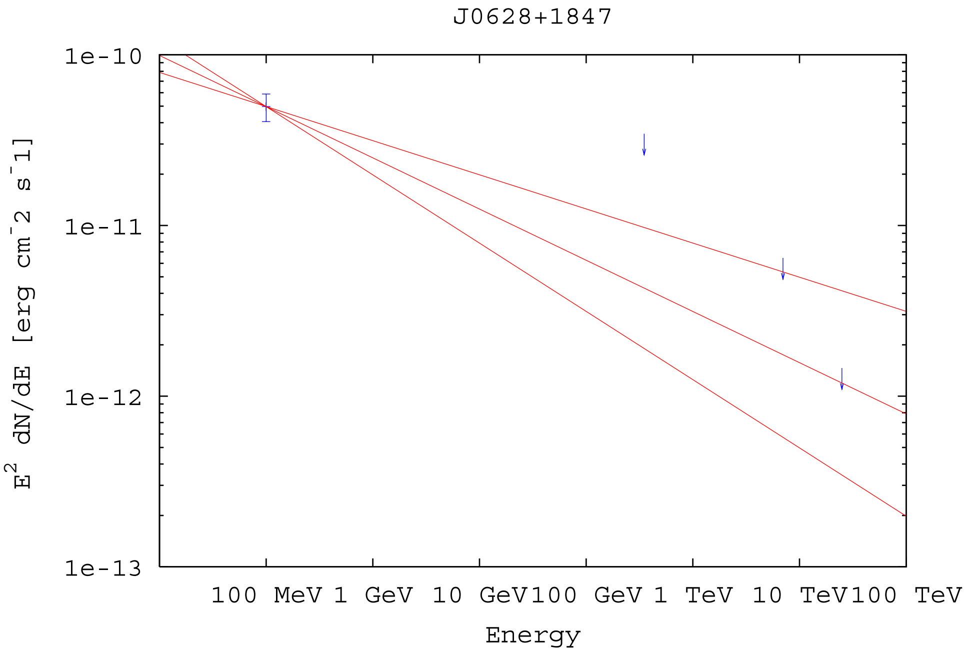

Figure 6.21: Spectrum of J0628+1847 with the upper limits at 350 GeV from Whipple observation, and 7 TeV and 25 TeV from Milagro observation.

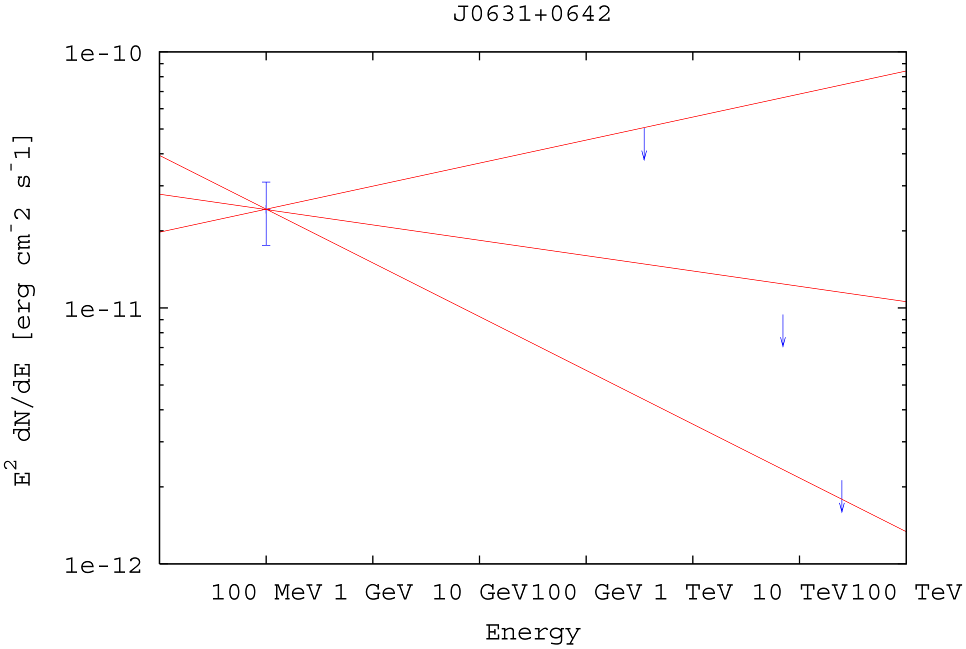

Figure 6.22: Spectrum of J0631+0642 with the upper limits at 350 GeV from Whipple observation, and 7 TeV and 25 TeV from Milagro observation.

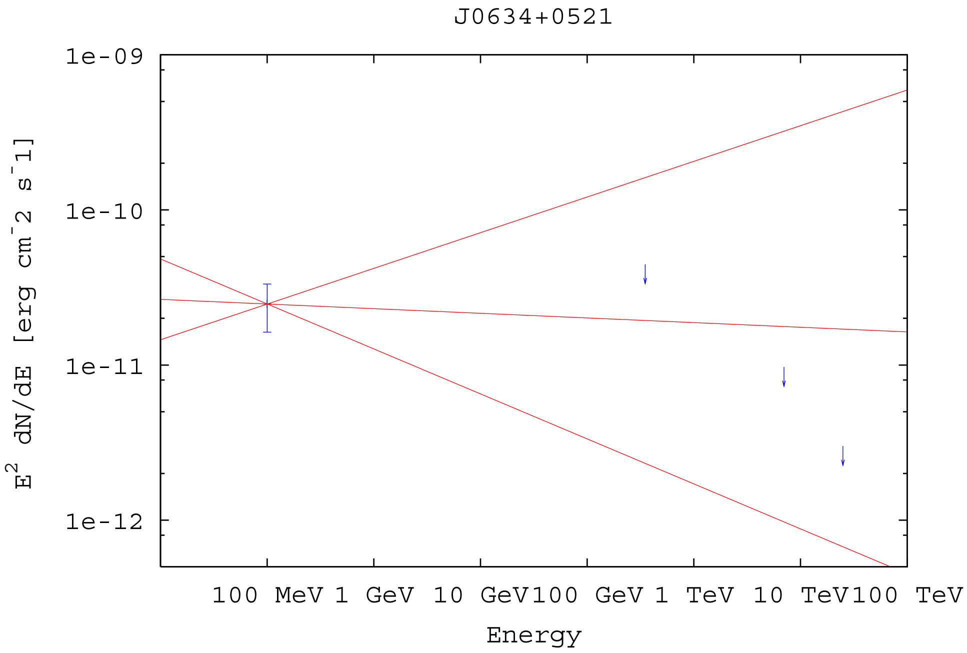

Figure 6.23: Spectrum of J0634+0521 with the upper limits at 350 GeV from Whipple observation, and 7 TeV and 25 TeV from Milagro observation.

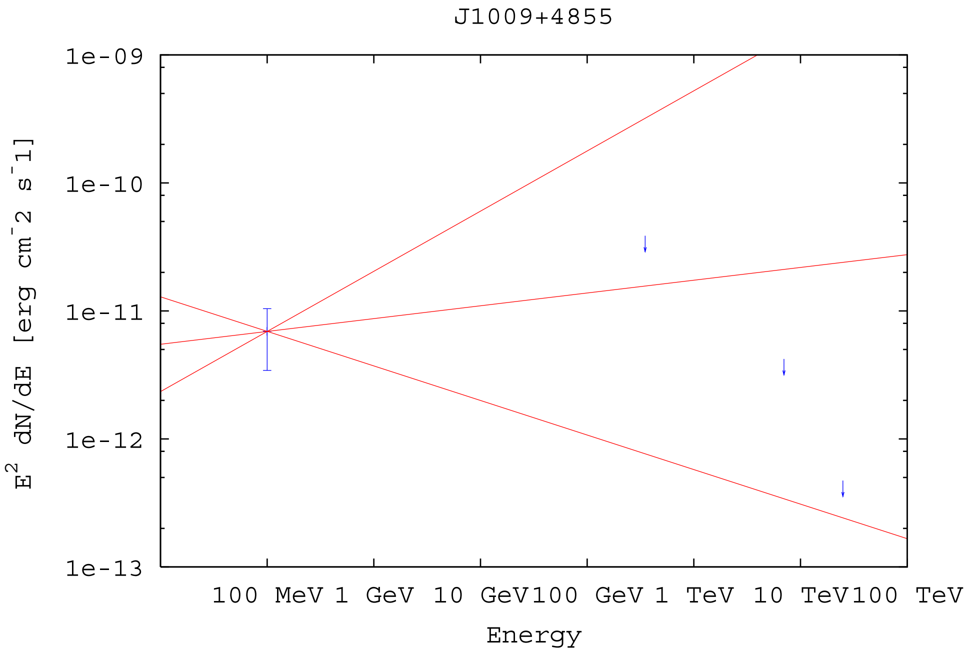

Figure 6.24: Spectrum of J1009+4855 with the upper limits at 350 GeV from Whipple observation, and 7 TeV and 25 TeV from Milagro observation.

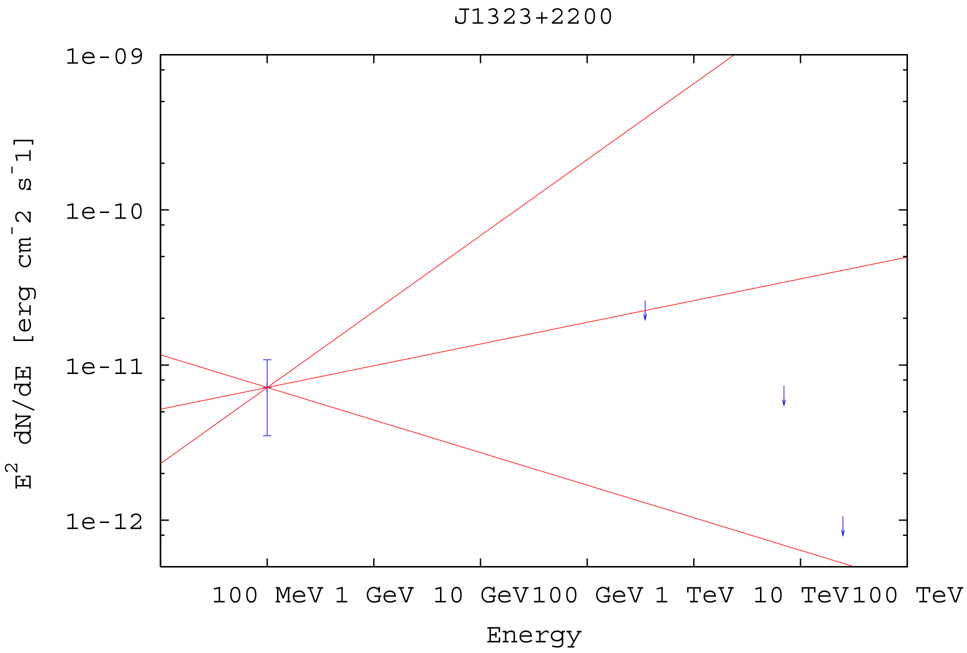

Figure 6.25: Spectrum of J1323+2200 with the upper limits at 350 GeV from Whipple observation, and 7 TeV and 25 TeV from Milagro observation.

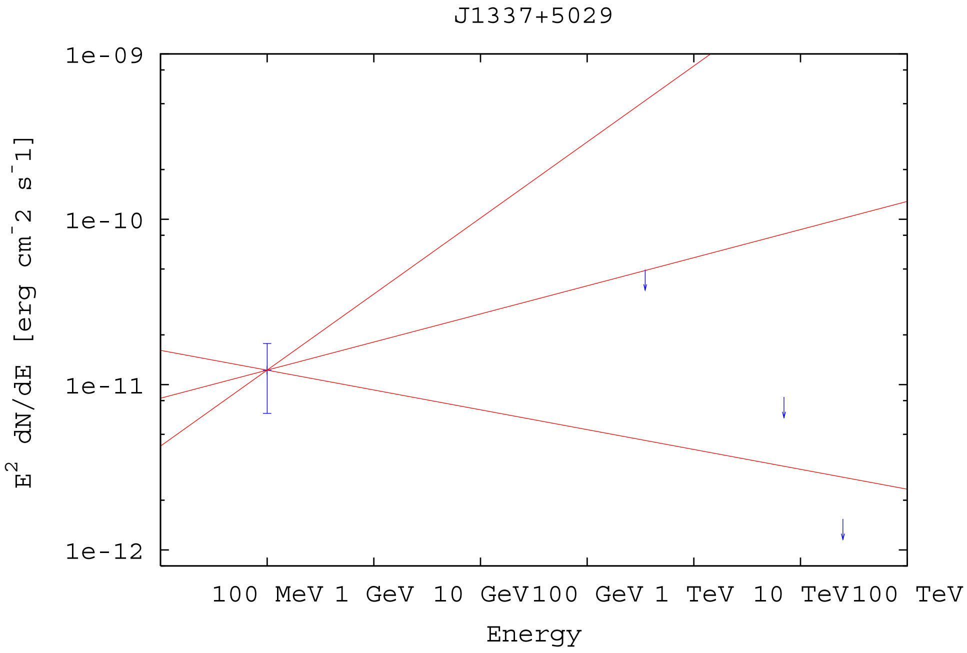

Figure 6.26: Spectrum of J1337+5029 with the upper limits at 350 GeV from Whipple observation, and 7 TeV and 25 TeV from Milagro observation.

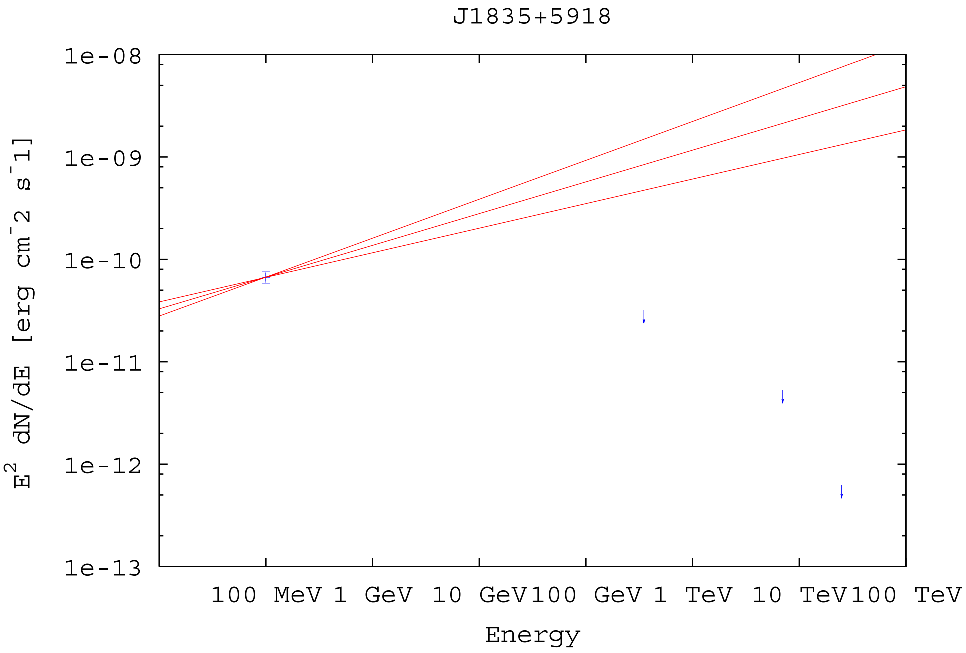

Figure 6.27: Spectrum of J1835+5918 with the upper limits at 350 GeV from Whipple observation, and 7 TeV and 25 TeV from Milagro observation.

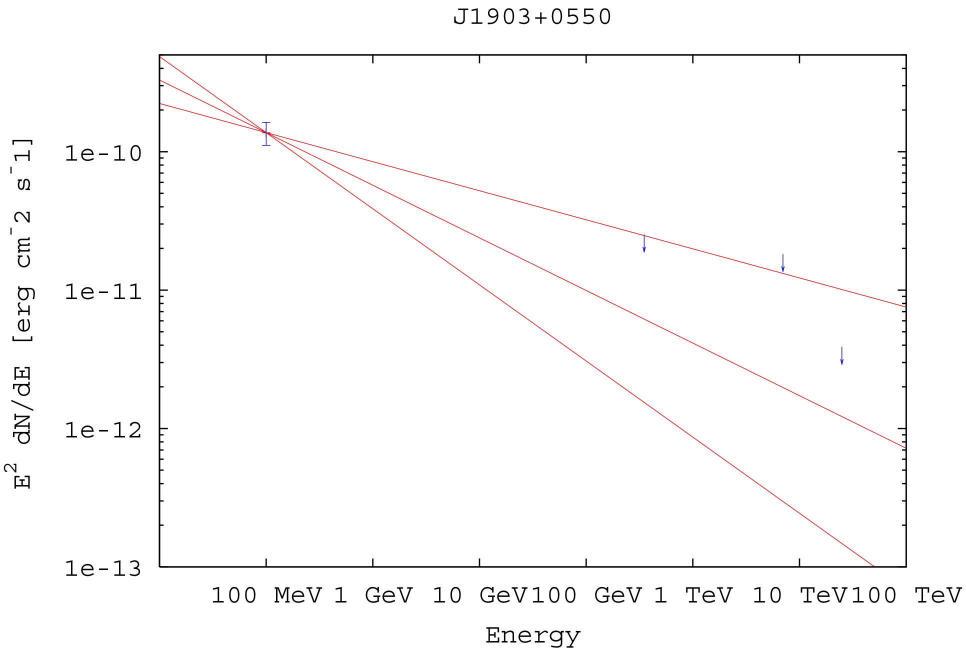

Figure 6.28: Spectrum of J1903+0550 with the upper limits at 350 GeV from Whipple observation, and 7 TeV and 25 TeV from Milagro observation.

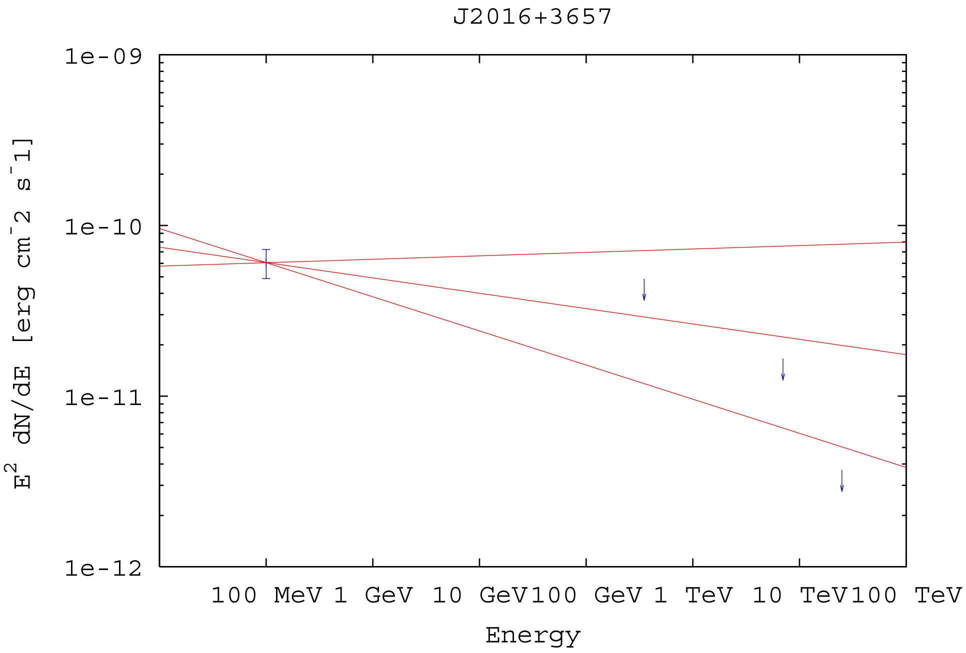

Figure 6.29: Spectrum of J2016+3657 with the upper limits at 350 GeV from Whipple observation, and 7 TeV and 25 TeV from Milagro observation.

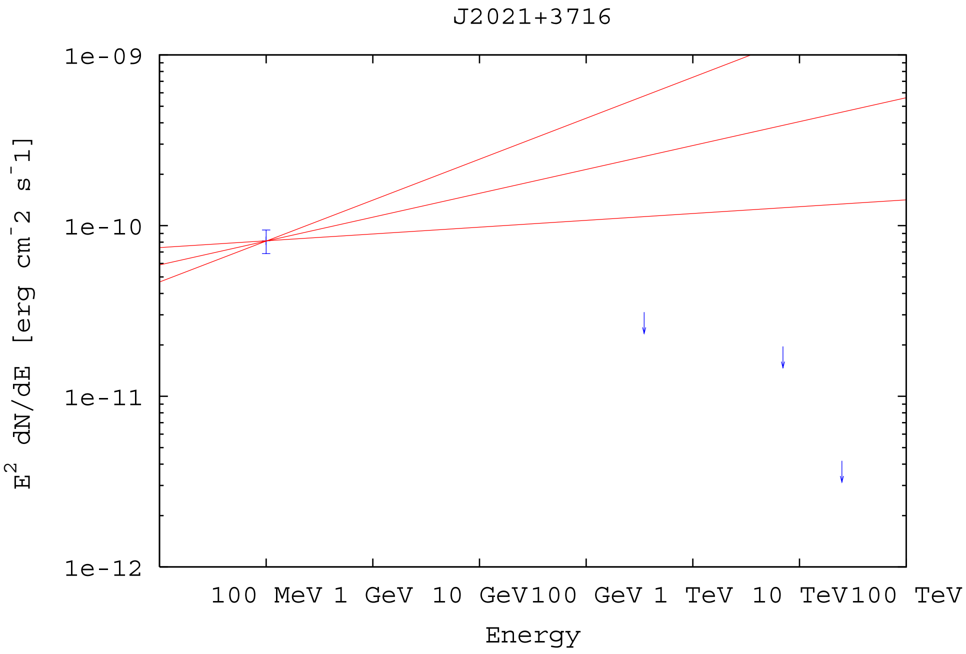

Figure 6.30: Spectrum of J2021+3716 with the upper limits at 350 GeV from Whipple observation, and 7 TeV and 25 TeV from Milagro observation.

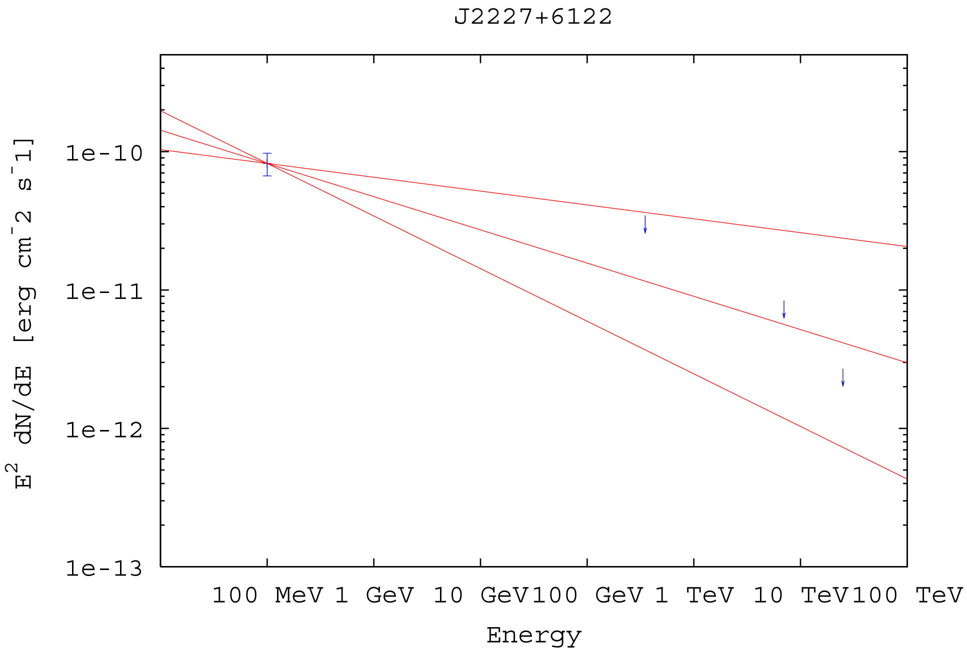

Figure 6.31: Spectrum of J2227+6122 with the upper limits at 350 GeV from Whipple observation, and 7 TeV and 25 TeV from Milagro observation.

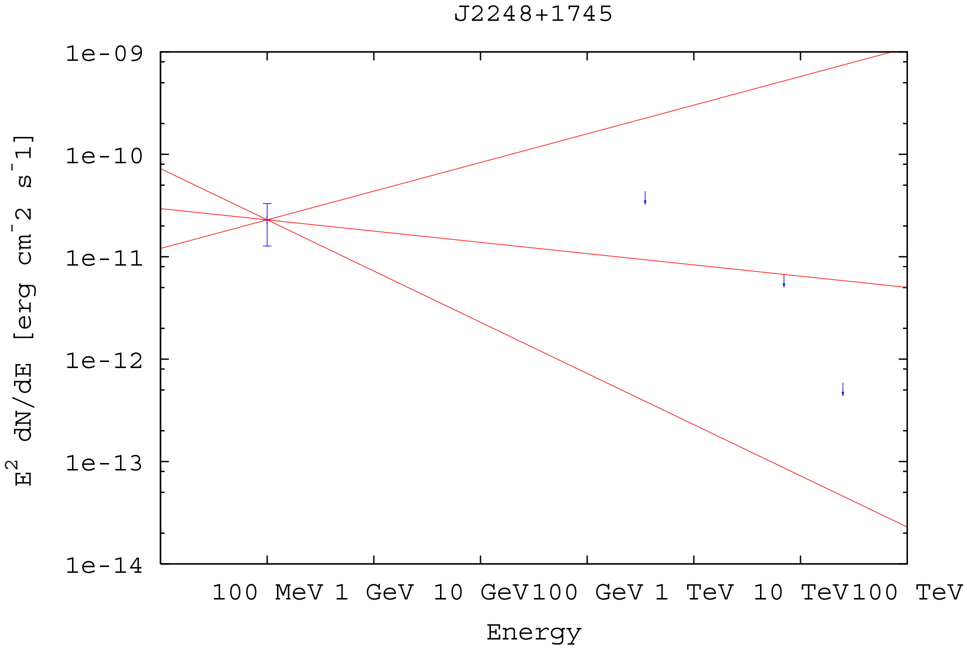

Figure 6.32: Spectrum of J2248+1745 with the upper limits at 350 GeV from Whipple observation, and 7 TeV and 25 TeV from Milagro observation.

Chapter 7

Conclusions

A survey of 129 EGRET sources in 3EG catalog has been performed with Milagro. Two different γ-hadron separation variables, $X2$ and A_4, along with A_4 weighted analysis and PSF smoothed method were used to analyze Milagro data. The median energies are 7 TeV and 25 TeV respectively. Monte Carlo simulation results to determine the optimum analysis technique due to the number of trials is presented. Flux and flux upper limit at 7 TeV and 25 TeV of these 129 EGRET sources are computed. Most of the EGRET source's spectral index between 100 MeV and 25 TeV are steeper than -2.0 and flatter than -2.6. In the 18 EGRET unidentified sources that Whipple observatory measured, Milagro data puts constrains at 7 TeV and 25 TeV on sources J0010+7309, J0433+2908, J1835+5918, and J2021+3716. Milagro data puts constrains at 25 TeV on sources J0241+6103, J0613+4201, J1337+5029, and J2016+3657. For the remaining sources Milagro data does not provide additional constraints at TeV energies, and are consistent with extrapolations from EGRET.

A continuation of this work would be detailed studies of the EGRET sources on spectral shape and the time variability, especially for high significance sources. The next generation of water Cherenkov telescope, such as HAWC (High Altitude Water Cherenkov Telescope) which is currently being proposed, is about 15 times sensetive than Milagro. Also the space-based telescope, GLAST (Gamma Ray Large Space Telescope) is scheduled for launch in May 2008. GLAST is sensitive at energies from 20 MeV to 300 GeV. Compared with EGRET, GLAST has better angular resolution ($< 0.15^\circ$) and larger collection area (~ 1 m^2). It is expected to reduce the source location error by as much as a factor 100 depending on the energy spectrum of photons detected and the local γ-ray background [49]. GLAST is expected to discover ≈ 1000 new γ-ray sources and HAWC will check their TeV compontents. Due to the overlap on the energy ranges the results of GLAST can be directly compared with HAWC results.

Appendix A

Distributions of the Maximum Posttrial Significance

In this section, distributions of the maximum posttrial significance for PSF and bin smoothed maps when σ_s equals 0°, 0.2°, and 0.5° and the radius of the search area equals 0°, 0.5°, 1.0° and 1.5° are plotted.

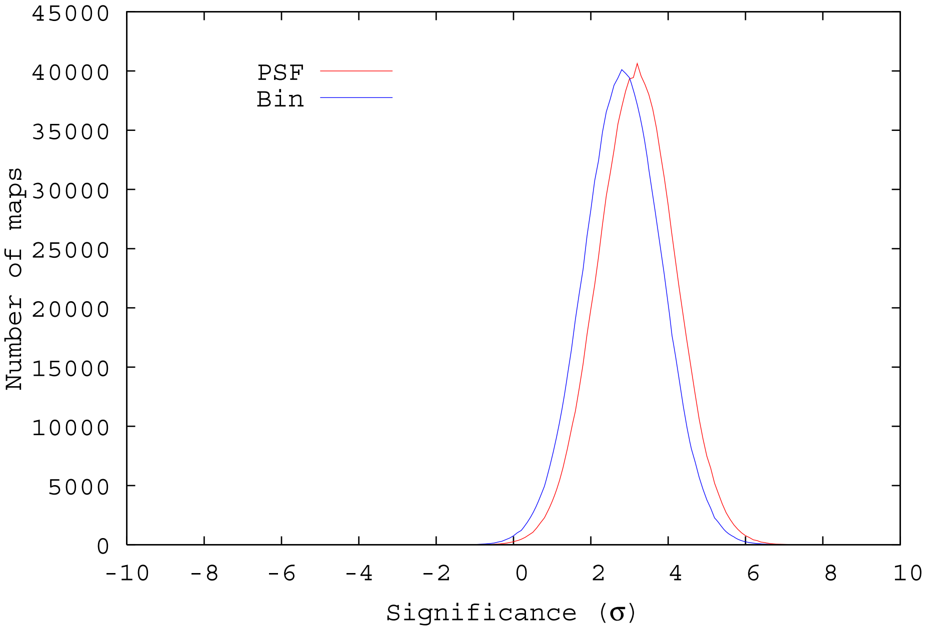

Figure A.1: distributions of the maximum posttrial significane for PSF and bin smoothed maps when σ_s equals 0° and the radius of the search area equals 0°.

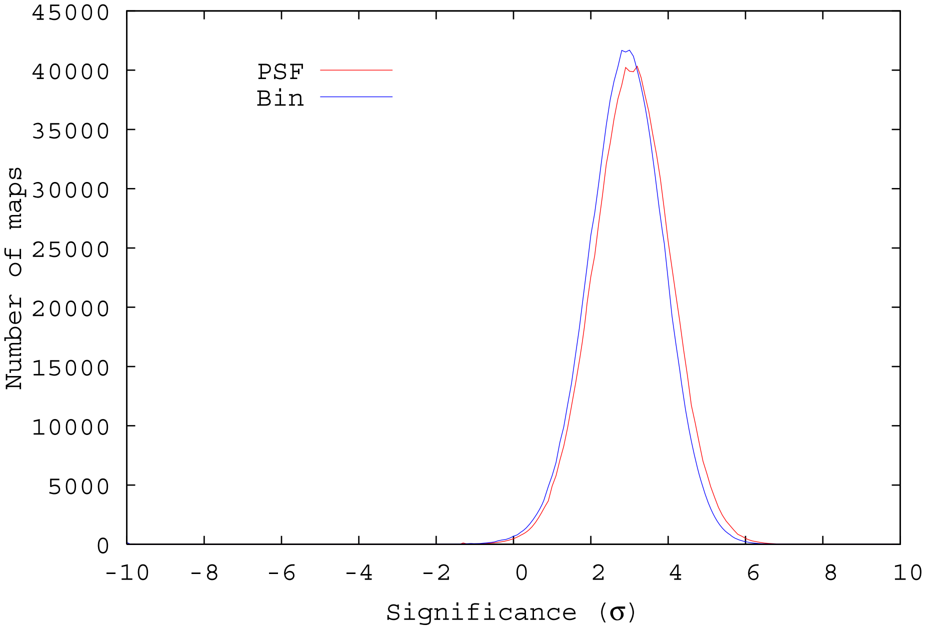

Figure A.2: distributions of the maximum posttrial significane for PSF and bin smoothed maps when σ_s equals 0° and the radius of the search area equals 0.5°.

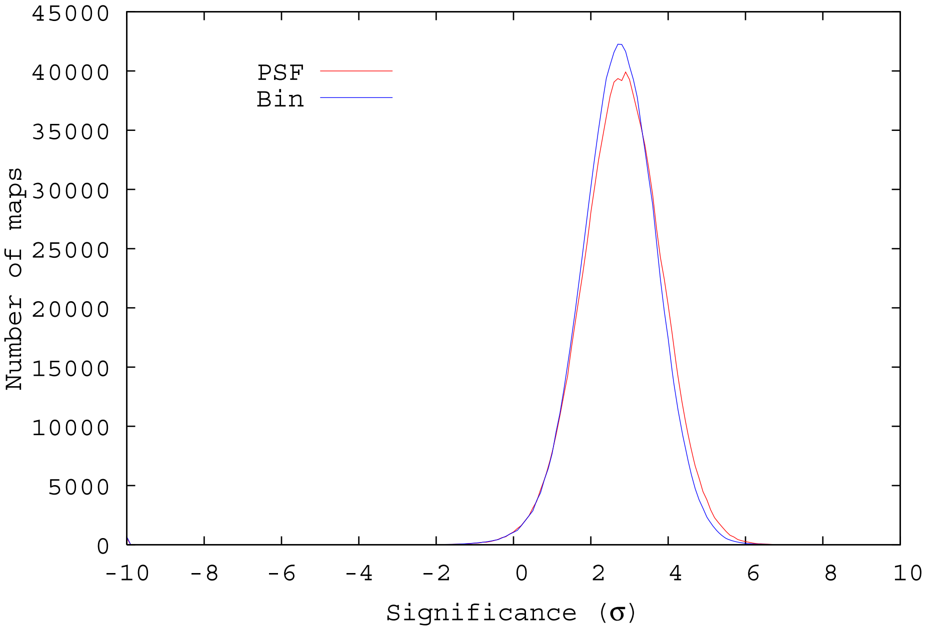

Figure A.3: distributions of the maximum posttrial significane for PSF and bin smoothed maps when σ_s equals 0° and the radius of the search area equals 1.0°.

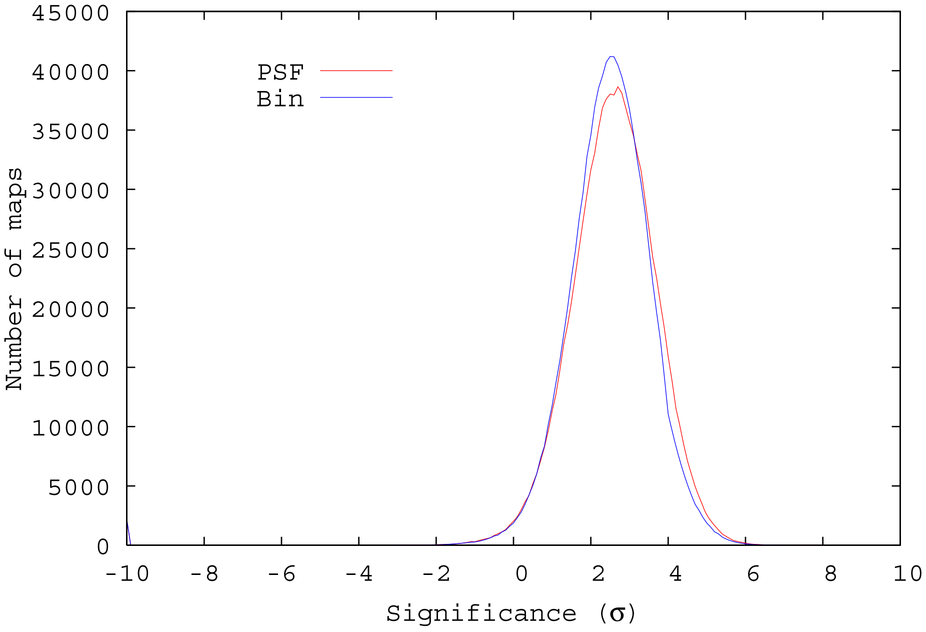

Figure A.4: distributions of the maximum posttrial significane for PSF and bin smoothed maps when σ_s equals 0° and the radius of the search area equals 1.5°.

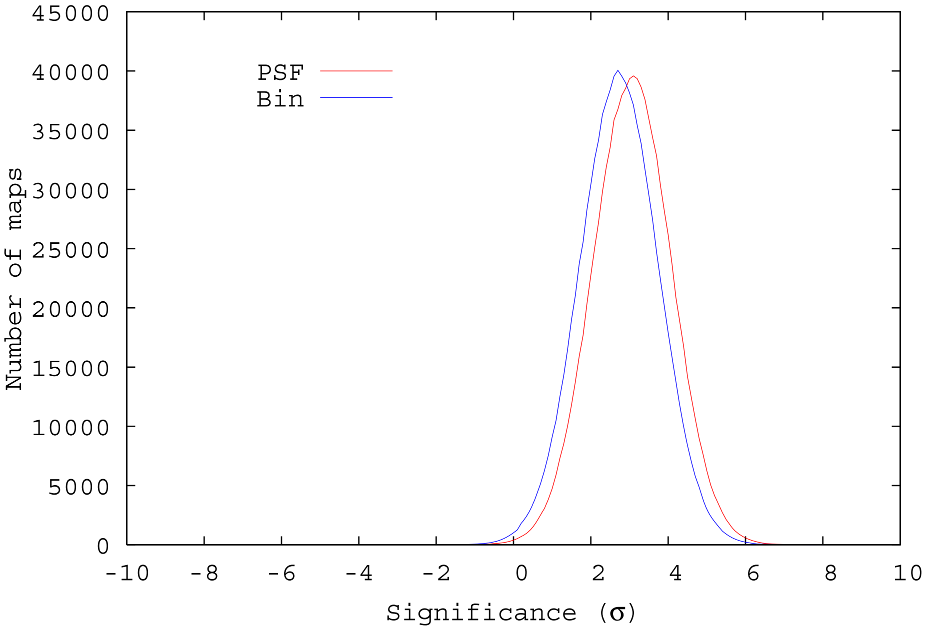

Figure A.5: distributions of the maximum posttrial significane for PSF and bin smoothed maps when σ_s equals 0.2° and the radius of the search area equals 0°.

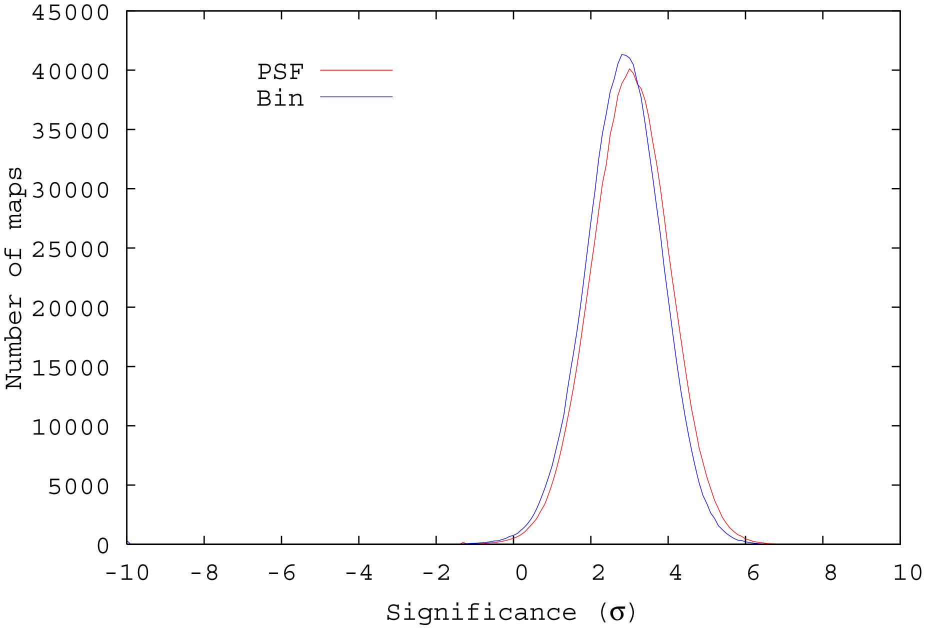

Figure A.6: distributions of the maximum posttrial significane for PSF and bin smoothed maps when σ_s equals 0.2° and the radius of the search area equals 0.5°.

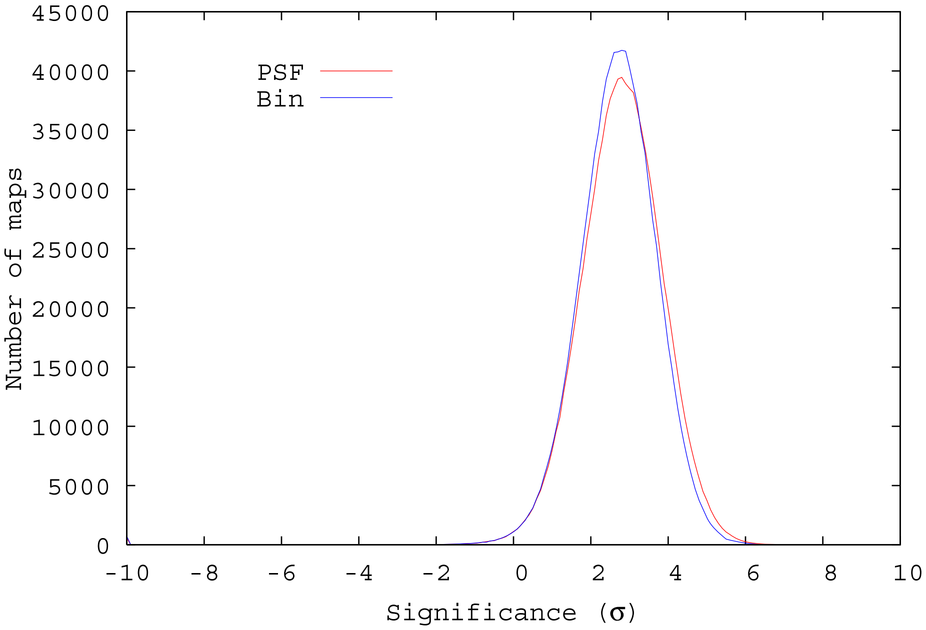

Figure A.7: distributions of the maximum posttrial significane for PSF and bin smoothed maps when σ_s equals 0.2° and the radius of the search area equals 1.0°.

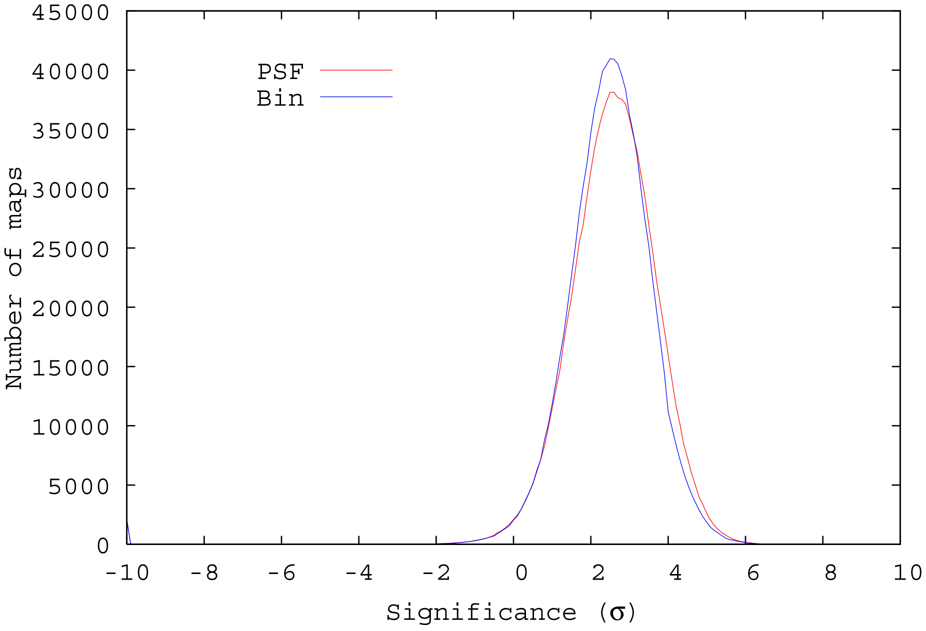

Figure A.8: distributions of the maximum posttrial significane for PSF and bin smoothed maps when σ_s equals 0.2° and the radius of the search area equals 1.5°.

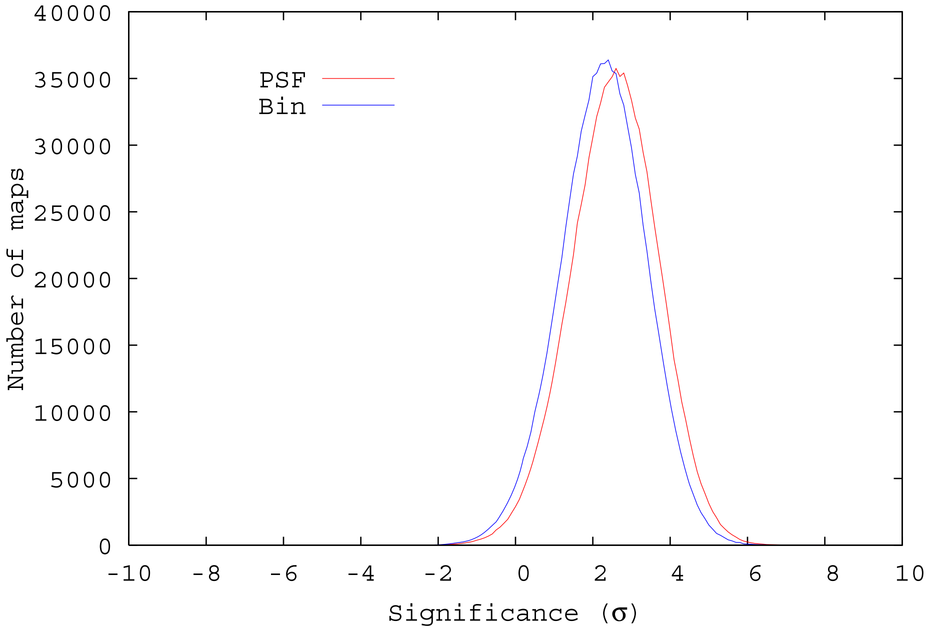

Figure A.9: distributions of the maximum posttrial significane for PSF and bin smoothed maps when σ_s equals 0.5° and the radius of the search area equals 0°.

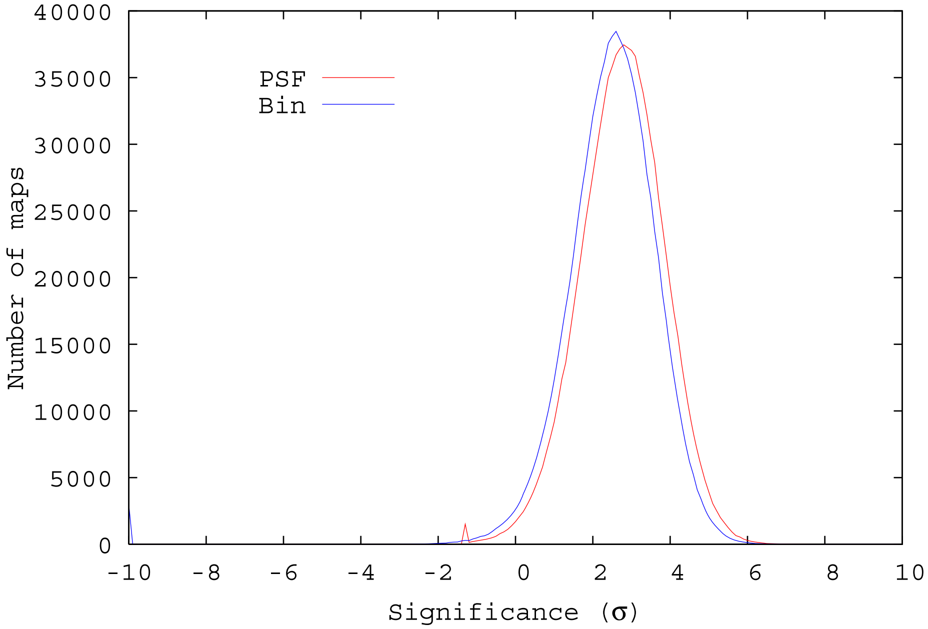

Figure A.10: distributions of the maximum posttrial significane for PSF and bin smoothed maps when σ_s equals 0.5° and the radius of the search area equals 0.5°.

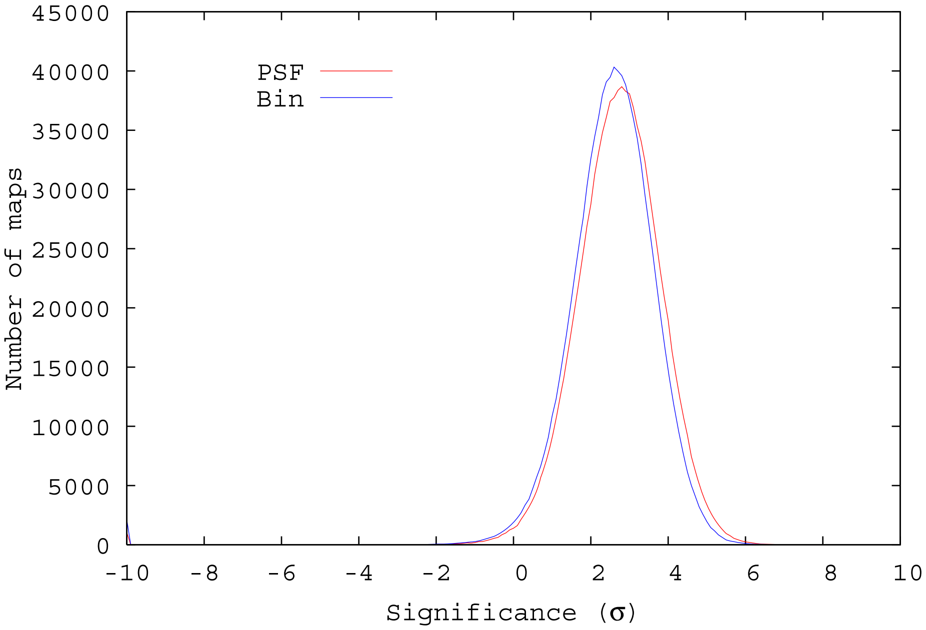

Figure A.11: distributions of the maximum posttrial significane for PSF and bin smoothed maps when σ_s equals 0.5° and the radius of the search area equals 1.0°.

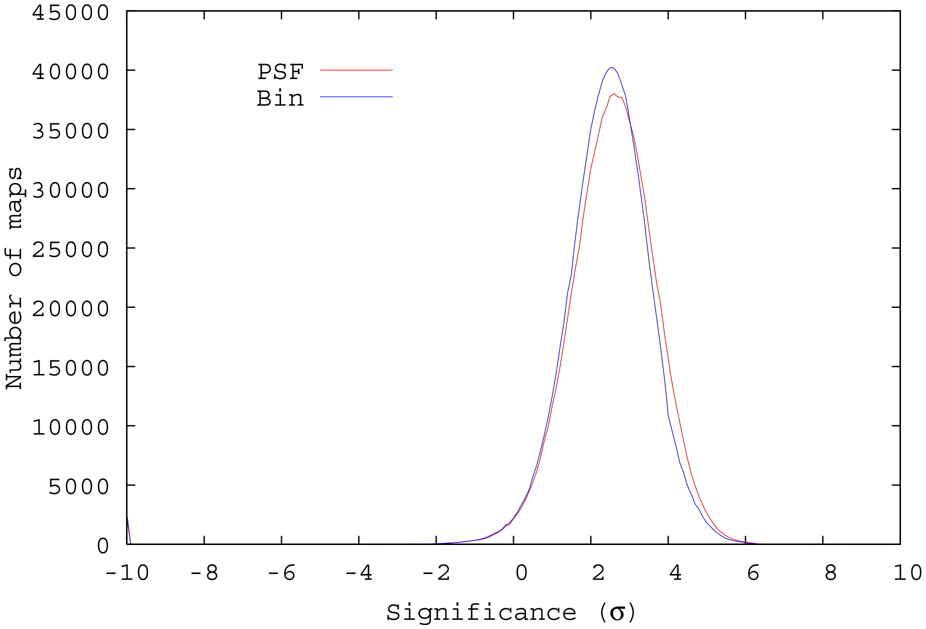

Figure A.12: distributions of the maximum posttrial significane for PSF and bin smoothed maps when σ_s equals 0.5° and the radius of the search area equals 1.5°.

Appendix B

Flux Upper Limit Calculation

The upper limit of a source, A, must depend on the experimental results: the background and the total number of events in the source region. The total counts in the source region will be denoted by C and the background will be denoted by B. A is also depend on the desired significance level, identified by $(1-\alpha)\cdot 100\%$. For a 95% conficence level, α equals 0.05.

The first step is to determinate the probability density function (p.d.f) of the source region after the measurement. It is identified by $g(a)$. The variable a is the total events in the source region. It can be considered as a statistical variable. $g(a)$ should depend on the result B and C, and the p.d.f prior the measurement. The second step is the determination of A, which can be easily be done if we know $g(a)$.

The probability for obtaining C events in the source region is

$$P(C) = \frac{e^{(a+B)}(a+B)^C}{C!} \tag{B.1}$$

This is a Possion distribution with mean $a+B$, and is correct when a and B are the true values. In equation B.1 a and B are parameters and C is a discrete variable.

The determination of the p.d.f of a after the experiment was estabilished very early [45, 46] and the result can be explicitly shown using Bayes theorem [47]. Hence

$$g(a) = N_1 \frac{e^{-(a+B)}(a+B)^C}{C!} \tag{B.2}$$

where N_1 is a normalization constant such that

$$\int_0^\infty g(a)da = 1 \tag{B.3}$$

In equation B.2 B and C are parameters and a is a continuous variable. The Gaussian approximation of equation B.2 is

$$g(a) \cong N_2 \frac{e^{\frac{-(a-\bar{a})}{2C}}}{\sqrt{2\pi C}} \tag{B.4}$$

where $\bar{a}$ is the signal events in the source region and $\bar{a} = C - B$. N_2 is a normalization constant. This approxmation is valid when $C \gg 1$, and the estimated total events of the source region is $\bar{a}$ and $\sqrt{C}$ is its standard deviation. Equation B.2 and **??** are valid when the background is exactly known or has a negligible standard deviation which is true for Milagro experiment.

After we know $g(a)$ we can determine the upper limit of the source region with a desired significance level. The probability of having an a value greater than A is

$$\alpha = \int_A^\infty g(a)da \tag{B.5}$$

The probability of having an a value less than A is $1 - \alpha$. The upper limit A depends on B and C. Plug equation B.4 in equation B.5 we can solve A for a given α.

Bibliography

[1] T. C. Weekes *et al.*. Observation of TeV Gamma Rays from the Crab Nebula using the Atmospheric Cerenkov Imaging Technique. ApJ, 342:379-395, 1989.

[2] C. M. Hoffman, C. Sinnis, P. Fleury, M. Punch. Gamma-Ray Astronomy at High Energies. Reviews of Modern Physics. Volume 71, No. 4, 1999.

[3] E. Hays. A Search for TeV Emission from Active Galaxies using the Milagro Observatory. PhD Thesis, University of Maryland.

[4] B. T. Allen. TeV Energy Spectra of the Crab Nebula, Mrk 421 and the Cygnus Region of the Milky Way. PhD Thesis, University of California, Irvine.

[5] D. J. Thompson *et al.*. Calibration of the Energetic Gamma-Ray Experiment Telescope (EGRET) for the Compton Gamma-Ray Observatory. ApJS, 86:629-656, 1993.

[6] R. Sreekumar *et al.*. EGRET Observations of the Extragalactic Gamma-Ray Emmision. ApJ, 494-523.

[7] H. Aharonian *et al.*. The H.E.S.S. Survey of the Inner Galaxy in Very High Energy Gamma Rays. ApJ, 636:777, 2006.

[8] *http://heasarc.gsfc.nasa.gov/docs/cgro/images/epo/news/*

[9] *http://en.wikipedia.org/wiki/Air_shower_physics*

[10] *http://www.lanl.gov/milagro/cosmicrays.shtml*

[11] D. E. Alexandreas *et al.*. NIM, A311, 350, 1992.

[12] A. Borione *et al.*. NIM, A346, 329, 1994.

[13] P. Morrison. Nuovo Cim. 7 858, 1958.

[14] D. Berley *et al.*. Status of the Expansion of the CYGNUS Array at Los Alamos. In International Cosmic Ray Conference, page 301, 1990.

[15] *http://www.icrr.u-tokyo.ac,jp/em/index.html*

[16] A. A. Abdo *et al.*. Discovery of TeV Gamma-Ray Emission from the Cygnus Region of the Galaxy. ApJ Letters, L33-L36, 2007.

[17] R. W. Atkins *et al*. Evidence for TeV Gamma-Ray Emission from the Galactic Plane. PRL, 95:251103, 2005.

[18] D. Coyne and M. Schneider. First Results on Milagro Water Attenuation Using Measurements from the Upgraded TUBE. Milagro Collaboration Memorandum. (2002)

[19] D. Heck, *et al.*. CORSIKA: A Monte Carlo Code to Simulate Extensive Air Showers. Tech report FZKA 6019, 1998.

[20] *http://geant4.web.cern.ch/geant4/*

[21] R. A. Atkins, *et al.*. Nucl. Instrum. Meth., A449 478-499, 2000.

[22] J. F. McCullough. A Search of the Northern Sky for Short Bursts of TeV Emission using the Milagrito Detector. PhD Thesis, University of California, Santa Cruz.

[23] E. Blaufuss. VME Trigger Card Manual. Milagro Collaboration Memorandum. (2002)

[24] E. Blaufuss. Milagro DAQ Help Page. Milagro Collaboration Memorandum. (2004)

[25] T. B. Li and Y. Q. Ma. Analysis Methods for Results in Gamma-Ray Astronomy. ApJ,272:317-324, 1983.

[26] M. Leonor. Search of a TeV Component of Gamma-Ray Bursts Using the Milagrito Detector. PhD Thesis, University of California, Irvine.

[27] D. E. Alexandreas, *et al.*. Point Source Search Techniques in Ultra High Energy Gamma Ray Astronomy. NIM, A328 570-577, 1993.

[28] G. Walker's email to the Milagro Collaboration.

[29] G. B. Yodh and R. Atkins. A Simple algorithm for Hadron Rejectioin in Milagro. Milagro Collaboration Memorandum (1999)

[30] G. Sinnis. A Maximum Likelihood Approach to Background Rejectiooon. Milagro Collaboration Memorandum

[31] R. Atkins, *et al.*. Observation of TeV Gamma Rays from the Crab Nebula with Milagro Using a New Background Rejection Technique. ApJ, 595:803-811, 2003.

[32] A. A. Abdo. Discovery of Localized TeV Gamma-Ray Sources and Diffuse TeV Gamma-Ray Emission from the Galactic plane with Milagro Using a New Background Rejection Technique. PhD Thesis, Michigan State University.

[33] P. Hüntemeyer, Systematic Studies for the Diffuse Emission Analysis. Milagro Collaboration Memorandum (2007).

[34] A. Smith. A Weighting Analysis of Crab Data. Milagro Collaboration Memorandum (2005).

[35] J. Linnemann. Weighting for Bins of a Hadron Identification or Energy Variable. Milagro Collaboratio Memorandum.

[36] R. Ellsworth. Uncertainties in Weighted Monte Carlo Data. Milagro Collaboration Memorandum (2003).

[37] C. Chen. Weighting Analysis of MC data and the Studies of Unertainties. Milagro Collaboration Memorandum (2006).

[38] R. Atkins, *et al.*. TeV Gamma-ray Survey of the Northern Hemisphere Sky Using the Milagro Observatory. ApJ, 608:680-685, 2004.

[39] A. A. Abdo, *et al.*. TeV Gamma-ray Sources from a Survey of the Galactic Plane with Milagro. ApJL 664:L91-L94, 2007.

[40] R. C. Hartman, *et al.*. The Third EGRET Catalog of High-Energy Gamma-Ray Sources. ApJS, 123:79-202, 1999.

[41] D. J. Thompson, *et al.*. The Second EGRET Catalog of High-Energy Gamma-Ray Sources. ApJS, 101:259-286, 1995.

[42] D. J. Thompson, *et al.*. Supplement to the Second EGRET Catalog of High-Energy Gamma-Ray Sources. ApJS, 107:227-237, 1996.

[43] C. Lansdell. Galactic Place Flux Profiles. Milagro Collaboration Memorandum (2007).

[44] O. Helene. Upper Limit of Peak Area. NIM, 212:319-322, 1983.

[45] W. L. Nicholson, Nucleonics, 24(8) 118, 1966.

[46] L. J. Rainwater and C. S. Wu, Nucleonics 1(2) 60, 1947.

[47] W. T. Eadie, D. Drijard, F. E. James, M. Ross and B. Sadoulet. Statistical Methods in Experimental Physics (North-Holland, Amsterdam, 1971).

[48] S. J. Fegan, *et al.* A Survey of Unidentifiedd EGRET Sources at Very High Energies. ApJ, 624 638F, 2005.

[49] J. E. McEnery, I. V. Moskalenko, and J. F. Ormes. Cosmic Gamma-Ray Sources, eds. K.S. Cheng and G. E. Romero (Cordreche:Kluwer), Astrophysics and Space Science Library v.304, Chapter 15, pp.361-395, 2004.

[50] F. Aharonian, *et al.* The H.E.S.S. Survey of the Inner Galaxy in Very High energy Gamma Rays. ApJ, 636:777-797, 2006.